Electron dynamics in layered materials

Jingwei Dong

INSTITUT POLYTECHNIQUE DE PARIS

NNT : 2021IPPAX019

Thèse de doctorat

Electron Dynamics in Layered Materials

Thèse de doctorat de l'Institut Polytechnique de Paris
préparée à l'Ecole Polytechnique

École doctorale n°626 Ecole Doctorale de l'Institut Polytechnique de Paris (ED IP Paris)
Spécialité de doctorat: Physique de la matière condensée

Thèse présentée et soutenue à Palaiseau, le 25/03/2021, par

Jingwei DONG

Composition du Jury :

Pascal RUELLO Professeur, Le Mans Université	Président
Claude MONNEY Professeur, University of Fribourg	Rapporteur
Azzedine BENDOUNAN Beamline Scientist, TEMPO Beamline of SOLEIL Synchrotron	Examinateur
Valerie VENIARD Permanent Researcher, Ecole Polytechnique	Examinateur
Luca PERFETTI Permanent Researcher, Ecole Polytechnique	Directeur de thèse

Thèse de Doctorat de
L'ECOLE POLYTECHNIQUE
Spécialité: Physique de la matière condensée

Electron dynamics in layered materials

par: **Jingwei DONG**

Soutenue le 25 Mars 2021

Composition du jury**:**

M. Pascal Ruello	Président
M. Claude Monney	Rapporteur
M. Azzedine Bendounan	Examinateur
Mme. Valerie Veniard	Examinatrice
M. Luca Perfetti	Directeur de thèse

To my beloved family

Acknowledgements

Time passes very quickly, often so quickly that I am surprised. In the near four-year work and live experience at École Polytechnique that is a French public institution of higher education and research in Palaiseau, a suburb south of Paris, I am extremely fortunate to be surrounded by many smart and kind people. Without the genuine help provided by these wonderful people, this thesis would not have been possibly completed. Without the meticulous care and concern from them, I could not deal with the hard times for my PhD project and exotic life. Here, I wish to take this opportunity to express my heartfelt thanks and highest respect to all of them.

First of all, I would like to thank my supervisor Prof. Luca Perfetti at Laboratoire des Solides Irradiés (LSI). From the first time I entered the FemtoLab to now, he always tries his best to teach me the relevant details on the femtoARPES system and the electron dynamics in layered materials. His patience and trust in me has given me enough courage and ability to through all the excellent projects I have embarked on. For other members who work at FemtoLab group include Dr. Zhesheng Chen, Prof. Evangelos Papalazarou, Prof. Marino Marsi and graduate student Marie Cherasse, Caillaux jonathan, Jiuxiang Zhang and Pierfrancesco Aversa, I am also very grateful to them for their help. Especially, thanks to the recommendation of Zhesheng Chen, I attained the golden opportunity funded by the China Scholarship Council (CSC, my great country, thanks to you for your scholarship and love) for working on my doctorate under the supervision of Prof. Luca Perfetti at LSI. Moreover, Dr. Zhesheng Chen and Prof. Evangelos Papalazarou gave me timely and valuable advices when I was in difficulty for both my doctoral projects and daily life. Since our apparatus is located at the Soleil synchrotron, the measurements of our group always benefit from the lab resources of the CASSIOPEE beamline at Soleil synchrotron, and our group sometimes could pass the application for beamline experiments and develop our measurements in the ANTARES beamline, the GALAXIES beamline or the TEMPO beamline. I hereby extend my sincere thanks to all people at Soleil synchrotron.

Besides the projects on the electron dynamics in layered materials based on the femtoARPES system, I have also joined the research on the generation and detection of Terahertz radiation (THz) based on nonlinear optical methods. With the guidances of Prof. Yannis Laplace and Dr. Romain Grasset at LSI of École Polytechnique, I not only gain insights into THz generation and detection setup but also acquire further understanding on the superconducting materials. Furthermore, in order to help me form a good experimental

habit, they used to check my notebook for my measurements. I will always remember the valuable sentence that they said to me 'you will not succeed in doing next measurements two months later if you do not write down the experimental details this time'. Since that, I must write down all scientific research details such as the key points I see in books or journals, the experimental methods adopted in our measurements, and the relevant reports in conferences and so on. École Polytechnique is one of the most respected, selective and leading prestigious French universities, and it is also very famous to most Chinese people in China, I am greatly honored to work at LSI of École Polytechnique. And all people of LSI are kindhearted and helpful, I have also learned a lot from the discussions with Prof. Christine Giorgetti and Prof. Jelena Sjakste. when I met something tricky on my registration for the new school year or the academic report even the credit for my PhD degree, Valérie Véniard, Michele Raynaud, Elodie Dubois and Marylene Raclot always helped me handle them. And we together enjoyed delicious food for all LSI people when there were important festivals in France. I heartedly appreciate all people at LSI for their concern and help.

I can not imagine that he/she will how to live happy and successful without any friends. Luckily I have made lots of loyal and kind-hearted friends during my near four-year life in Paris. Due to their company I felt relaxed, calm and good in these years. They are Zailan Zhang, Xuan Liu, Guozhao Zhang, Haiwa Zhang, Wenyi Wu, Ruibin Zhang and Yazhou Wang who worked as a PhD student at Pierre and Marie Curie University and Huacai Yan, Dongjun Wu, Yan Gao and Miao Feng who work as PhD student at Paris-Saclay University and Yuanyuan Liao, Shu Zhang and Qingyu Kong who work at Soleil synchrotron and Zejun Deng, Chuang Yu, Xuan Chen, Guoshun Qin, Rupu Yang, To Duy-Quang, Drong Mariusz and Pinaeva Uliana who worked as a PhD student at the Institut Polytechnique de Paris. Their care and help has made these years memorable and enjoyable.

I am deeply grateful to the members of the thesis committee for the careful reading and the comments they made on the dissertation. Prof. Claude Monney from the Department of Physics at the University of Fribourg in Switzerland and Prof. Pascal Ruello from the Institut des Molécules et Matériaux du Mans at the Le Mans Université in France spent lots of time on my thesis report. Prof. Azzedine Bendounan from the TEMPO beamline at the SOLEIL SYNCHROTRON in France and Prof. Valerie Veniard from the Laboratoire des Solides Irradiés at the École Polytechnique in France gave me many valuable advices on my thesis. I will never forget the corrections and help on my doctoral defense from these four kind and heartful professors.

At last, I would like to thank my parents Yan Dong and Baofen Gou. They are the most important people in my life, they have always provided me the best care and education since I was born. Even though they had not received enough education during their early youth, they have taught me many valuable and meaningful things which are the ways and attitudes to overcome the difficulties and conquer the challenges throughout my life. With their selfless love and support, I can complete doctorate successfully. There is an important proverb in ancient China ’when your parents are alive, do not travel far’, I have not often accompanied them as the only child in my family for such a long time. And I am full of continuously to my parents guilty. After obtaining my PhD degree, I am going to be around them and dutiful to them in order to make up for the regrets in these years.

Résumé

Actuellement, les matériaux lamellaires suscitent un grand intérêt en raison de leurs propriétés électriques et optiques. De tels cristaux peuvent être amincis jusqu'à obtenir une couche atomique et ils montrent une structure de bandes électroniques qui dépend fortement de l'épaisseur de l'échantillon. Les grands changements d'écrantage électronique et de la bande d'énergie interdite en fonction du nombre des couches atomiques peuvent être très attrayantes pour la création d'heterostructures polyvalente et avec des propriétés qui peuvent être changés à la charte. Ces objectifs motivent une attention renouvelée à des composés qui étés connus depuis longtemps pour d'autres applications. On peut dire que le domaine de recherche des matériaux à basse dimensionnalité a été initié par la découverte du graphène et c'est rapidement élargi à d'autres matériaux comme les dichalcogénures de métaux de transition, le phosphore noir et le séléniure d'indium. Nos travaux portent sur la dynamique des états excités dans ces composés, ainsi que sur l'évolution de la structure des bandes lors d'un fort dopage de surface. Le manuscrit est organisé comme suit :

Le **chapitre 1** est une introduction générale sur les matériaux lamellaires. En particulier, nous discutons des propriétés structurelles et électroniques des composés plus connus. Le **chapitre 2** décrit les principes de fonctionnement de la spectroscopique ultra-rapides et montre nombreuses applications sur des matériaux lamellaires. Nous attirons principalement l'attention sur la dynamique des électrons dans les cristaux semi-conducteurs ou avec onde de densité de charge. Le **chapitre 3** illustre la technique expérimentale que nous avons employée et l'enceinte dans lequel nous avons effectuées les mesures. La dynamique des électrons des matériaux lamellaires a été étudiée au moyen de la spectroscopie photoélectronique résolue en temps et en angle (TrARPES), qui est un outil puissant pour cartographier la structure des bandes électronique et pour suivre la dynamique des électrons photo-injectés via une source laser ultra-rapide.

La discussion des données originales de notre travail débute dans le **chapitre 4**. Les mesures TrARPES sur le phosphore noir suivent la distribution électronique dans la bande de conduction en fonction du délai temporale par rapport à l'instant de la photoexcitation. Nos données montrent qu'après thermalisation, les électrons photo-injectés ne produisent pas une diminution de bande d'énergie interdite, ni génèrent-ils une multiplication appréciable du nombre des porteurs. D'autre part, un élargissement Stark de la bande de valence est due à l'écrantage inhomogène d'un potentiel local autour de défauts chargés.

Le **chapitre 5** présente les données ARPES résolues en temps sur une surface de phosphore noir dopée in situ par évaporation des métaux alcalins. Nous mesurons

l'effondrement de la bande interdite dans la couche d'accumulation électronique avec une précision inédite et nous observons des états enterrés qui sont détectable à cause de la faible énergie de photons dans notre sonde. Ces états acquièrent une vitesse de bande étonnamment élevée quand la concentration de dopants augmente. Le **chapitre 6** montre la modification de la dynamique des porteurs chauds lors de la variation du dopage de surface de BP. Dans ce cas, l'analyse proposé est encore préliminaire et doit être complémenté par des calculs ab-initio.

Le **chapitre 7** contient notre travail sur le composé ε-InSe. Comme dans le cas de phosphore noir, nous générons une couche d'accumulation de densité électronique variable à la surface du semi-conducteur. En variant le niveau de dopage à partir du limite semi-conducteur jusqu'au limite métallique, nous observons que l'écrantage quantique des phonons optiques longitudinaux (LO) n'est pas aussi efficace qu'il le serait dans un système strictement bidimensionnel. Ce résultat indique la présence d'un couplage à distance entre les états confinés à la surface et les phonons polaires du volume. De plus, nous montrons qu'une interaction de Fröhlich 3D avec écrantage de Thomas-Fermi peut être utilisée pour reproduire les effets d'un tel couplage à distance. Dans le **chapitre 8**, nous étudions le 1T-TaS_2. Ce matériau appartient aux systèmes d'ondes de densité de charge (CDW) et a été largement étudié par plusieurs équipes de chercheurs. Dans le 1T-TaS_2, la combinaison d'une distorsion structurelle avec des fortes corrélations électroniques conduit à un diagramme de phase complexe et fascinant. Nous reproduisons des données controversées qui ont été récemment publiées dans la littérature et qui identifient une nouvelle instabilité en proximité de la transition métal-isolant. Enfin, le **chapitre 9** résume les conclusions de nos résultats et aborde brièvement les orientations de recherche à venir.

Abstract

Currently, layered materials attract great interest due to their electrical and optical properties. Such crystals can be thinned down to the single layer and display an electronic band structure that strongly depends on the sample thickness. The large tunability of the electronic screening and gap size can be very attracting for the creation of heterostructures whose properties can be designed on demand. These goals motivate the renewed attention to compounds that were known since many years. We can say that the research field of low dimensional materials has been boosted by the discovery of graphene and quickly has been enlarged to other materials as transition metal dichalcogenides, black phosphorous and Indium selenide. Our work will focus on the excited state dynamics in these compounds, as well as on the evolution of the band structure upon surface doping. The manuscript is organized as follow:

Chapter 1 provides a general introduction of layered materials. In particular, we discuss the structural and electronic properties of some relevant compounds. **Chapter 2** describes the principles of ultrafast spectroscopic methods and shows many applications to the case of the layered materials. We mainly focus our attention on the electron dynamics in semiconducting crystals and charge density waves systems. The electron dynamics of layered materials have been investigated by means of time- and angle-resolved photoelectron spectroscopy (TrARPES), which is a powerful tool to directly map the electronic band structure and to follow the dynamics of the electrons photoinjected via an ultrafast laser source. **Chapter 3** discusses the experimental technique of choice and the setup where we have been performed in the reported measurements.

we begin the discussion of our original data in **Chapter 4**. The TrARPES measurements of layered black phosphorus (BP) monitor the electronic distribution in the conduction and valence band as a function of delay time from photoexcitation. The data show that, after thermalization, the photo-injected electrons do not lead to sizable band gap renormalization, neither do they generate an appreciable amount of carrier multiplication. On the other hand, a Stark broadening of the valence band is ascribed to the inhomogeneous screening of a local potential around charge defects. **Chapter 5**

shows time resolved ARPES data on a BP surface that is doped in-situ by means of alkali metals evaporation. We monitor the collapse of the band-gap in the accumulation layer with unmatched accuracy and we observe that the buried states detected by the low energy photons of our probing pulse acquire a surprisingly high band velocity at large dopants concentration. **Chapter 6** deals with the modification of hot carrier dynamics upon increasing the surface doping of BP. In this case the reported analysis is still preliminary and needs to be backed by ab-initio calculations.

Chapter 7 contains our work on layered *ε*-InSe. As in the case of BP, we generate an accumulation layer of varying electronic density on the surface of such semiconductor. By spanning the doping level from the semiconducting to the metallic limit, we observe that quantum screening of Longitudinal Optical (LO) phonons is not as efficient as it would be in a strictly bidimensional system, indicating a remote coupling of confined states to polar phonons of the bulk. Furthermore, we show that a 3D Fröhlich interaction with Thomas-Fermi screening can be used to mimic the effects of such a remote coupling at the *ε*-InSe surface. In **Chapter 8**, we study the layered 1T-TaS_2. This material belongs to the Charge density waves (CDW) systems and has been extensively investigated by several research groups. In 1T-TaS_2, the combination of structural distortion with high electronic correlations leads to a complex and fascinating phase diagram. We could reproduce controversial data that have been recently published in the literature and that identify a new instability in proximity of the metal to-insulator transition. Finally, **chapter 9** summarizes the conclusions of our work and briefly discusses the perspectives of some future directions of research.

Contents

Chapter 1 The introduction of layered materials

Solid-state physics displays a large variety of electronic phases such as metals, semimetals, semiconductors, superconductors and insulators. Especially interesting is the fact that the physical properties of these systems can be widely tuned by external parameters [1-5]. With increasing demand for technological development on photoelectric applications, many materials have drawn attention due to their potentials for the realization of highly scalable low power electronics and other novel devices [6-8]. Layered crystals is an important branch of such solid-state materials. They belong to a special class of materials, in which the crystals are built by the stacking of “two-dimensional” layers and that are bound to each other through weak Van der Waals forces [9,10]. The diagram of the layered material is shown in Figure 1.1.

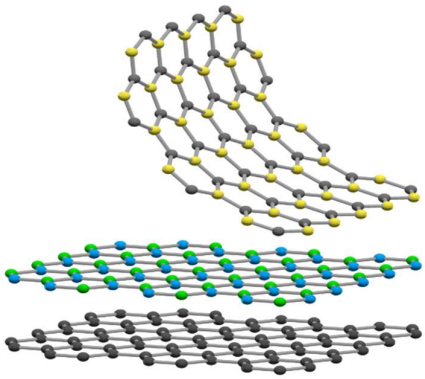

Figure 1.1: The diagram of the layered material.

Layered materials can be synthesized by hydrothermal heating or calcination at high temperature from mixture of raw chemicals. They can display a large variety of functionalities such as high carriers mobility, magnetic ordering, strong luminescence and photocatalytic activity. These properties depend on the chemical composition [11-13] and have been studied for more than a century. Figure 1.2 below shows some applications of layered materials in different scientific contests [14], but the proposed list is far from being exhaustive. The layered materials can be mechanical exfoliated from a bulk compound down to the monolayer limit, they can be intercalated with various elements, supported or self-supporting nanostructured films, can form porous solids, and functional colloids. Their applications involve photonic and electronic devices, chemistry, environment, high performance plastics, soft materials and optoelectronic devices. The discoveries and surveys of this class of materials not only play an important role in scientific research, but

also bridge the gap between solid-state physics and applied research. In our studies, we mainly focus our attention on conventional layered semiconductors and the layered Charge density waves (CDW) system with Mott phase.

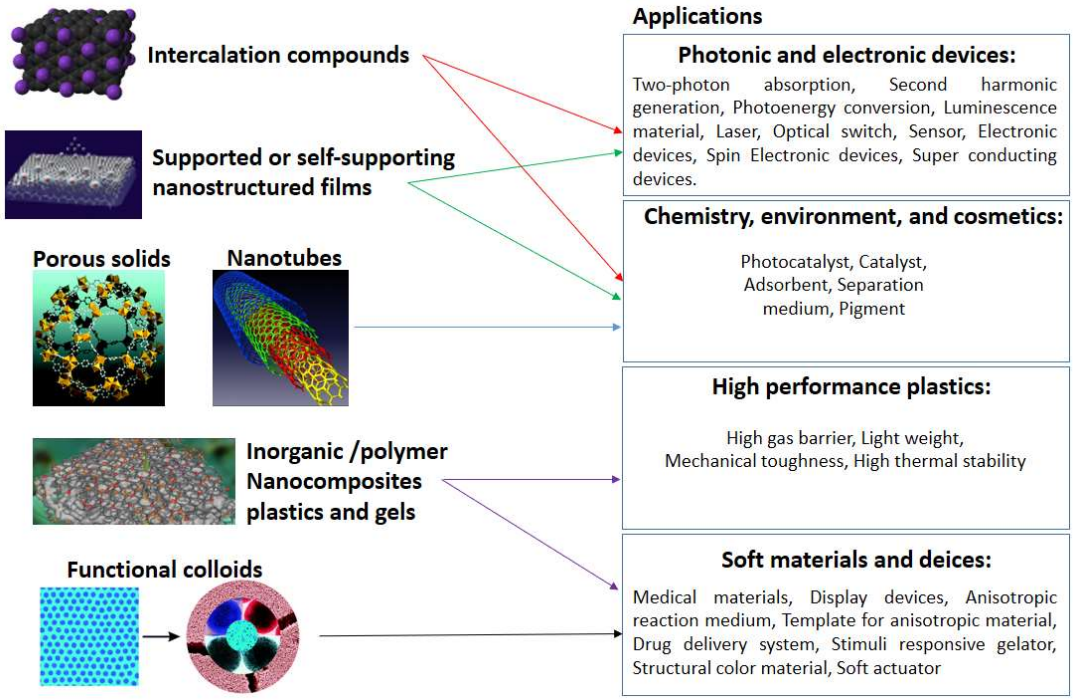

Figure 1.2: Overview of applications of layered materials [14]**.**

1.1 Layered semiconductors

Many semi-metallic and semiconducting compounds belonging to the family of layered material, display interesting optoelectronic properties and have proved a high potential for the application in the current nanoelectronics [15-18].

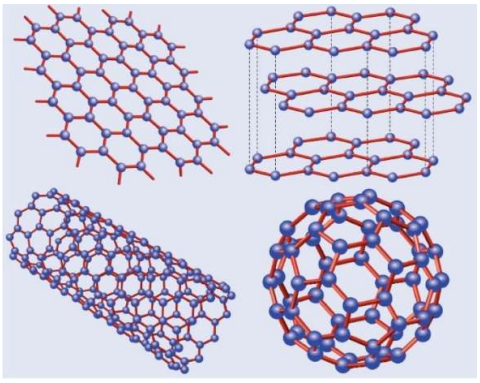

Figure 1.3: Graphene and its allotropes: top left: graphene; top right: graphite = stacked graphene; bottom left: nanotube=rolled graphene; bottom right: fullerene=wrapped graphene [22, 23].

The best known of all monolayer crystals is surely the one obtained by peeling graphite, namely graphene. Due the excellent carrier's mobility, graphene is often employed as electrode in nanoscale devices [19-21]. Fig. 1.3 shows the crystal structures of graphene and allotropes [22, 23], where each carbon atom is bounded to three nearest neighbors via an sp2 hybridization of the atomic orbitals. In despite of the extraordinary carrier mobility, graphene is a zero gap semiconductor, since the conduction and valence band meet at the Dirac points. The absence of an electronic gap severely limits the on-off current ratio of field-effect transistors that are based solely on graphene [24]. Moreover, it is hard if not impossible to generate a sizable bandgap in some graphene allotropes (as nanoribbons or bilayers on a substrate) without degrading its crystal quality and electronic properties [25-27]. For this reason, the generation of heterostructures where graphene is flanked by layered semiconductors is essential to realize performing devices in nanoelectronics.

The richness of such heterostructure resides in the large flexibility allowed by the Van der Waals bonds. Moreover, the electronic bandgap can be widely tuned by changing the compound and the number of layers. In the family of layered semiconductors, the Transition Metal Dichalcogenides (TMDCs) are probably the most studied ones. The monolayer TMDCs are two-dimensional (2D) materials where the transition metal atoms are sandwiched between two layers of chalcogens. Figure 1.4 shows the possible TMDs compounds that can be obtained by combining a transition metal atom and a chalcogenide [28]. As all the layered semiconductors, also the semiconducting TMDCs possess an electronic band gap that increases with decreasing thickness of the crystal [29, 30].

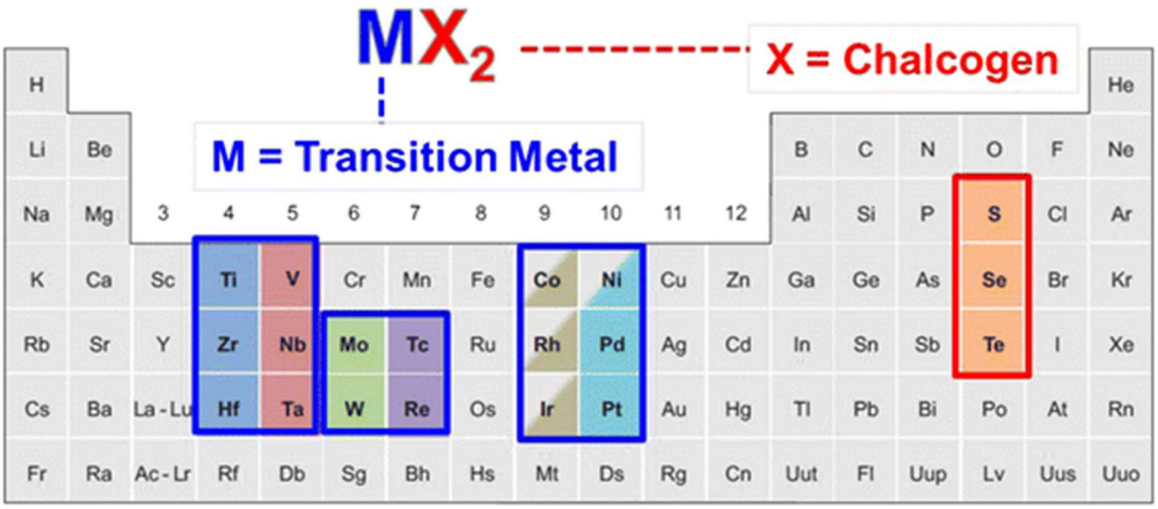

Figure 1.4: There are a number of possible TMDs compounds, which can be obtained by choosing one of the 16 transition metals and one of the 3 chalcogen atoms [28].

Molybdenum disulfide (MoS_2) is one representative example of transition metal dichalcogenide. It has an indirect band gap of 1.23 eV in the bulk 2H-MoS_2 and 3R-MoS_2 phases (the "H" and the "R" indicate hexagonal and rhombohedral symmetry, respectively) whereas it has a direct band gap of 1.8 eV in the monolayer limit. The 2H- and 3R structures are shown in Fig. 1.5 [31]. In both of these structures, each molybdenum atom is at the center of a trigonal prismatic coordination sphere and is covalently bonded to six sulfide ions. Each sulfur atom has pyramidal coordination and is bonded to three molybdenum atoms. Furthermore, a third phase 1T-MoS_2 has been discovered by means of intercalating 2H-MoS_2 with alkali metals. This metallic phase with tetragonal symmetry is also displayed in Fig. 1.5 [31]. The 1T-phase can be stabilized through doping with electron donors like rhenium, or converted back to the 2H-phase by microwave radiation [32]. Besides the bandgap tenability, the monolayer MoS_2 displays other optoelectronic properties of high interest. The degrees of freedom related to the valley character and spin flavor can be addressed and controlled by optical pulse of defined helicity. Indeed, the optical interband transitions have frequency-dependent polarization selection rules which allow selective photoexcitation of carriers with various combination of valley and spin indices. The signature of excitons in a defined valley leads indeed to selective circular dichroism (CD), therefore suggesting possible applications of “valleytronics” in future optoelectronic devices [33]. Here we limit the discussion to few relevant articles that have treated this subject. For examples, Di Xiao and his co-workers have shown that inversion symmetry breaking together with spin-orbit coupling leads to coupled spin and valley polarization in monolayers of MoS_2, making possible controls of spin and valley in some 2D materials [34]. They asserted that the spin-valley coupling at the valence-band edges suppresses spin and valley relaxation, as the flip of each index alone is forbidden by the valley-contrasting spin splitting. Dal Conte and his colleagues studied the exciton valley relaxation dynamics in single-layer MoS_2 by a combination of two nonequilibrium optical techniques: time-resolved Faraday rotation and time-resolved circular dichroism [35]. The depolarization dynamics, measured at 77 K, exhibits a peculiar biexponential decay, characterized by two distinct time scales of 200 fs and 5 ps. The fast relaxation of the valley polarization is in good agreement with a model including the intervalley electron-hole Coulomb exchange as the dominating mechanism. The valley relaxation dynamics is further investigated as a function of temperature and photoinduced exciton density. They measured a strong exciton density dependence of the transient Faraday rotation signal. This indicates the key role of exciton-exciton interactions in MoS_2 valley relaxation dynamics. Dong Hak Kim and collaborators studied the excitonic valley polarization and

coherence in few-layer MoS2 by using circular- and linear-polarization-resolved photoluminescence [36]. They indicated that the valley polarization is largest in monolayer MoS_2 and decreases with increasing number of layers or temperature. Contrary to the valley polarization, the linear polarization is negligibly small in monolayer MoS_2 and increases with increasing number of layers or temperature. The temperature-dependent valley depolarization can be explained by the exciton center-of-mass momentum-dependent electron-hole exchange interaction. The valley decoherence in few-layer MoS_2 is much faster than the valley depolarization at low temperature and is steady against increasing temperature or photoexcitation intensity, indicating that the decoherence process does not involve phonon or carrier-carrier scattering. The dominant valley decoherence has a pure dephasing origin and cannot be explained by the valley-depolarizing e-h exchange interaction.

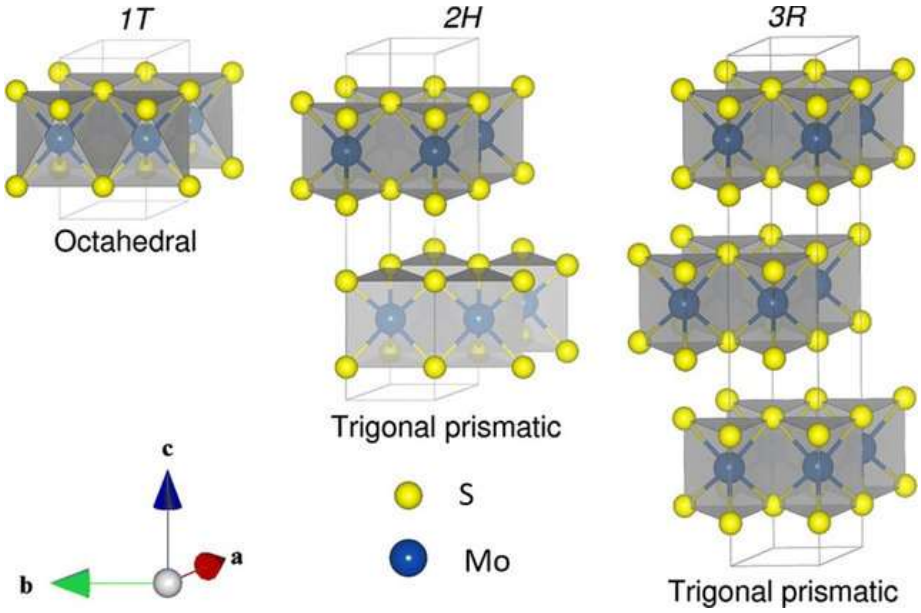

Figure 1.5: Crystal structures of MoS2: Octahedral (1T), Trigonal prismatic (2H) and Trigonal prismatic (3R) unit cell structures [31].

Recently some ambitious experiments have even shown that the Valley Hall and spin Hall effects coexist in both electron-doped and hole-doped systems [37]. The photoinduced spin Hall and valley Hall effects can be employed to generate long lived spin and valley accumulations on sample boundaries.

Black phosphorus (BP) [38,39] and indium selenide (InSe) [40] are layered semiconductors that do not hold valleys at the conduction band and valence band minima as the TMDC, but hold many interesting properties that are common to this family.

Depending on the number of layers, BP has a bandgap bridging between the graphene and TMDCs. Interestingly, InSe has a bandgap which is large enough in order to build field effect transistors and displays an exceptionally high carrier's mobility [41]. A detailed survey of BP and InSb, which are most relevant in this thesis work, will be given in chapters 4, 5, 6 and chapter 7, respectively. Here instead, complete our general overview by mentioning the existence of two layered magnetic semiconductors, the compounds $CrGeTe_3$ and CrX_3 (X = Cl, Br, I). These crystals can be thinned down to a monolayer, still retaining the magnetic order [42-44]. Traditional electronics are based on control of charge carriers (n- or p-type), however, magnetic semiconductors would also allow control of quantum spin state (up or down). It has been suggested that near-total spin polarization would be possible in these monolayer magnetic semiconductors (as opposed to iron and other metals, which provide only up to 50% polarization). Figure 1.6 illustrate the development of a net spin polarization in the ferromagnetic phase of monolayer magnetic semiconductors [42]. This process differs from the spin dependent shift of the density of electronic states that takes place upon doping with diluted magnetic impurities. Even if monolayer CrI_3 is ferromagnetic, the magnetic ground state of the few-layer CrI_3 consists instead of antiferromagnetically coupled ferromagnetic monolayers with out-of-plane easy axis [44]. The interlayer exchange interaction is relatively weak. Shengwei Jiang and his co-workers quantified the relative importance of the exchange and anisotropy magnetostriction by measuring the resonance frequency under a magnetic field parallel and perpendicular to the easy axis, respectively. Furthermore, they showed efficient strain-tuning of the internal magnetic interactions in two-dimensional CrI_3 as a result of inverse magnetostriction [45]. John Cenker and his colleagues reported the direct observation of two-dimensional magnons through magneto-Raman spectroscopy with optical selection rules determined by the interplay between crystal symmetry, layer number and magnetic states in atomically thin CrI_3 [46]. Besides, Amber McCreary and her co-workers observed a striking evolution of the Raman spectra with increasing magnetic field applied perpendicular to the atomic layers in which clear, sudden changes in intensities of the modes are attributed to the interlayer ordering changing from antiferromagnetic to ferromagnetic at a critical magnetic field value [47]. These property suggests many different applications of monolayer magnetic semiconductors such as spin filters and spin transistors.

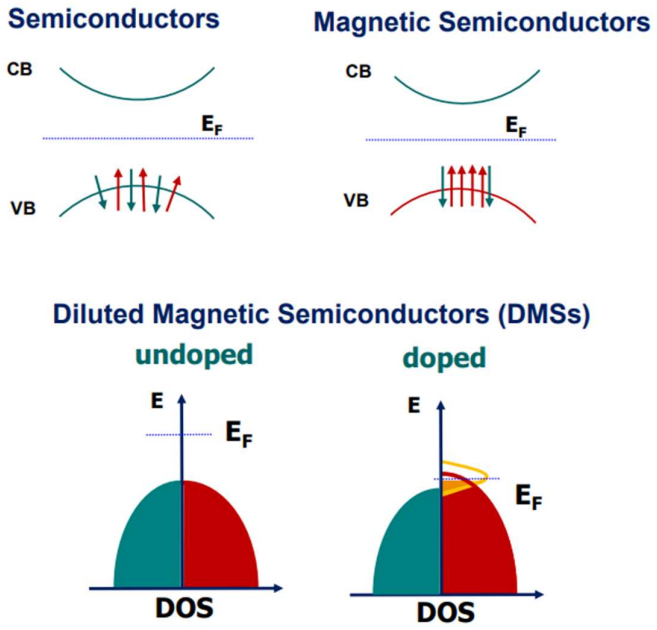

Figure 1.6: The spin polarization difference between monolayer magnetic semiconductors and doped magnetic semiconductors [42].

1.2 Layered crystals with Charge Density Waves (CDW) and Mott insulator

Charge density waves (CDWs) are collective electronic condensates originating from the strong coupling of conduction electrons and the underlying lattice. Several of the transition metals chalcogenides display CDW ordering below room temperature. These systems have generated considerable interest in condensed matter physics, owing to the important insight into the electron-phonon interaction and to the connections between CDW and similar charge ordering that have been observed in superconducting cuprates. Most CDW formations are favored by Fermi surface (FS) nesting, i.e., the matching of sections of FS to others by a wave vector q, which lowers the electronic energy of the distorted phase. In quasi-1D CDW systems, the perfect nesting condition can be easily realized and the FS would be fully gapped, resulting in a semiconducting phase, as manifested in most quasi-1D materials. In higher dimensional systems instead, the FS nesting could remove at best only part of the FSs. Due to the residual ungapped regions of FSs, the CDW phase tends to keep metallic. Though a few examples exhibit semiconducting 2D CDW states, the semiconducting phase is not truly driven by the FS nesting but rather by strong electron-phonon coupling matrix elements. Moreover, other physical mechanisms as the Mott localization of electrons or excitonic correlations may be concurrent to the CDW formation [48, 49]. This is for example the case of 1T-$TiSe_2$ that has been often identified with an excitonic insulator [49]. The layered CDW crystal 1T-$TaSe_2$ and 1T-TaS_2 display instead a

Mott phase and several charge ordering that may depend on the sample thickness [50, 51]. Mott insulators are a class of materials that should conduct electricity under conventional band theories but are in fact insulators due to electron–electron interactions. This type of insulators often hold a rich phase diagram, which may be explored by varying the composition, pressure, strain, voltage, or magnetic field. The devices based on the Mott localization has been recently proposed as building blocks of neuromorphic devices [52, 53]. Further details of 1T-TaS_2 will be depicted in chapter 8. Finally, we mention that other TMDCs, such as 2H-$NbSe_2$ display a CDW order in competition with the superconducting phase [54]. These compounds have been model systems where to observe the Higgs Boson by Raman spectroscopy.

References

[1] Lin, Y., Shao, Y., Dai, J. *et al.* Metallic surface doping of metal halide perovskites. *Nat Commun* **12,** 7 (2021).

[2] Konstantinova, T., Wu, L., Yin, WG. *et al.* Photoinduced Dirac semimetal in $ZrTe_5$. *npj Quantum Mater.* **5,** 80 (2020).

[3] Y. Cao. et al., Quality Heterostructures from Two-Dimensional Crystals Unstable in Air by Their Assembly in Inert Atmosphere. *Nano Lett*. **15** (8), 4914-4921 (2015).

[4] Abdel-Hafiez, M., Zhao, XM., Kordyuk, A. *et al.* Enhancement of superconductivity under pressure and the magnetic phase diagram of tantalum disulfide single crystals. *Sci Rep* **6,** 31824 (2016).

[5] Yue, Z., Xue, G., Liu, J. et al. Nanometric holograms based on a topological insulator material. *Nat Commun* **8**, 15354 (2017).

[6] Dey, S., Nag, S., Santra, S. et al. Voltage-controlled NiO/ZnO p–n heterojunction diode: a new approach towards selective VOC sensing. *Microsyst Nanoeng* **6**, 35 (2020).

[7] Ioannou, P.S., Kyriakides, E., Schneegans, O. et al. Evidence of Biorealistic Synaptic Behavior in Diffusive Li-based Two-terminal Resistive Switching Devices. *Sci Rep* **10**, 8711 (2020).

[8] Werner, F., Veith-Wolf, B., Melchiorre, M. et al. Ultra-thin passivation layers in Cu(In,Ga)Se2 thin-film solar cells: full-area passivated front contacts and their impact on bulk doping. *Sci Rep* **10**, 7530 (2020).

[9] Frisenda, R., Niu, Y., Gant, P. *et al.* Naturally occurring van der Waals materials. *npj 2D Mater Appl* **4,** 38 (2020).

[10] George, A., Fistul, M.V., Gruenewald, M. *et al.* Giant persistent photoconductivity in monolayer MoS_2 field-effect transistors. *npj 2D Mater Appl* **5,** 15 (2021).

[11] Wu, Z., Hao, J. Electrical transport properties in group-V elemental ultrathin 2D layers. *npj 2D Mater Appl* **4,** 4 (2020).

[12] Hao, L., Meyers, D., Suwa, H. *et al.* Giant magnetic response of a two-dimensional antiferromagnet. *Nature Phys* **14,** 806–810 (2018).

[13] Jenjeti, R.N., Kumar, R., Austeria, M.P. *et al.* Field Effect Transistor Based on Layered $NiPS_3$. *Sci Rep* **8,** 8586 (2018).

[14] N.Miyamoto, S.Yamamoto, Katsuhiko Ariga and Masakazu Aono. Supra-Materials Nanoarchitectonics. Book, (2017).

[15] A. K. Geim, I. V. Grigorieva, Van der Waals heterostructures, *Nature* **499**, 419-425 (2013).

[16] Wan, Z., Kazakov, A., Manfra, M. et al. Induced superconductivity in high-mobility two-dimensional electron gas in gallium arsenide heterostructures. *Nat Commun* **6**, 7426 (2015).

[17] Jenjeti, R.N., Kumar, R., Austeria, M.P. et al. Field Effect Transistor Based on Layered NiPS 3. *Sci Rep* **8**, 8586 (2018).

[18] Blancon, J., Stier, A.V., Tsai, H. et al. Scaling law for excitons in 2D perovskite quantum wells. *Nat Commun* **9**, 2254 (2018).

[19] K.S.Novoselov,A.K.Geim,S.V.Morozov,D.Jiang,Y.Zhang, S. V. Dubonos, I. V. Grigorieva, and A. A. Firsov, Electric field effect in atomically thin carbon films. *Science* **306**, 666 (2004).

[20] K. S. Novoselov, A. K. Geim, S. V. Morozov, D. Jiang, M. I. Katsnelson, I. V. Grigorieva, S. V. Dubonos, and A. A. Firsov, Two-dimensional gas of massless Dirac fermions in graphene, *Nature* **438**, 197 (2005).

[21] Y. Zhang, J.W.Tan, H.L.Stormer and P.Kim, Experimental observation of the quantum Hall effect and Berry's phase in graphene, *Nature* **438**, 201 (2005).

[22] A. H. Castro Neto, F. Guinea, N. M. R. Peres, K. S. Novoselov, and A. K. Geim. The electronic properties of graphene. *Reviews of Modern Physics* **81**, 109 (2009).

[23] A. H. Castro Neto, F. Guinea, and N. M. R. Peres. Drawing conclusions from graphene. *Physics World* **19**, 33(2006).

[24] F. Xia, D. B. Farmer, Y.-M. Lin, and P. Avouris. Graphene Field-Effect Transistors with High On/Off Current Ratio and Large Transport Band Gap at Room Temperature. *Nano Lett.* **10**, 715 (2010).

[25] K. S. Kim et al. Coexisting massive and massless Dirac fermions in symmetry-broken bilayer graphene. *Nat. Mater*. **12**, 887–892 (2013).

[26] Martin Gmitra & Jaroslav Fabian. Graphene on transition-metal dichalcogenides: a platform for proximity spin-orbit physics and optospintronics. *Phys. Rev. B* **92**, 15(2015).

[27] Cai, Y., Zhang, G. & Zhang, Y.-W. Electronic properties of phosphorene/graphene and phosphorene/hexagonal boron nitride heterostructures. *J. Phys. Chem. C* **119**, 13929–13936 (2015).

[28] Han, S.A., Bhatia, R. & Kim, S. Synthesis, properties and potential applications of two-dimensional transition metal dichalcogenides. *Nano Convergence* **2**, 17 (2015).

[29] Keum, D. H. et al. Bandgap opening in few-layered monoclinic MoTe2. *Nature Physics* **11**(6), 482–486 (2015).

[30] Lindlau, J., Selig, M., Neumann, A. et al. The role of momentum-dark excitons in the elementary optical response of bilayer WSe_2. *Nat Commun* **9**, 2586 (2018).

[31] Han B, Hu YH. MoS_2 as a co-catalyst for photocatalytic hydrogen production from water. *Energy Sci Eng* **4**:285–304 (2016).

[32] Wang, Q.; Ge, S.; Li, X.; Qiu, J.; Ji, Y.; Feng, J.; Sun, D. Valley Carrier Dynamics in Monolayer Molybdenum Disulfide from Helicity Resolved Ultrafast Pump-Probe Spectroscopy. *ACS nano* **7** (12), 11087-11093 (2013).

[33] Nurmamat, M., Ishida, Y., Yori, R. et al. Prolonged photo-carriers generated in a massive-and-anisotropic Dirac material. *Sci Rep* **8**, 9073 (2018).

[34] Xiao D, Liu GB, Feng W, Xu X, Yao W. Coupled spin and valley physics in monolayers of MoS2 and other group-VI dichalcogenides. *Phys Rev Lett* **108**(19):196802 (2012).

[35] S. Dal Conte, F. Bottegoni, E. A. A. Pogna, D. De Fazio, S. Ambrogio, I. Bargigia, C. D'Andrea, A. Lombardo, M. Bruna, F. Ciccacci, A. C. Ferrari, G. Cerullo, and M. Finazzi. Ultrafast valley relaxation dynamics in monolayer MoS2 probed by nonequilibrium optical techniques. *Phys. Rev. B* **92**, 235425 (2015).

[36] Kim, D.H., Shin, M.J. & Lim, D. Excitonic valley polarization and coherence in few-layer MoS_2.*Journal of the Korean Physical Society* **66**, 806–810 (2015).

[37] Di Xiao, Gui-Bin Liu, Wanxiang Feng, Xiaodong Xu, and Wang Yao. Coupled Spin and Valley Physics in Monolayers of MoS2 and Other Group-VI Dichalcogenides. *Phys Rev Lett* **108**, 196802 (2012).

[38] H. O. H. Churchill, P. Jarillo-Herrero, Phosphorus joins the family, *Nat. Nanotechnol*. **9**, 330–331 (2014).

[39] Liu, Y., Rodrigues, J.N.B., Luo, Y.Z. et al. Tailoring sample-wide pseudo-magnetic fields on a graphene–black phosphorus heterostructure. *Nature Nanotech* **13**, 828–834 (2018).

[40] Bandurin, D. A. et al. High electron mobility, quantum Hall effect and anomalous optical response in atomically thin InSe. *Nat. Nanotech*. **12**, 223–227 (2017).

[41] Jiang, J., Li, J., Li, Y. et al. Stable InSe transistors with high-field effect mobility for reliable nerve signal sensing. *npj 2D Mater Appl* **3**, 29 (2019).

[42]https://download.uni-mainz.de/fb08-spice/2020-08-04-2DvanDerWaals/2020-VDW-Hee_Lee.pdf

[43] Zhang Z, Shang J, Jiang C, Rasmita A, Gao W, Yu T. Direct photoluminescence probing of ferromagnetism in monolayer two-dimensional CrBr3. *Nano Lett*. **19**:3138-3142 (2019).

[44] Xu, C., Feng, J., Xiang, H. *et al.* Interplay between Kitaev interaction and single ion anisotropy in ferromagnetic CrI_3 and $CrGeTe_3$ monolayers. *npj Comput Mater* **4,** 57 (2018).

[45] Jiang, S., Xie, H., Shan, J. *et al.* Exchange magnetostriction in two-dimensional antiferromagnets. *Nat. Mater.* **19,** 1295–1299 (2020).

[46] Cenker, J., Huang, B., Suri, N. *et al.* Direct observation of two-dimensional magnons in atomically thin CrI_3. *Nat. Phys.* **17,** 20–25 (2021).

[47] McCreary, A., Mai, T.T., Utermohlen, F.G. et al. Distinct magneto-Raman signatures of spin-flip phase transitions in CrI_3. *Nat Commun* **11**, 3879 (2020).

[48] P. Fazekas and E. Tosatti, Electrical, structural and magnetic properties of pure and doped 1T-TaS_2. *Philosophical Magazine B* **39**, 229 (1979).

[49] H. Cercellier, C. Monney, F. Clercet et. al. Evidence for excitonic phase in 1T-$TiSe_2$. *Phys Rev Lett* **99**, 146403 (2007).

[50] Y Chen et al. Strong correlations and orbital texture in single-layer 1T-$TaSe_2$. *Nature physics* **16**, 218 (2020).

[51] Yoshida, M., Zhang, Y., Ye, J. et al. Controlling charge-density-wave states in nano-thick crystals of 1T-TaS2. *Sci Rep* **4**, 7302 (2014).

[52] Y. Zhou and S. Ramanathan. Mott memory and neuromorphic devices. *Proceedings of the IEEE*, **103**(8):1289–1310, (2015).

[53] Etienne Janod, Julien Tranchant, Benoit Corraze, Madec Querré, Pablo Stoliar, Marcelo Rozenberg, Tristan Cren, Dimitri Roditchev, Vinh Ta Phuoc, Marie-Paule Besland, and Laurent Cario. Resistive switching in mott insulators and correlated systems. *Advanced Functional Materials*, **25**(40):6287–6305, (2015).

[54] Kiss, T., Yokoya, T., Chainani, A. et al. Charge-order-maximized momentum-dependent superconductivity. *Nature Phys* **3**, 720–725 (2007).

Chapter 2 Ultrafast spectra of layered materials

The fundamental scattering processes in condensed matter span the femtosecond to picosecond time scale and can be monitored in real time by means of ultrafast spectroscopy. This kind of techniques are employed in condensed matter to investigate the carrier's photoexcitation and relaxation dynamics, the excitonic effects, the electron-electron interaction and the coupling between electron and phonon modes of the nuclear lattice [1-3]. To these purposes, several pump-probe techniques have been developed, such as Pump-Probe Transient Absorption Spectroscopy, Pump-Probe Reflection Spectroscopy, Time Resolved Fluorescence Spectroscopy and Time- and Angle-Resolved Photoelectron Spectroscopy. Besides the common ultrafast sources based on visible light, also ultraviolet, infrared and Terahertz (THz) pulses are today available, extending the scope of optical pump-probe spectroscopy to the control of collective excitations lying in the meV energy range or, conversely, to the direct observation of electronic motion on the attosecond timescale. The wealth of these time resolved techniques has been used to study a large variety of physical phenomena, complex many-body states such as Cooper pair and vortex dynamics in superconductors [4], CDW motion [5], metal-insulator phase transitions [6]. Most recently, some notable efforts have been even made in order to explore metamaterials that may lead to novel functionalities.

2.1 Optical pump-probe transient absorption spectroscopy

The optical pump-probe transient absorption spectroscopy is the most common technique to follow the temporal evolution of photoexcited electrons and nuclear vibrations in molecules or condensed matter systems [7]. An illustration of the optical pump-probe transient absorption measurement is shown in Fig. 2.1. Several review articles have explained in detail the working principles of this technique [8-10]. For example, in a transient absorption measurement, a fraction of the electrons in the valence band is promoted to an electronically excited state by means of an excitation (or pump) pulse [8]. Depending on the type of experiment, this fraction typically ranges from 0.1% to tens of percents. In order to avoid multiphoton/multistep processes during probing, a weak probe is sent through the sample with a delay τ with respect to the pump pulse (Fig.2.1). A difference absorption spectrum is then extracted, i.e., the absorption spectrum of the excited sample minus the absorption spectrum of the sample in the ground state (ΔA) without pumping. By changing the time delay τ between the pump and the probe and

recording a Δ*A* spectrum at each time delay, a Δ*A* profile as a function of τ and wavelength λ, i.e., a Δ*A*(λ,τ) is obtained. Δ*A*(λ,τ) contains information on the dynamic processes that occur in the excited state, such as thermalization among electrons, emission of phonons, plasmonic modes and possible photoinduced transition.

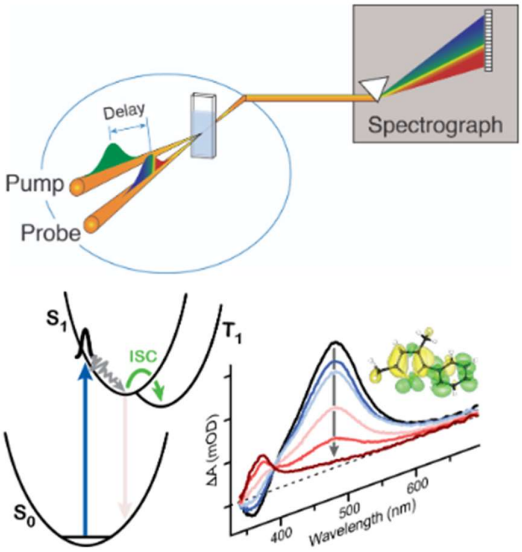

Figure 2.1: The diagram of the optical pump-probe transient absorption measurement [8].

By means of optical pump-probe transient absorption spectroscopy in the VIS-NIR region, Qianqian Ding and collaborators experimentally investigated the femtosecond-resolved plasmon-exciton interaction of graphene-Ag nanowire hybrids [11]. As another example, Petr A. Obraztsov and his co-workers reported the ultrafast light-induced absorbance change in CVD-grown multilayer graphene [12]. Using femtosecond pump−probe measurements in 1100−1800 nm spectral range, they revealed broadband absorbance change when the probe photon energy was higher than that of the pump photon. The observed phenomenon is interpreted in terms of the Auger recombination and impact ionization playing a significant role in the dynamics of photoexcited carriers in graphene.

2.2 Optical pump-probe reflection spectroscopy

Alternatively, the temporal evolution of optical properties can be also retrieved by detecting the transient changes in the reflectivity of the probe beam. A typical setup to measure transient reflection is shown in Fig. 2.2 [6]. In the specific case the experiment allows for the measurement of the reflectivity (R, blue curve) and and an extraction of optical conductivity σ (red curve) of in Nd_2CuO_4. The schematic of the experimental setup is illustrated in Fig. 2.2b. Pump and probe pulses are generated from a non-collinear optical

parametric amplifier. The cross-correlation profile (10 fs) of the pump and probe pulses is shown in Fig. 2.2c. The spectrum of the pulse is shown by the colored area in Fig. 2.2a, which is indeed located within the optical transition corresponding to the Mott-gap of Nd_2CuO_4. In some several cases, the technique has been employed to observe photoinduced change of the electronic states at high pumping fluence. S. Pagliara and his co-workers demonstrated that a renormalization of the π−π* band gap takes place when a UV-laser pulse excites a carrier density larger than 10% of the π* density of state in graphite, which has been achieved by detecting the transient reflectivity and the associated decay time of an infrared probe following the excitation of a UV pump pulse tuned across the π−π* absorption resonance [13]. The pump photon energy at which both the transient reflectivity and the decay time are maximum is downshifted by 500 meV with respect to the relative absorption maximum at equilibrium. This finding is interpreted as a transient π−π* band gap shrinking of similar magnitude, near the M point of the Brillouin zone.

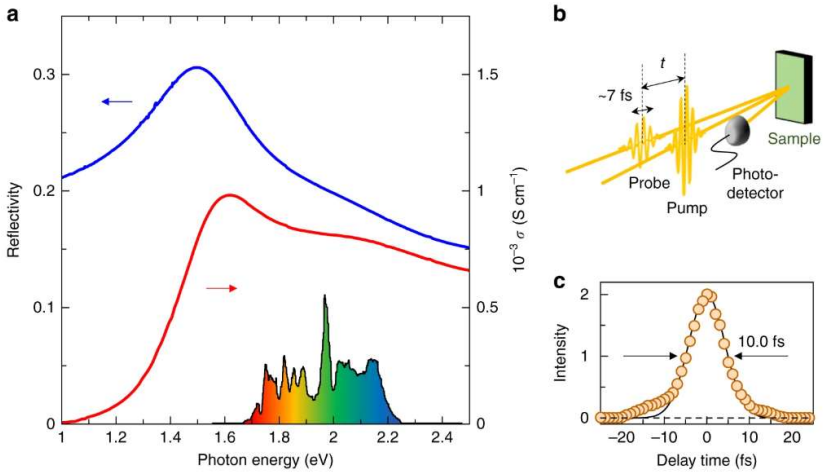

Figure 2.2: Schema of a pump-probe reflection setup and optical spectra of CuO_2 planes in Nd_2CuO_4 [6].

Other works investigates the response of topological materials. By using the time-resolved pump-probe reflectance (ΔR/R) measurement at room temperature under a strong optical pumping, Guohao Zhai and his cooperators explored the photoexcited hot carrier dynamics of a bulk single crystal Cd_3As_2 in the mid-IR region [14]. They analyzed the transient hot carrier redistribution upon a strong photoexcitation and the subsequent interband transitions combined the experimental ΔR/R results and theoretical model. They showed that the ΔR/R response of Cd_3As_2 has a complex behavior, due to the interplay of transitions between Dirac bands and transitions involving both the Dirac and non-Dirac bands. Throughout the mid-IR region measured, they found that ΔR/R is contributed

primarily by changes in the refractive index, rather than by changes in the extinction coefficient.

2.3 Time-resolved fluorescence spectroscopy

The time-resolved fluorescence spectroscopy is widely employed to understand photo-induced carrier's dynamics and recombination mechanisms in layered semiconductors. The most advanced setups make use of ultrafast streak cameras to digital count photons that are time-correlated in relation to a short excitation light pulse. An overview of the streaking technique to measure time resolved fluorescence is shown in Fig. 2.3 [15]. A pulse beam photoexcite the sample and the subsequent fluorescence is monitored as a function of time after excitation. Fluorescence lifetimes across the semiconductor bandgap and or from trapped states are typically occurring in the time spectral region ranging from picoseconds to nanoseconds. By making use of the time-resolved fluorescence spectroscopy, H. Fang and his cooperators [16] demonstrated that the exciton radiative rate in some van der Waals heterostructures such as $MoSe_2$ in hexagonal boron nitride (hBN) can be tailored by a simple change of the hBN encapsulation layer thickness, as a consequence of the Purcell effect. The time- resolved photoluminescence measurements showed that spontaneous emission time of neutral excitons can be tuned by one order of magnitude depending on the thickness of the surrounding hBN layers. Understanding the role of these electrodynamical effects is important to predict the complex dynamics of relaxation and recombination for both neutral and charged excitons. On a practical level, monochromatic TMD-based emitters would be beneficial for low-dimensional devices, but this challenge is yet to be resolved. Indeed, the photoluminescence spectra of TMD monolayers display a large number of features that are particularly challenging to decipher. In their work Lorchat's and colleagues showed that graphene, directly stacked onto TMD monolayers, enables single and narrow-line photoluminescence arising solely from TMD neutral excitons [17]. The authors thought this filtering effect stems from complete charge neutralization of the TMD by graphene, combined to selective non-radiative transfer of some long-lived excitonic species to graphene. These measurements proved that monolayer electroluminescent systems could emit visible and near-infrared photons with linewidths approaching the homogeneous limit.

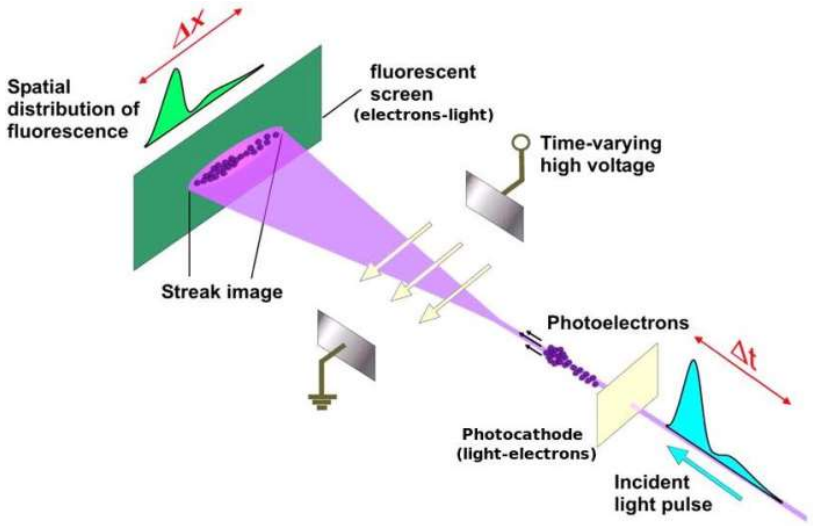

Figure 2.3: The diagram of time resolved fluorescence spectroscopy [15].

2.4 THz emission spectroscopy

Terahertz (THz) electromagnetic radiation have experienced a large development in recent years [18-22]. It is not exaggeration to say that THz waves can be applied to survey numerous scientific areas, covering the structure analysis in solid state, the electron dynamics in atomic and molecular physics, the discovery of the fundamental building blocks of life in medicine and life sciences, the composition distinguishing in chemistry and the security test in military matters. The frequency range of terahertz radiation, lies between the microwave and infrared regions of the electromagnetic spectrum. Some scientists refer to the range of 0.1–10 THz in frequency as terahertz radiation while others extend this range to frequency as long as 30 THz [23]. Sources of THz radiation can roughly be divided into two categories; broadband sources which are typically based on the conversion of ultrashort optical pulses into few cycle THz pulses and continuous wave (CW) sources which are spectrally very narrow. Herein, we just discuss broadband sources of THz radiation, in which an emitter is excited by a femtosecond driving pulse. The emitter can be a photoconductive antenna, a non-linear crystal for optical rectification or a multilayer with ferromagnetic materials and heavy metals [24, 25]. The THz detection is usually based on an electro-optic (EO) device. The birefringence induced by the THz pulse in the crystal is proportional to the THz electric field. Hence, the THz electric field information is encoded into the polarization state of the THz detection beam after going through the EO crystal. The polarization of the probe beam is further analyzed by a combination of a Wollaston prism and a balanced photodetectors. By scanning the delay of the THz detection beam, we are able to reconstruct the entire THz waveform. The main

experimental mechanism is described in Fig. 2.4. The impulsive and broadband THz pulse can be combined with an excitation beam in a pump probe configuration in order to obtain information about the dynamics of excited carriers and collective modes [26, 27].

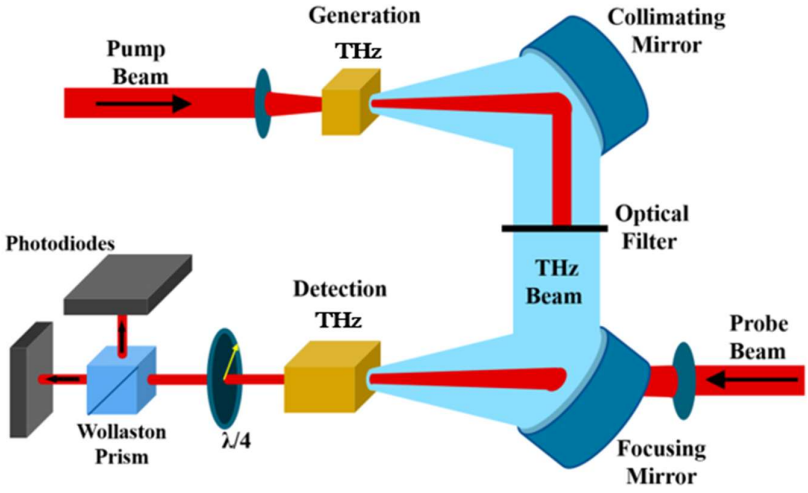

Figure 2.4: The diagram of THz emission spectroscopy.

2.5 Ultrafast photoelectrons spectroscopy

Finally, a complementary and powerful method to investigate photoexcited materials is ultrafast photoelectrons spectroscopy. The working principle of ultrafast photoelectrons spectroscopy is depicted in Fig. 2.5. In ARPES measurements, a photon beam induces the emission of electrons from a solid surface. The band structure of a crystalline solid is reconstructed by analyzing the emission angle and the kinetic energy of the photoemitted electrons. In the case of time resolved photoelectron spectroscopy, a pump pulse is absorbed by the surface, therefore creating a non-equilibrium state. A second pulse in the ultraviolet spectral range probes the photoexicted state via the photoemission process. This technique provides instantaneous photographs of the electronic states with temporal resolution better than 100 fs. The dynamics of the electronic states is obtained by changing the temporal delay between the pump and probe pulse. In recent years, such technique as notably improved, either accessing shorter pulse duration, tighter focusing or high energy resolution. Most important, time resolved photoelectron spectroscopy is capable of provide multi-dimensional information [28, 29], by detecting the electronic states as a function of their wavevector and therefore leading to a complete mapping of the band structure and of the occupation factor in a photoexcited state. Being this

technique the core of the present work, its detailed description will be presented in chapter 3.

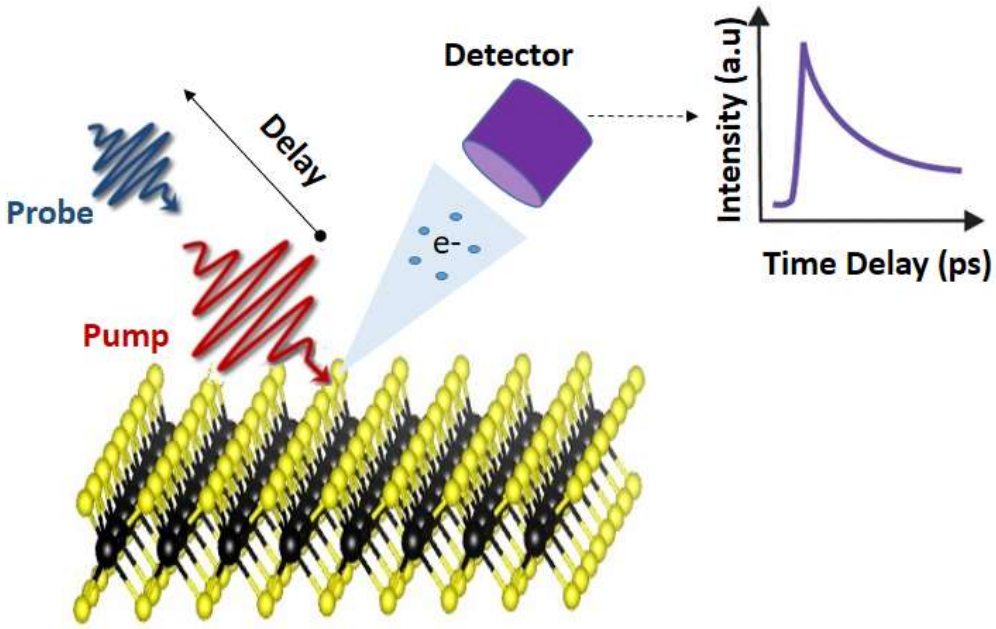

Figure 2.5: The diagram of ultrafast spectroscopy of layered materials (the crystal structure displayed in figure is TMDC).

References

[1] Kim, M., Xu, S.G., Berdyugin, A.I. et al. Control of electron-electron interaction in graphene by proximity screenings. *Nat Commun* **11**, 2339 (2020).

[2] Jiaojian Shi, Edoardo Baldini, Simone Latini, Shunsuke A. Sato, Yaqing Zhang, Brandt C. Pein, Pin-Chun Shen, Jing Kong, Angel Rubio, Nuh Gedik, and Keith A. Nelson, Room Temperature Terahertz Electroabsorption Modulation by Excitons in Monolayer Transition Metal Dichalcogenides. *Nano Lett*. **20**, 5214–5220, (2020).

[3] D. Bhattacharyya, Y. Zhang, C. G. Elles, and S. E. Bradforth, Electronic structure of liquid methanol and ethanol from polarization-dependent two-photon absorption spectroscopy. *J. Phys. Chem. A*, **123**, 5789 (2019).

[4] Claudio Giannettia, Massimo Caponeb, Daniele Faustic, Michele Fabriziob, Fulvio Parmigiani. Ultrafast optical spectroscopy of strongly correlated materials and high-temperature superconductors: a non-equilibrium approach. *Advances in Physics* **65** (58-238), (2016).

[5] Zong, A., Kogar, A., Bie, YQ. et al. Evidence for topological defects in a photoinduced phase transition. *Nature Phys* **15**, 27–31 (2019).

[6] Miyamoto, T., Matsui, Y., Terashige, T. et al. Probing ultrafast spin-relaxation and precession dynamics in a cuprate Mott insulator with seven-femtosecond optical pulses. *Nat Commun* **9**, 3948 (2018).

[7] Pu-Ting Dong & Ji-Xin Cheng. Pump–Probe Microscopy: Theory, Instrumentation, and Applications. *Spectroscopy* **32**(4) 2017.

[8] Berera R, van Grondelle R, Kennis JT. Ultrafast transient absorption spectroscopy: principles and application to photosynthetic systems. Photosynth Res. 101(2-3):105-18 (2009).

[9] Mark Forster, Daniel W. F. Cheung, Adrian M. Gardner and Alexander J. Cowan. Potential and pitfalls: On the use of transient absorption spectroscopy for in situ and operando studies of photoelectrodes. *J. Chem. Phys*. **153**, 150901 (2020).

[10] K. E. Knowles , M. D. Koch and J. L. Shelton , Three applications of ultrafast transient absorption spectroscopy of semiconductor thin films: spectroelectrochemistry, microscopy, and identification of thermal contributions. *J. Mater. Chem. C* **6**, 11853 —11867 (2018).

[11] Ding, Q., Shi, Y., Chen, M. et al. Ultrafast Dynamics of Plasmon-Exciton Interaction of Ag Nanowire- Graphene Hybrids for Surface Catalytic Reactions. *Sci Rep* **6**, 32724 (2016).

[12] Obraztsov, P. A. et al. Broadband light-induced absorbance change in multilayer graphene. *Nano Lett.* **11**, 1540 (2011).

[13] S. Pagliara, G. Galimberti, S. Mor, M. Montagnese, G. Ferrini, M. S. Grandi, P. Galinetto, and F. Parmigiani. Photoinduced π−π* Band Gap Renormalization in Graphite. *J. Am. Chen. Soc*. **133**, 6318 (2011).

[14] Guihao Zhai, Chaoyang Ma, Junsen Xiang, Jialiang Ye, Ting Li, Ying Li, Peijie Sun, Genfu Chen, Xiaoguang Wu, Xinhui Zhang. Mid-infrared transient reflectance study of the Dirac semimetal Cd3As2 under strong optical pumping. *Physical Review B* **101** (17) (2020).

[15] Shah, Jagdeep. Ultrafast Spectroscopy of Semiconductors and Semiconductor Nanostructures. Springer, Berlin, Germany, 1999.

[16] H. H. Fang, B. Han, C. Robert, M. A. Semina, D. Lagarde, E. Courtade, T. Taniguchi, K. Watanabe, T. Amand, B. Urbaszek, M. M. Glazov, and X. Marie, Control of the Exciton Radiative Lifetime in Van der Waals Heterostructures. *Phys. Rev. Lett*. **123**, 067401 (2019).

[17] Lorchat, E., López, L.E.P., Robert, C. et al. Filtering the photoluminescence spectra of atomically thin semiconductors with graphene. *Nat. Nanotechnol*. **15**, 283–288 (2020).

[18] T. Seifert, S. Jaiswal, U. Martens, J. Hannegan, L. Braun, P. Maldonado, F. Freimuth, A. Kronenberg, J. Henrizi, I. Radu8, E. Beaurepaire, Y. Mokrousov, P. M. Oppeneer, M.

Jourdan, G. Jakob, D. Turchinovich, L. M. Hayden, M. Wolf, M. Münzenberg, M. Kläui and T. Kampfrath*, Efficient metallic spintronic emitters of ultrabroadband terahertz radiation. *Nature Photonics*. **10**, 483-488 (2016).

[19] Ulbricht, R., Hendry, E., Shan, J., Heinz, T. & Bonn, M. Carrier dynamics in semiconductors studied with time-resolved terahertz spectroscopy. *Rev. Mod. Phys*. **83**, 543–586 (2011).

[20] Kampfrath, T., Tanaka, K. & Nelson, K. Resonant and nonresonant control over matter and light by intense terahertz transients. *Nature Photon*. **7**, 680–690 (2013).

[21] Chan. W, Deibel, J.&Mittleman, D. Imaging with terahertz radiation. *Rep. Prog. Phys*. **70**, 1325–1379 (2007).

[22] Zeitler, J.etal. Terahertz pulsed spectroscopy and imaging in the pharmaceutical setting—a review. *J. Pharm. Pharmacol*. **59**, 209–223 (2007).

[23] E. Brüdermann, H.-W. Hübers, and M. F. Kimmitt, Terahertz Techniques (*Springer*, Heidelberg, 2011).

[24] Reimann, K. Table-top sources of ultrashort THz pulses. *Rep. Prog. Phys*. **70**, 1597–1632 (2007).

[25] Blanchard, F.etal. Generation of intense terahertz radiation via optical methods. IEEE J. Sel. Top. *Quantum Electron*. **17**, 5–16 (2011).

[26] Luo, L., Yang, X., Liu, X. et al. Ultrafast manipulation of topologically enhanced surface transport driven by mid-infrared and terahertz pulses in Bi_2Se_3. *Nat Commun* **10**, 607 (2019).

[27] Fu, Z., Yamaguchi, M. Coherent Excitation of Optical Phonons in GaAs by Broadband Terahertz Pulses. *Sci Rep* **6**, 38264 (2016).

[28] Yao, B., Huang, S., Liu, Y. et al. Gate-tunable frequency combs in graphene–nitride microresonators. *Nature* **558**, 410–414 (2018).

[29] Gerber, S., Kim, K., Zhang, Y. et al. Direct characterization of photoinduced lattice dynamics in $BaFe_2As_2$. *Nat Commun* **6**, 7377 (2015).

Chapter 3 Time and Angle-resolved Photoemission Spectroscopy

3.1 Angle Resolved Photoemission Spectroscopy (ARPES)

Probably, the most important and widely used experimental technique to gain information about occupied electronic states is Angle Resolved Photoelectron Spectroscopy (ARPES) [1-3]. The goal of an ARPES experiment is to derive the single particle excitations of the investigated system by measuring the energy and momentum of excited photoelectrons. Fig. 3.1 exhibits the basic principle of an ARPES experiment. The photoelectrons are produced exposing the sample to monochromatic light of energy $h\square$. The important parameters to be measured are their kinetic energy E_p and their angles θ and φ of emission with respect to the surface normal.

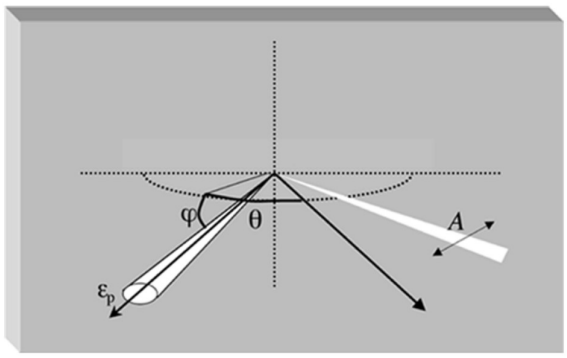

Figure 3.1: schematic geometry of an ARPES experiment. E_p is the kinetic energy of the photoelectrons and (θ,φ) are their angles of emission.

Obviously the photoelectrons may scatter many times before leaving the solid. Most of the interacting channels of these light charged particles are strongly inelastic. Consequently, the ARPES signal has two distinct components: a shapeless background produced by multiple scattering events, and a primary photocurrent produced by electrons that do not scatter at all. Remarkably, the primary component dominates the low energy excitations, and can be extracted from the inelastic background.

The universal curve of the mean free path of primary photoelectrons in the relevant energy range for photoemission is displayed in Fig. 3.2. One can see that the mean free path is about one atomic layer when the electron kinetic energy is roughly 50 eV, and increase to few nanometers if the photons are Hard-X rays or are around 1 eV above the work function. Thus, the typical synchrotron-based ARPES is more surface sensitive than the laser-based ARPES.

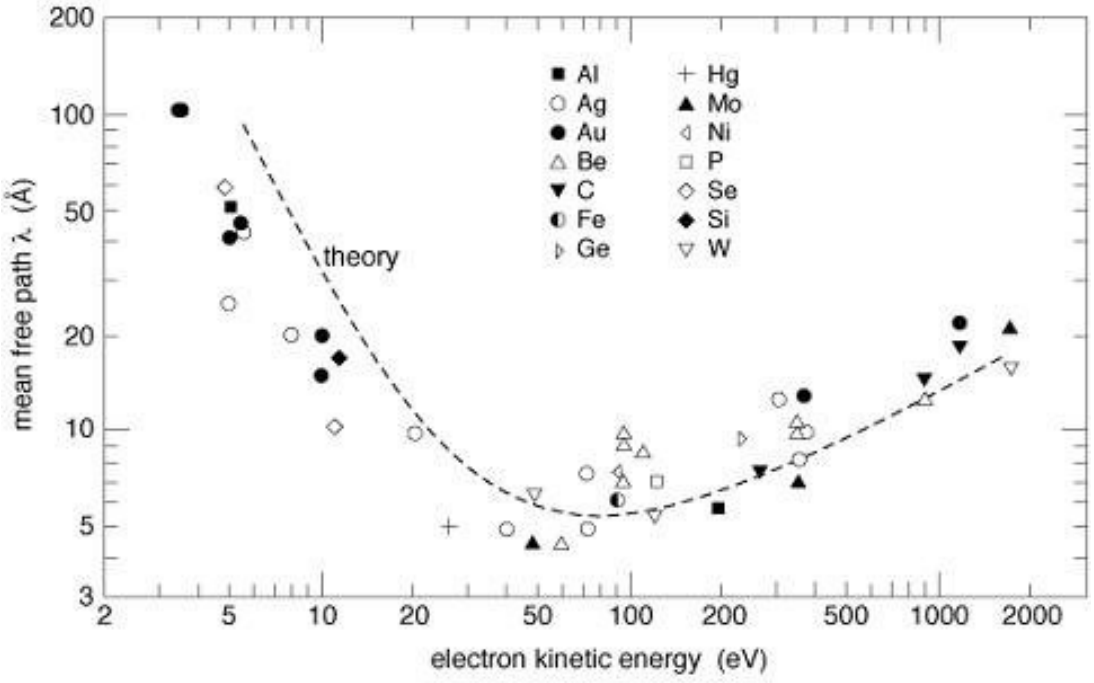

Figure 3.2: Universal curve of the mean free path of electrons in common materials.

Since this signal characterize photoelectrons with a short mean free path, any relation to the bulk properties, assumes the absence of surface reconstruction. Once this is established, photoemission represents the most direct and powerful tool to explore the electronic properties of crystalline solids.

The main strength of the ARPES technique relies in the ability to reproduce the occupied band structure. Indeed, the unscattered photoelectron contains all the energetic information about the excited state left behind. An instructive scheme of the underlying process is presented in Fig. 3.3. Sample and spectrometer are in electrical contact. The chemical potential of this coupled system is separated from the vacuum level by the spectrometer work function Φ. The energy conservation of the primary process defines univocally the photohole binding energy by the identity

$$E_b = h\nu - \Phi - E_p$$

This relation implies that the photoemission event has to be treated as a coherent quantum-mechanical process.

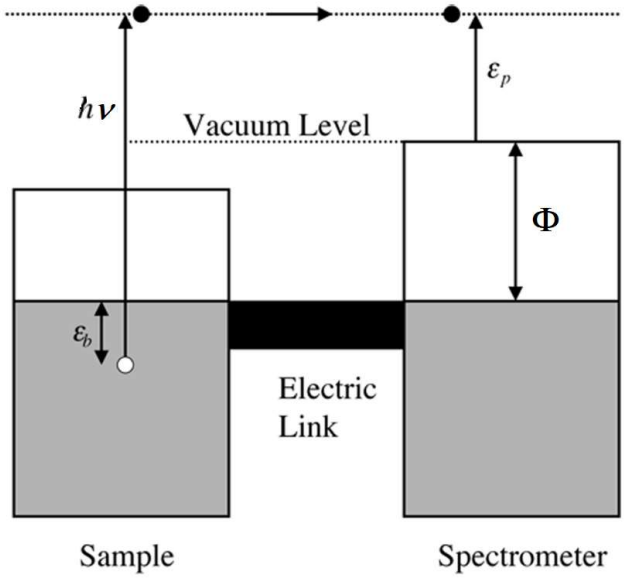

Figure 3.3: Energetic scheme of the photoemission experiment.

Obviously, the absorbed photon cannot provide a free electron with the adequate momentum to the respective energy gained. The missing wavevector must be supplied by another source, namely scattering with the crystal potential. These umklapps come in units of reciprocal lattice vectors ***G*** and impose an important selection rule. The large photoelectron momentum projects the final state into higher Brillouin zones. In a band model, this optical absorption would be a vertical transition from a filled band to an empty one. In reality the excitation is assisted by ***G*** umklapps. The physics of this angular dependence is very appealing. If one could measure at a given direction inside the solid, he could optically excite electrons of only one energy. Thus ARPES can be employed for a detailed mapping of the energy bands. However, there are some impediments to this procedure. Let's analyze more in detail the tunneling through the surface. The photohole can still be approximated by a Bloch state, whereas the photoelectron is a necessarily complex wavefunction. Indeed, the photoelectron is a plane wave in the vacuum and a damped combination of Bloch states inside the crystal. The parallel component of the wavevector is conserved but the perpendicular one is not. This limitation is not so stringent as it looks. Indeed, a photoelectron tunneling through the surface suffers a reduction of kinetic energy that may be reasonably distributed around a value V_0. By knowing the kinetic energy E_p and the polar angle θ, the photoelectron momentum parallel to the crystal surface $K_{||}$ can be obtained through the following equation:

$$K_{||} = [(2mE_p)/(\hbar)^2]^{1/2} \sin\theta = 0.512(E_p)^{1/2} \sin\theta$$

where m is the free electron mass and $\hbar$ is the Planck's constant. In addition, the x and y components of the in-plane momentum can be derived by

$$K_x = 0.512(E_{kin})^{1/2} \sin\theta \cos\varphi$$
$$K_y = 0.512(E_{kin})^{1/2} \sin\theta \sin\varphi$$

where φ is the azimuthal angle. Furthermore, the perpendicular (z) component of the free electron K_z in vacuum is given by the formula:

$$K_z = [(2mE_p)/(\hbar)^2]^{1/2} \cos\theta = 0.512(E_p)^{1/2} \cos\theta$$

The perpendicular (z) component of the electron K_z in a crystal can is given by:

$$K_z = 0.512[E_{kin} (\cos\theta)^2 + V_0]^{1/2}$$

In summary, the measured free electron kinetic energy and the angles are related to the crystal momentum in the following way:

$$K_x = 0.512(E_{kin})^{1/2} \sin\theta \cos\varphi$$
$$K_y = 0.512(E_{kin})^{1/2} \sin\theta \sin\varphi$$
$$K_z = 0.512[E_{kin} (\cos\theta)^2 + V_0]^{1/2}$$

3.2 Time-resolved ARPES

Time-resolved photoemission technique was first introduced in the 1980s to study the electron thermalization in metals and semiconductors [4-8]. Due to the advancement in ultrafast lasers techniques and the development of ARPES setup with parallel momentum detection, the laser-based ARPES has considerably developed, and is nowadays an essential tool to detect the carrier's dynamics in solid-state materials [9, 10]. Time-resolved ARPES experiments are currently applied to study the dynamics of electron, lattice and magnetic order in strongly correlated electron systems, low dimensional materials, topological insulators and superconductors [11-14]. Time-resolved ARPES is a stroboscopic pump probe technique. The probe beam is obtained from the fundamental of our laser source by non-linear optical processes in BBO crystals for our optical beams system [15]. The detailed introduction of this system will be in section 3.3.3.

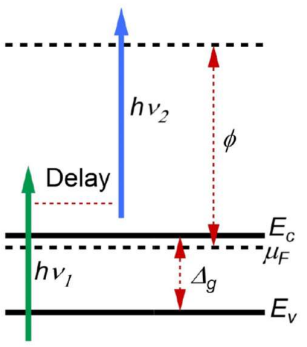

Figure 3.4: A time-resolved ARPES energy diagram. Here E_c is the bottom of the conduction band, E_v is the top of the valence band, E_F is the chemical potential, Φ is the

workfunction, $h\nu_1$ and $h\nu_2$ are the photon energy of the pump and probe beam, respectively.

Fig. 3.4 describes a typical experiment in a semiconducting material. A pump photon of energy $h\nu_1$ excite an electron from its initial state in the valence band towards an intermediate state. A second photon $h\nu_2$ reaches the sample after a variable delay time and promotes the excited electron out to the vacuum. The emitted photoelectron is then analyzed as a function of energy and wavevector. By this method, it is possible to perform time resolved spectroscopy both of the valence and conduction band states. By acquiring the ARPES spectra at various pump probe delay time, it is possible to retrieve a temporal evolution of the band structure and the transient occupation factor.

TrARPES is a powerful tool for the study of strongly correlated system because of its capability to disentangle the electron, lattice and spin degrees of freedom, which roots in its simultaneous detection of electron's energy and momentum in a time-resolved way. Figure 3.5 is a sketch of the main scattering process between different degrees of freedom as well as the characteristic timescale that are to them associated. For the electronic system, insights on the electron-electron and electron-phonon interactions can be obtained from the thermalization process [16, 17]. The direct optical transition at *t*=0 disrupts the thermal equilibrium and creates and transient occupation differing from the Fermi-Dirac distribution. Afterwards, the excited electrons inelastically scatter among themselves and with the phonon modes to return back to a thermalized distribution. Making Use of TrARPES, the distribution function as a function of time can be extracted from the photoelectron intensity maps [18-20]. There are also many other nonthermal processes that can be induced by a photoexcitation. If the pump beam beam is strong enough, the systems with spontaneously broken symmetries can experience a photoiduced phase transition. These phenomena have been currently observed in Peierls insulators, Mott insulators, magnetically ordered systems, and superconductors [21-25]. TrARPES provides an ideal tool to survey the relaxation and dynamics of these complex phases, helping the researchers gain insights on the most important interactions leading to a Fermi surface instability.

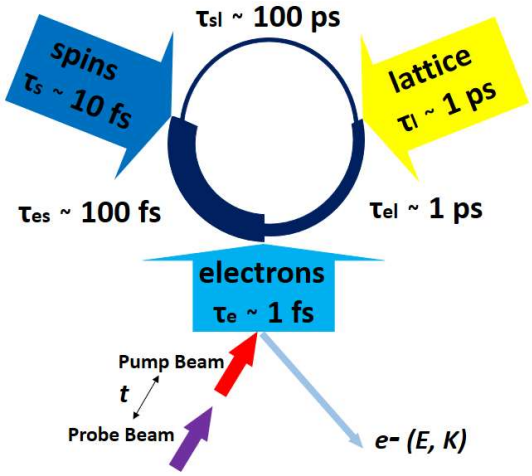

Figure 3.5: Interactions between the electron, spin and lattice degrees of freedom after the photons injection. The typical thermalization time scale is labelled inside the arrow standing for each subsystem. The magnitude of interactions between the subsystems are represented by the width of the circle. Both the pump and probe pulses couple to the electronic degree of freedom.

3.3 Experimental setup

3.3.1 Overview

In our experiments, we use a time-resolved optical setup based on Ti-Sapphire laser system with a state of the art ARPES setup. The experimental system can be divided in three major parts: the laser source; the optics for generating ultraviolet (UV) and scanning time-delay; and three ultra-high-vacuum (UHV) chambers equipped with instruments of surface preparation or surface analysis. Fig. 3.6 shows an overall diagram of our time-resolved ARPES setup.

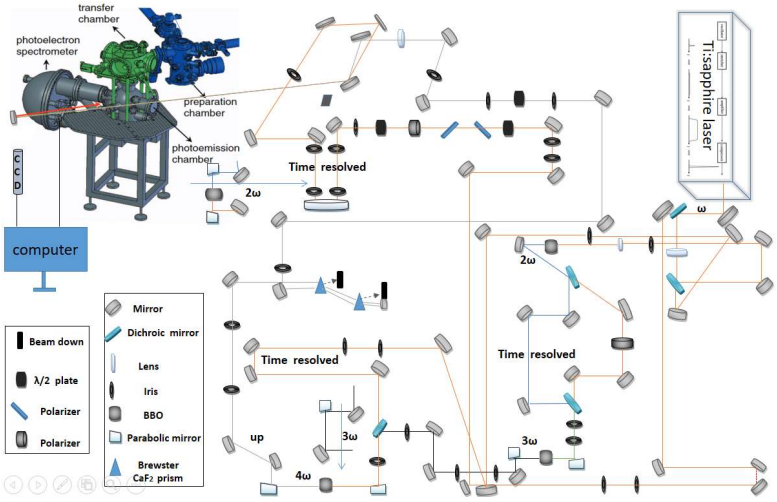

Figure 3.6: The diagram of our laser-based time-resolved ARPES setup.

Our laser source is a Regenerative amplifier from the COHERENT company. The details about the laser system will be described in Section 3.3.2. In order to generate 4ω light which is suitable for TrARPES, we use three β-barium borate (BBO or β-BaB_2O_4) crystals for manipulating the frequency of light. In addition, half-wave plates and polarizers are employed to adjust the powers of the pump beam and probe beam in our measurements. The polarizer passes horizontal polarization and reflects vertical polarization. The angle of the half-wave plate determines the ratio of the two orthogonal polarizations and thus distributes the transmission and reflection power. The nonlinear physics involved will be described in Section 3.3.3. In experiments, two light beams as pump-probe sources are needed to achieve the TrARPES measurements. Furthermore, a charge-coupled device (CCD) is used to check if two beams are spatially overlapped on a scintillator that map the sample postion into the UHV photoemission chamber. The photoelectrons emitted by the laser beams are be collected and analyzed by a hemispherical analyzer. The UHV system will be described in Section 3.3.4.

3.3.2 Ultrafast laser system for TrARPES

Figure 3.7 shows our commercial Ti:Sapphire laser system (RegA by Coherent) delivering 6μJ per pulse with 50 fs duration at FWHM (Full Width Half Maximum) at 250 kHz repetition rate. The laser wavelength can be tuned between 780 nm and 820 nm for a safe and stable operation. The short laser pulses are generated by a technique called mode-locking in a Ti:Sapphire Micra oscillator. The Oscillator is pumped by a continuous wave laser providing 5 Watts at 532nm. Such beam is obtained by splitting the output of Verdi 18 (which is a frequency doubled diode laser). The optical cavity of the Micra oscillator is confined by two end-mirrors. The allowed modes are those that form standing waves in the cavity and have frequency separation equal to the inverse of the round-trip time. The number of that can be effectively populated is determined by the bandwidth of the gain medium, which is the Ti:Sapphire crystal, and by the cavity losses. Without the mode-locking, only one of these modes gets macroscopically populated and results in a lasing output. However, due to the optical Kerr effect, a spontaneous mode looking takes place when the cavity is properly aligned. In this case many modes get macroscopically populated in locked in phase, thereby generating a soliton that we call pulse. This mode locking operation is forced and actively stabilized by an acoustic-optic modulator that shakes the output coupler at a frequency equal to the round-trip time (namely one over the repetition rate of the Micra).

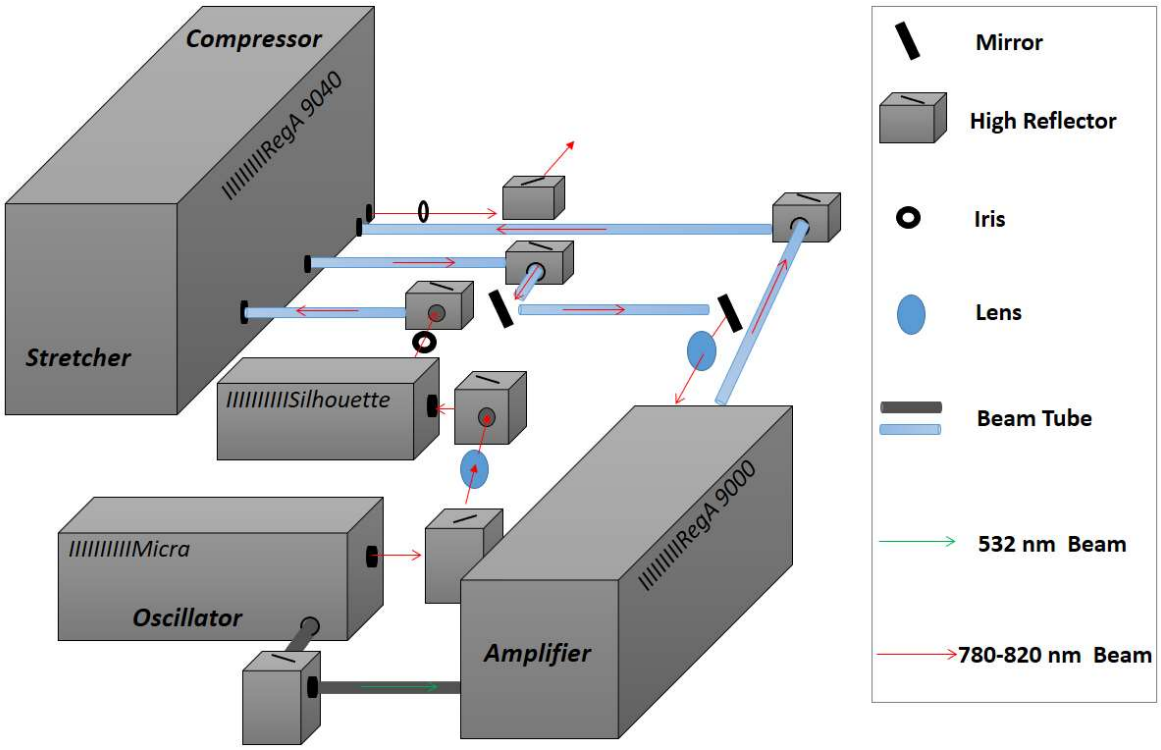

Figure 3.7: The diagram of our ultrafast laser system.

The pulses generated by the Micra is then sent to the silhouette that is a pulse shaper based on liquid crystals. The Silhouette is a single device that measures and manipulates the spectral phase and amplitude of ultrafast pulses. First, the Silhouette modifies the spectral amplitudes to change the pulse bandwidth. Second, it compensates for spectral phase distortions to achieve a transform-limited pulse. Third, it may introduce the spectral phase optimal for a particular ultrafast pulse application. Pulse shaping has been applied to many processes requiring laser pulse shaping such as compression of pulses generated by optical parametric amplifier (OPA) output, high order harmonic generation, dissociative ionization etc. In multi-photon microscopy experiments, Silhouette can compensate for unwanted phase distortions at the focus of the microscopy and it can optimally shape the pulses for selective excitation of different samples. In molecular dynamics, Silhouette can produce double pulses to enable fast interrogation of wave packets.

The pulses outcoming from the silhouette, are sent to the stretcher made of a multipass grating system, where they are temporally chirped to roughly 100 ps. The reduced peak energy in a broadened pulse avoids damaging to the gain medium in the amplifier. These broadened ‘seed’ pulses enter the regen cavity for amplification. The regenerative amplifier works as follow: the 12 Watts of Verdi 18 laser (532 nm center wavelength)

excites the Ti:Sapphire crystal of the regenerative amplifier, creating a population inversion. An acoustic-optic modulator injects some of the oscillator pulses in the cavity of the Regenerative amplifier. The seed photons induce stimulated emission of identical photons as they go through the crystal, so that the amplification is achieved. The same acoustic-optic modulator ejects the amplified pulses from the amplifier cavity and send them into the compressor. Here a multipass grating system very similar to the stretcher compresses the pulses to 50 fs Full Width Half Maximum. At the output the pulse energy is 6 microJoules and the repetition rate is 250 KHz. Figure 3.8 illustrates the multiple steps of the amplification process.

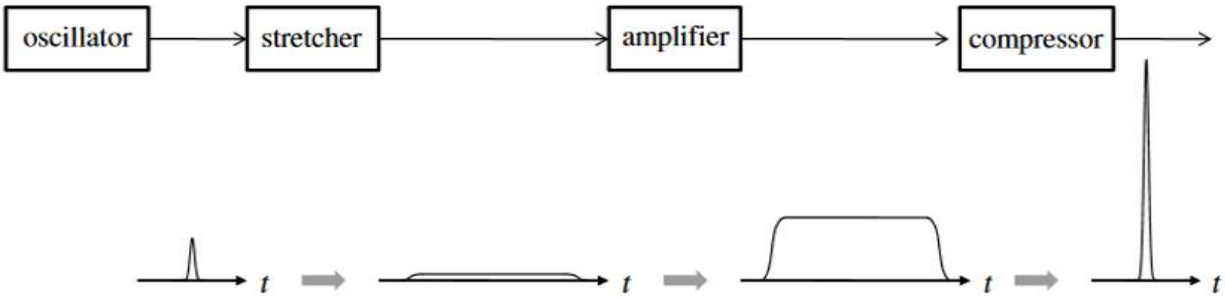

Figure 3.8: The illustrative diagram of our ultrafast laser system.

3.3.3 Optical beamlines for TrARPES

In order to perform TrARPES experiments, it is necessary to generate the 2th , 3th and, 4th harmonic of the laser beam. Figure 3.9 depicts the beam line that we employ in order to generate the harmonics. One fourth of the total beam power outcoming from of the laser system at ω=790 nm is focused in a 200 μm thick BBO crystal (cutting angle: $\theta = 29.2°$) using a focusing lens with the focal length of f = 20 cm to generate the second harmonic (SH) beam. Afterwards, a pair of dichroic mirrors (thickness, 1 mm) split and recombine the ω and 2ω beams in order to match their relative temporal delay. The ω and 2ω beams are then focused by an off-axis parabolic mirror onto a 50μm thick BBO crystal ($\theta = 44.3°$) to produce the 3th harmonic beam. Frequency mixing calculations indicate that the group velocity mismatch can be neglected in such thin crystals and the pulse duration should stay close to 50 fs [15]. The outcoming 3th harmonic is collimated by a parabolic mirror and isolated from the 2th harmonic via dichroic mirror. The 3th harmonic and part of the fundamental are focused on a 20μm thick BBO crystal ($\theta = 64.8°$) to generate the 4th beam. In the whole frequency mixing processes, delay lines with micrometer precision permit the precise temporal overlap of the beams, all beams are focused by reflective mirrors in order to avoid dispersion and a strictly collinear geometry for the frequency mixing stages is employed. As shown in Fig. 3.9, either the 3th or the 4th harmonic can be employed as

probe pulse. Since the beams have to pass dispersing MgO window, their group velocity dispersion is pre-compensated by prims compressors in Breustel angle configuration. Furthermore, they can be spatially and temporally characterized in great detail. The focus is imaged via a scintillator, behind an objective mounted on a CCD camera. An ocean optics spectrometer is employed to acquire a frequency spectrum. Finally, a cross correlation between the probe beam and the fundamental generate a frequency difference beam that is detected by means of a photomultiplier tube connected to a lock-in amplifier. The CCD camera is routinely employed to check the spatial overlap between the pump and probe beam. The intensity variations of the probe beam are also measured in real time during the measurement via a back reflection from the MgO window, that passed thought an optical chopper and measured via a calibrated Silicon photodiode connected to a DSP Lock-In Amplifier (MODEL SR830).

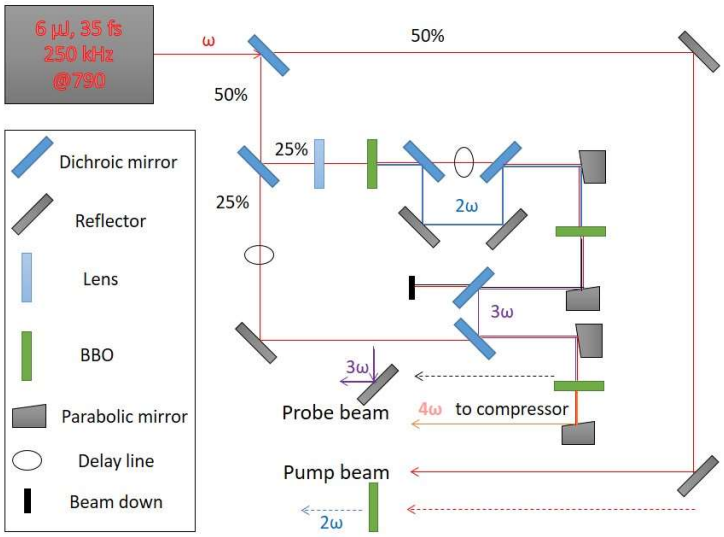

Figure 3.9: Schematic for FH generation by frequency mixing.

The 4th harmonic at 6.28 eV is the beam that we employ most commonly in our experiments. By making using of this beam we have access to a reasonably large portion of the Brillouin zone in many of the interesting systems. The repetition rate of 250 KHz provide high photon flux of 10^{13} photons/s as well as relative low photons per pulse. This optimal combination mitigates space charge effects and save time of data acquisition.

3.3.4 The ultra-high-vacuum (UHV) chambers and the analyzer for TrARPES

As displayed in Fig. 2.10, our vacuum system consists of a load-lock chamber that is used to load a sample from an atmosphere environment, a preparation chamber, a transfer chamber and a photoemission chamber connected to the photoelectron spectrometer. The

low base pressure in the ultra-high-vacuum system is essential to keep the cleaved surface for a crystal clean for a long time. We use primary pumps and turbo pumps to make the UHV system reach high vacuum. In the preparation and measurement chamber ion pumps and Titanium sublimator pumps further improve the base pressure. In the usual conditions, the pressures are: 10^{-8} mbar in the load-lock chamber, $5x10^{-10}$ mbar in our preparation chamber; $1x10^{-10}$ mbar in the transfer chamber and $5x10^{-11}$ mbar in the photoemission chamber.

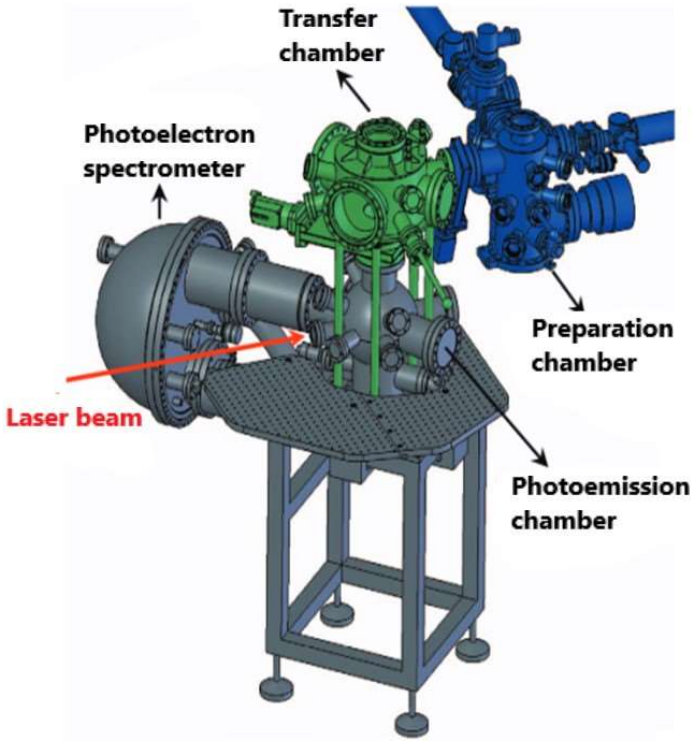

Figure 3.10: A 3D view of the experimental chambers and of the ARPES analyzer [15].

Several steps are routinely done before each measurement. The sample is inserted in the load-lock and is this small entry chamber is pumped until the pressure reaches 10^{-8} mbar. Then, the sample is transferred to the preparation chamber, where different operations are possible. The clean surface of a layered crystal is obtained by cleaving the sample by means of a wobble stick. In the case of non-layered material, sputtering and annealing cycles are necessary in order to obtain a clean surface. The preparation chamber is equipped with an Ar gun for sputtering and e-beam heater for annealing. In the case of ion-sputtering, a partial pressure of of 10^{-5} mbar of argon is injected in the sputter gun via a precision leak-valve. A DC current (~4.5 A) is passed through the filament of the sputter gun, yielding thermal emission of electrons (~10 mA). While the filament is grounded, a positive voltage of roughly +0.8 kV is applied to the grid of ion sputtering. Thermally

emitted electrons are accelerated toward the grid and generate positive Ar ions through impact ionization. In order to accelerate the positive ions toward the scanning probe, a negative voltage on the order of −2.0 kV is applied to the tip of the sputtering device, resulting in a measurable ion current of several microamperes. The bombardment by means of energetic Ar ions removes residual impurities from the surface. Then, the annealing to high temperature induce an ordering of the surface atoms that is compatible with the underlying crystal structure. After several sputtering and annealing cycles, a clean and well-ordered surface of the crystal can be obtained [26].

After the suitable preparation steps, the sample is mounted on the cryogenic manipulator of the transfer chamber. In the transfer chamber, a low energy electron diffraction (LEED) setup can be employed to verify the crystalline quality of the surface. Moreover, important information can be obtained about a possible surface reconstruction. As in all diffraction experiments, the determination of an atomic structure is naturally divided into two parts: the first is the determination of the periodicity of the system and thus the basic surface unit cell, and the second is the location of the atoms within this unit cell. The first part, the evaluation of the surface unit mesh is straightforward and involves simple measurements of symmetry and spot separation in the diffraction pattern. Since the diffraction pattern corresponds essentially to the surface reciprocal lattice, the reverse transformation yields the periodicity in real space. Instead, the determination of atomic coordinates, requires a detailed measurement of diffracted intensities. The LEED technique is frequently used for this purpose, even though the theoretical problem of deriving an atomic structure from the measured intensities is far from simple, due to the “strong” interaction of slow electrons with a solid. The standard experimental set up for LEED consists of an electron gun to produce an electron beam with primary energies in the range of 20–500 eV and a display system for observing the Bragg diffraction spots. The energy range below 300 eV is particularly suited to surface studies since the mean-free path of these slow electrons in the solid is short enough to give good surface sensitivity. Furthermore, according to the de Broglie relation: $\lambda = (150.4/ E)^{1/2}$, where λ in Å and E in eV, typical LEED wavelengths are in the Ångstrom range, comparable with wavelengths used in X-ray crystallography, and of the same magnitude as the interatomic distances in a solid.

Figure 3.11 shows the components of a typical three-grid LEED system. The electron gun unit consists of a directly or indirectly heated filament with a Wehnelt cylinder W followed by an electrostatic lens with apertures A, B, C, D. The acceleration energy (20–500 eV) is determined by the potential between the cathode and apertures A and D. Apertures B and C have potentials intermediate between A and D and are used to focus the electron beam.

Initial collimation is achieved by the Wehnelt cylinder which has a somewhat negative bias with respect to the cathode filament (LaB_6). The last aperture D, also called the drift tube, is usually at the same (earth) potential of the aperture A and of the sample; the same is true for the first and last grids in front of the fluorescent screen. Thus a field-free space is established between the sample and the display system through which the electrons travel to the surface and back after scattering. The fluorescent screen (collector) has to be biased positively (5-7 kV) in order to achieve a final acceleration of the slow electrons; only high-energy electrons owing to elastic scattering can be made visible on the screen. Besides elastic scattering, inelastic scattering also occurs at the sample surface, therefore giving rise to electrons of lower energy. These electrons are scattered through wide angles and produce a relatively homogeneous background illumination of the phosphor screen. This background illumination is suppressed, by giving the middle grid a somewhat negative bias. The inelastically scattered electrons are thus prevented from reaching the collector. The emission current of standard equipment is on the order of 1μA; it varies with primary energy but electronic stabilization may be used to fix its value. The energy spread is about 0.5 eV, attributable mainly to the thermal energy distribution. The diameter of the primary beam is on the order of 1 mm. In addition, the current density of ≈ 1 μA in the primary beam is rather high. Thus organic adsorbates and clean semiconductor surfaces may suffer severe damage.

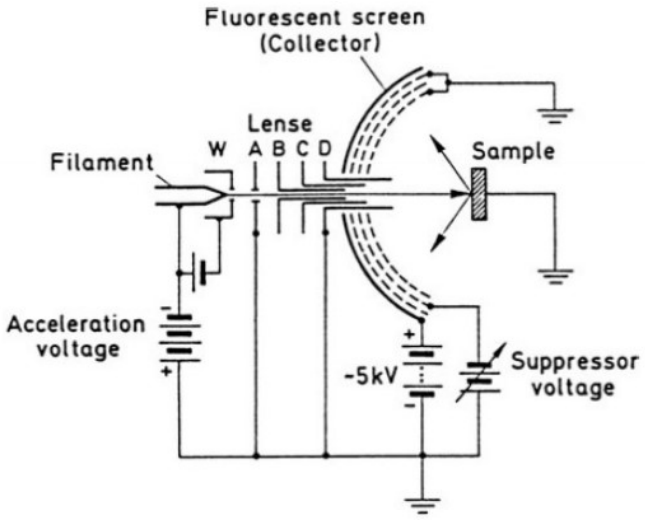

Figure 3.11: Schematic of a three-grid LEED optics for electron diffraction experiments. The integrated electron gun consists of a heated filament, a Wehnelt cylinder (W) and the electron optics containing the apertures A–D. B and C are usually held at potentials between those of A and D.

Note that the primary electron beam deviates from an ideal plane wave $A\exp(ik\cdot r)$, but is a mixture of waves of slightly different energy and direction. These deviations from the ideal direction and energy are caused by the finite energetic width ΔE (thermal width ≈ 500 meV) and the angular spread 2β of the beam. The electrons impinging on the crystal surface exhibit therefore slight random variations in phase; if two spots on the surface have too large a separation, the incoming waves cannot be considered as coherent. The phases are not correlated and the outgoing waves cannot interfere to produce a diffraction pattern. There is a characteristic length called coherence length such that atoms in the surface within a coherence length (or radius) can be considered as illuminated by a simple plane wave. Waves scattered from points separated by more than a coherence radius add in intensity rather than in amplitude. Thus no surface structure on a scale larger than the coherence length forms a diffraction pattern. The two contributions responsible for limiting the coherence are the finite energy width ΔE and the angular spread 2β, giving rise to incoherence in time and space, respectively. The coherence radius is given by the following equation

$$\Delta r_c = \frac{\lambda}{2\beta\sqrt{1+(\Delta E|2E)^2}},$$

where λ in a standard LEED experiment, the angular width of the primary beam is $\approx 10^{-2}$ rad with an energy spread of ≈0.5 eV. At a primary energy of ≈100 eV this leads to a coherence length of about 100 Å.

Alkali metal	Content (mg)			Start of evaporation (Amp)		
	A =12 mm	A=17 mm	A=25 mm	Average	Standard Deviation	
Caesium Cs	5.2	7.3	10.8	4.7	0.2	Standard Production
Potassium K	2.9	4.1	6.0	5.3	0.2	
Sodium Na	1.7	2.4	3.5	6.0	0.2	
Rubidium Rb	4.5	6.4	9.4	5.3	0.2	Only on Request
Lithium Li	0.8	1.1	1.7	7.3	0.2	

Table 3.1 (A is active length)

We show in Fig. 3.12 a picture of the interior of the transfer chamber. The transfer chamber is also equipped with effusion cells for the evaporation of alkali metals. This source has to be carefully degassed and then approached to a distance of roughly 5 cm from the sample. The evaporation of the alkali metal is obtained by a resistive heating of the getter cartridge with the nominal current value. The typical parameters employed

during these processes depend to the alkali metal and are shown in Table 3.1. The important applications of such doping method of the surface will be detailed in chapters 5, 6 and 7.

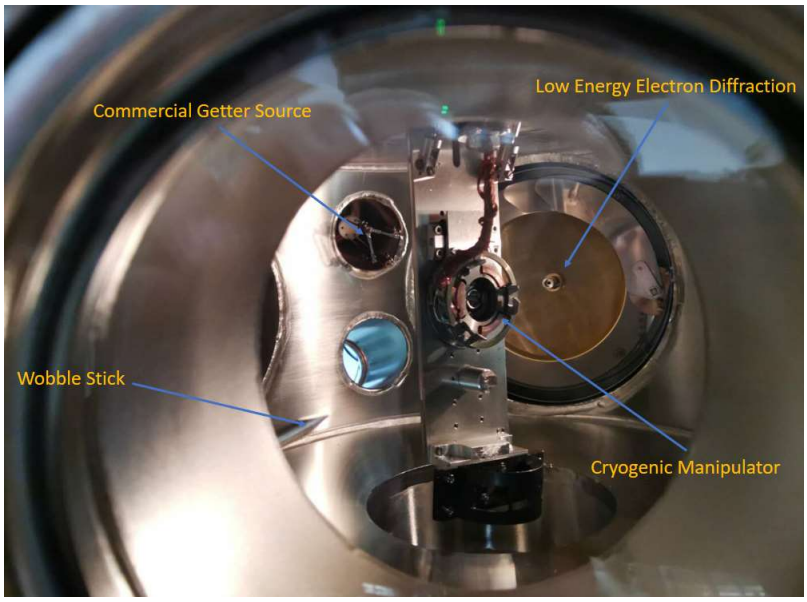

Figure 3.12: A picture showing the interior of the transfer chamber.

The sample is mounted on a cryogenic manipulator that has three translations (x, y, z) and two rotations, horizontal tilt, and azimuth (θ, φ). The sample can be cooled down to 35 K using liquid helium, down to 130 K using liquid nitrogen and can also be heated to 800 K, allowing us to perform experiments in various temperature conditions. Opening a valve is possible to lower the sample position from the transfer chamber to the measurement position. This allows to perform the alkaline evaporation steps, the LEED Characterization and the photoemission measurement keeping stable the temperature at the desired value and minimizing the unavoidable degassing during transfer processes.

Since we aim to measure photoelectrons with low kinetic energy, it is essential to have a good shielding from residual electric field and magnetic fields. Therefore, all components employed in the photoemission chamber are conductive. The photoemission chamber itself is made of μ-metal alloy, which has very high magnetic susceptibility. The photoemission chamber is also connected to a plasma discharge UV He lamp, which can be used to perform conventional static photoemission at 21.21 eV. This continuous source is routinely employed to check the quality of the sample and to obtain a band mapping of the full Brillouin zone in thermal equilibrium conditions.

The electron energy analyzer map in parallel the energy and emission angle of the photoelectrons on the position of a multichanneltron array. The electrostatic lenses that are in front of the hemisphere collimate the photoelectrons, convert emission angle into lateral position at the entrance slit of the analyzer and accelerate the electrons to a typical pass energy of 10 eV. The different kinetic energies are dispersed along the radial direction of the spheres as they traverse the vacuum space between the two concentric spheres, which have a voltage difference appropriate to the pass energy of the photoelectrons. As a result, energy and angles are dispersed on two perpendicular axes. The photoelectrons passing the hemispheres hit the multichanneltron and generate amplified flux that induce luminescence on a phosphorous screen. A Peltier cooled CCD camera is employed to record the photoluminescence image and convert the data in a digital map that is sent to the computer. Our photoelectron spectrometer, it is a commercial hemispherical electron analyzer (Phoibos 150, Specs) providing angular resolution better than 0.1° and an energy resolution of about <10 meV. As shown in Fig. 3.13, the entrance slit selects out photoelectrons with a given azimuthal angle. To obtain a complete mapping of the in-plane momentum, the sample is rotated relative to the detector for a scan.

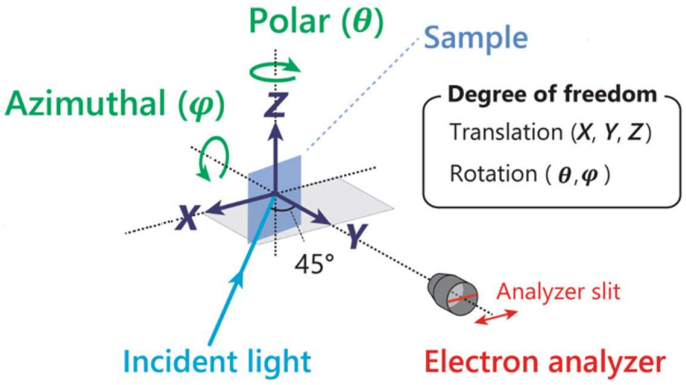

Figure 3.13: Schematic inside the photoemission chamber and spectrometer.

Our measurements are fully computer controlled and all instruments are driven by a homemade LabVIEW program. The program is able to acquire data while moving the manipulator and the translation stage of the delay line that is used for pump-probe experiments. This allows us to acquire automatically and in a consistent manner a large amounts of data. Spending the minimal amount of time for data acquisition is important since the temporal scans can be time consuming and require good laser stability. Two screenshots of the program window during a typical acquisition are shown in the Fig. 3.14.

For the data analysis, we make use of the IGOR Pro software, which is the most employed in the ARPES community.

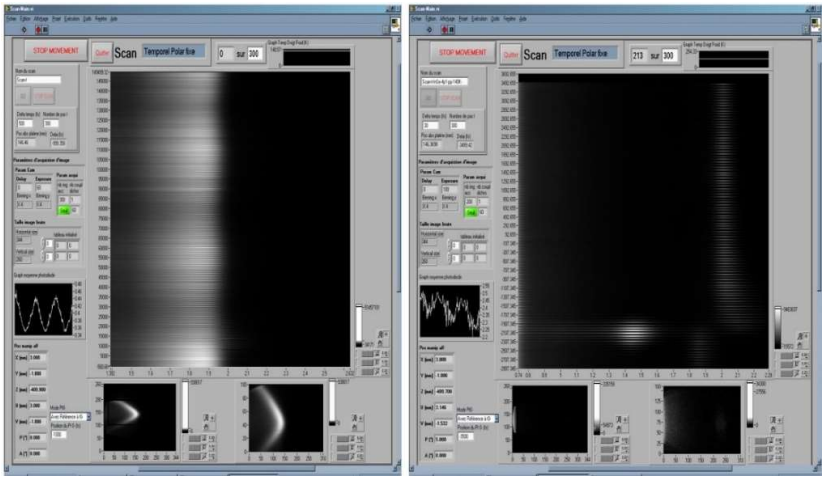

Figure 3.14: Two photos about the program service condition.

3.3.5 Sample preparation, sample loading and sample cleaving

A careful sample preparation is very important for TrARPES measurements because of the stringent requirement on surface cleanness and homogeneity. Our samples are single crystals purchased from external companies or obtained in the context of collaborations with other laboratories. When we have to cleave the crystal, the sample is glued on our sample holder with silver epoxy or Torr Seal glue. In principle, the sample needs to be heated to 100°C for 1 hour with a heater (SB160, by Stuart) when we employ silver epoxy. Then we glue a ceramic post and cover the whole with graphite coating. This ensures that all material around the cleaved surface is conductive, so to avoid charging effects during photoemission (see also Fig. 3.15). We use a microscope (By BRESSER) to check each step of the sample preparation.

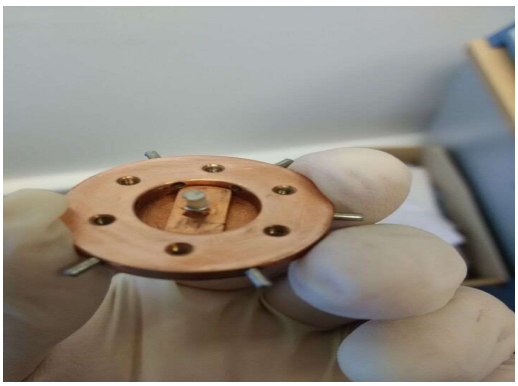

Figure 3.15: Prepared sample with the sample holder.

For the sample transfer from an atmosphere environment to the load-lock chamber, we make use of the specific toll in Fig. 3.16 to hold the sample. The transfers arm in the vacuum chamber work with the same principle and allow for sample transfer processes that are smooth and safe.

Figure 3.16: The sample prepared will be loaded with another kind of sample holder.

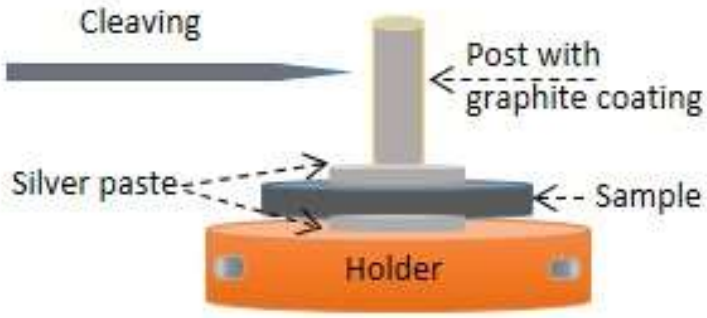

Figure 3.17: Sample prepared for cleaving in the preparation chamber.

Through the Fig. 3.17, we can view the sample prepared for cleaving in the preparation chamber. In order to obtain a fresh surface for the layered materials in UHV, the post is kicked by a wobble stick in the preparation chamber. Since the bonding force of epoxy is stronger than the Van der Waals force between the interlayers of a layered material, the crystal can be cleaved by this mechanical force, and a fresh surface results after cleaving.

References

[1] Christian R. Ast and Hartmut Höchst. Fermi Surface of Bi (111) Measured by Photoemission Spectroscopy. *Phys. Rev. Lett*. **87**, 177602 (2001).

[2] Ding, H., Yokoya, T., Campuzano, J. *et al.* Spectroscopic evidence for a pseudogap in the normal state of underdoped high-T_c superconductors. *Nature* **382**, 51–54 (1996).

[3] Kim, B., Koh, H., Rotenberg, E. *et al.* Distinct spinon and holon dispersions in photoemission spectral functions from one-dimensional $SrCuO_2$. *Nature Phys* **2**, 397–401 (2006).

[4] J. G. Fujimoto, et al., Femtosecond Laser Interaction with Metallic Tungsten and Nonequilibrium Electron and Lattice Temperatures. *Phys. Rev. Lett.* **53**, 1837-1840 (1984).

[5] W. S. Fann, et al., Electron Thermalization in Gold. *Phys. Rev. B.* **46**, 13592-13595, (1992).

[6] H. Petek and S. Ogawa, Femtosecond time-resolved two-photon photoemission studies of electron dynamics in metals. *Progress in Surface Science*. **56**, 239-310 (1997).

[7] W. S. Fann, et al., Direct Measurement of Nonequilibrium Electron-Energy Distributions in Subpicosecond Laser-Heated Gold-Films. *Phys. Rev. Lett.* **68**, 2834-2837 (1992).

[8] T. Fauster, et al., Quasi-elastic scattering of electrons in image-potential states. *Progress in Surface Science*. **82**, 224-243, (2007).

[9] J. D. Koralek, et al., Laser based angle-resolved photoemission, the sudden approximation, and quasiparticle-like spectral peaks in Bi2Sr2CaCu2O8+delta. *Phys. Rev. Lett*. **96**, (2006).

[10] J. D. Koralek, et al., Experimental setup for low-energy laser-based angle resolved photoemission spectroscopy. *Review of Scientific Instruments*. **78**, (2007).

[11] L. Perfetti, P. A. Loukakos, M. Lisowski, U. Bovensiepen, H. Eisaki, and M. Wolf. Ultrafast Electron Relaxation in Superconducting $Bi_2Sr_2CaCu_2O_{8+\delta}$ by Time-Resolved Photoelectron Spectroscopy. *Phys. Rev. Lett*. **99**, 197001 (2007).

[12] L. Rettig, et al., Ultrafast Momentum-Dependent Response of Electrons in Antiferromagnetic $EuFe_2As_2$ Driven by Optical Excitation. *Phys. Rev. Lett*. **108**, 2012.

[13] C. L. Smallwood, et al., Tracking Cooper Pairs in a Cuprate Superconductor by Ultrafast AngleResolved Photoemission. *Science*, **336**, 1137-1139 (2012).

[14] R. Cortes, et al., Momentum-Resolved Ultrafast Electron Dynamics in Superconducting $Bi_2Sr_2CaCu_2O_{8+\delta}$. *Phys. Rev. Lett.* **107**, 2011.

[15] J. Faure, J. Mauchain, E. Papalazarou, W. Yan, J. Pinon, M. Marsi, and L. Perfetti, Full characterization and optimization of a femtosecond ultraviolet laser source for time and angle-resolved photoemission on solid surfaces. *Review of Scientific Instruments*. **83**, 043109 (2012).

[16] W. S. Fann, et al., Direct Measurement of Nonequilibrium Electron-Energy Distributions in Subpicosecond Laser-Heated Gold-Films. *Phys. Rev. Lett*. **68**, 2834-2837 (1992).

[17] J. G. Fujimoto, et al., Femtosecond Laser Interaction with Metallic Tungsten and Nonequilibrium Electron and Lattice Temperatures. *Phys. Rev. Lett*. **53**, 1837-1840 (1984).

[18] S. Hufner, Photoelectron Spectroscopy. Berlin: Springer, 2003.

[19] Chen, Z.; Giorgetti, C.; Sjakste, J.; Cabouat, R.; Veniard, V.; Zhang, Z.; TalebIbrahimi, A.; Papalazarou, E.; Marsi, M.; Shukla, A.; J., P.; Perfetti, L. Ultrafast electron dynamics reveal the high potential of InSe for hot-carrier optoelectronics. *Physical Review B* **97**, 241201 (2018).

[20] Chen, Z.; Dong, J.; Papalazarou, E.; Marsi, M.; Giorgetti, C.; Zhang, Z.; Tian, B.; Rueff, J.-P.; Taleb-Ibrahimi, A.; Perfetti, L. Band Gap Renormalization, Carrier Multiplication, and Stark Broadening in Photoexcited Black Phosphorus. *Nano Lett*. **19**, 488–493 (2018).

[21] F. Schmitt, P. S. Kirchmann, U. Bovensiepen, R. G. Moore, M. K. L. Rettig, J.-H. Chu, N. Ru, L. Perfetti, D. H. Lu, M. Wolf, I. R. Fisher, and Z.-X. Shen. Transient Electronic Structure and Melting of a Charge Density Wave in $TbTe_3$. *Science* **321**, 1649 (2008).

[22] L. Perfetti, et al., Time evolution of the electronic structure of 1T-TaS2 through the insulatormetal transition. *Phys. Rev. Lett*. **97**, 2006.

[23] Först, M., Manzoni, C., Kaiser, S. *et al.* Nonlinear phononics as an ultrafast route to lattice control. *Nature Phys* **7**, 854–856 (2011).

[24] Dienst, A., Hoffmann, M., Fausti, D. *et al.* Bi-directional ultrafast electric-field gating of interlayer charge transport in a cuprate superconductor. *Nature Photon* **5**, 485–488 (2011).

[25] Bossini, D., Dal Conte, S., Hashimoto, Y. *et al.* Macrospin dynamics in antiferromagnets triggered by sub-20 femtosecond injection of nanomagnons. *Nat Commun* **7**, 10645 (2016).

[26] Georg Eder, Stefan Schlögl, Klaus Macknapp, Wolfgang M. Heckl, and Markus Lackinger. A combined ion-sputtering and electron-beam annealing device for the in vacuo postpreparation of scanning probes. *Review of Scientific Instruments* **82**, 033701 (2011).

Chapter 4 Bandgap Renormalization, Carrier Multiplication and Stark Broadening in Photoexcited Black Phosphorous

4.1 Motivation

Two-dimensional (2D) crystals have shown a great deal of potential for applications in design and optimization of electronic and optoelectronic devices [1], mainly due to their high carrier mobility [2,3], broadband photoresponse [4] and intrinsic anisotropy [5-7]. The research on 2D materials has gained remarkable interest since people discovered the graphene and transition metal dichalcogenides (TMDCs). However, the zero-bandgap nature of graphene and the relatively low mobility in TMDCs may limit their applications [5]. Within the family of 2D crystals, black phosphorous (BP) is a promising semiconductor with many desirable properties. Its electronic gap depends on thickness [8,9], attaining the value of 1.5-1.7 eV in the monolayer [10] while shrinking down to 0.3 eV in the bulk limit [11]. As shown in Fig. 4.1, the band gap of black phosphorous strongly depends on its thickness. Both theoretical and experimental work indicate that the energy gap value of the black phosphorous change with the number of layers.

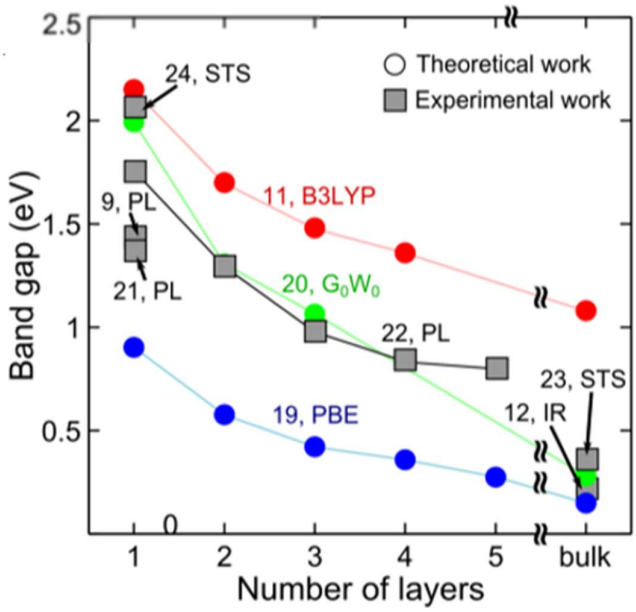

Figure 4.1: Thickness dependence of the black phosphorous band gap, calculated with different approaches [9].

The band structure of black phosphorous is particularly sensitive to external electric fields [12,13] and surface dipoles [14]. Moreover, black phosphorous displays a strong in-plan

anisotropy that could be exploited in optoelectronic and electronic devices. The special properties of black phosphorous are closely related to its structure. Figure 4.2 shows the schematic diagram of the crystal structure of black phosphorous (a), and the calculated band structure of single-, bi- and tri-layer black phosphorous (b). The crystal structure of black phosphorous at ambient conditions is orthorhombic and consists of puckered layers parallel to the x-y plane. Each atom of a single puckered layer is bonded with three neighboring atoms by covalent bonds, whose lengths are nearly equal to each other and the bond angles are close to a right angle. As shown in Fig. 4.2 (b), first principle calculations predict a thickness dependence of the black phosphorous band gap.

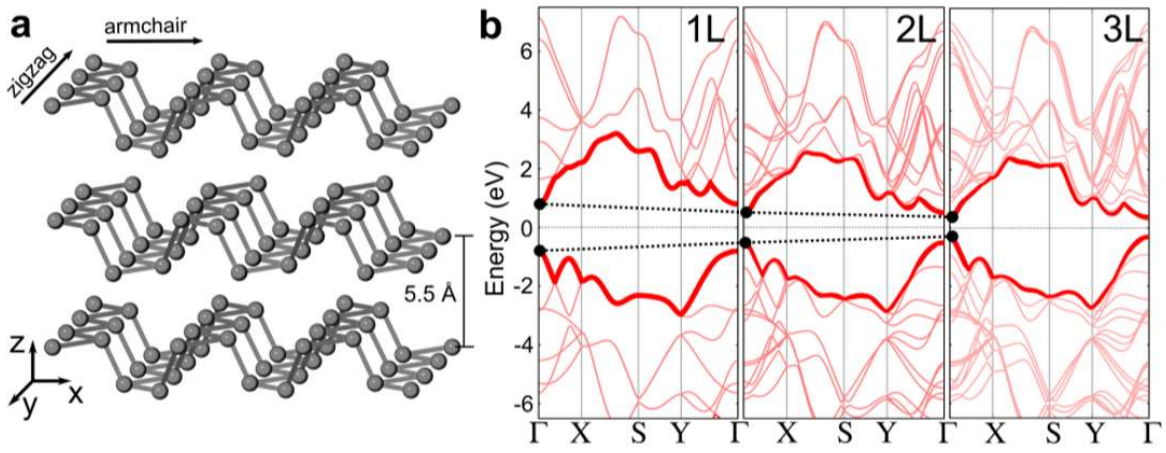

Figure 4.2: (a) Schematic diagram of the crystal structure of black phosphorous. (b) Calculated band structure of single-, bi- and tri-layer black phosphorous [9].

Figure 4. illustrates a schematic energy-level diagram of phosphorous 3p orbital in the case of an atom, a molecule, and a single puckered layer, and black phosphorous crystal [15]. The tight binding model can be instructive to describe the electronic bonding starting from an atomic basis. Indeed, the tight-binding model is an approach to the calculation of electronic band structure using an approximate set of wave functions based upon superposition of wave functions for isolated atoms located at each atomic site. In the case of black phosphorous, the general features of the tight binding scheme can be understood in the following way. In A single layer of black phosphorous the bonds are covalent and essentially made of 3p orbitals. In the two-dimensional band structure of the single layer, therefore, the the valence band consists of the bonding 3p levels and the conduction band of the anti-bonding 3p levels. By suitably choosing the hopping integrals [15], the energy gap between conduction and valence band is located at the center of the Brillouin zone and attains a value of roughly 1.8 eV. The wave functions at the top of the valence band

and the bottom of the conduction band have mainly a p_z-like character. The tight-binding calculations also show that the separation between the bonding and anti-bonding levels related to the bonds bridging the armchair bond-chains running along the x direction, which consist of mainly $3p_x$ and $3p_y$ orbitals, is larger than the one associated with the bonds bridging the zig-zag bond-chains running along the y direction [9]. This means that levels near the gap are mainly related to the bonds bridging the zig-zag bond-chains running along the y direction.

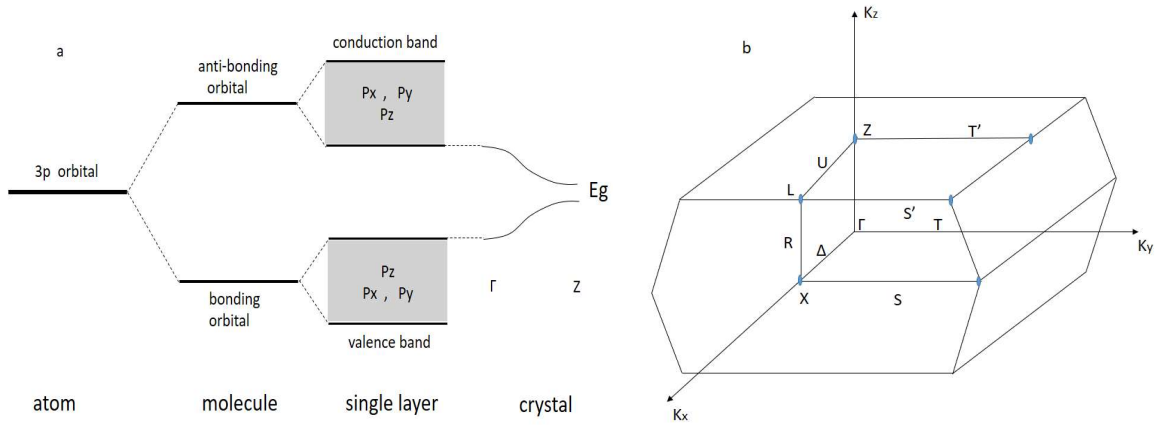

Figure 4.3: (a) Schematic energy-level diagram of phosphorous 3p orbital in atom, molecule, single puckered layer, and black phosphorous crystal. (b) The Brillouin zone of black phosphorous.

In the three-dimensional crystal, black phosphorous has Cmca space group with the lattice parameters of the orthorhombic cell given by a = 4.3763 Å, b = 3.3136 Å and c_{ortho} = 10.478 Å, d_1 = 2.244 Å, d_2 = 2.224 Å, θ_1 = 96.34° and θ_2 = 102.09°. Our collaborator Christine Giorgetti has reproduced the band structure by ab-initio calculations based on density functional theory. The structure has been converted into the monoclinic geometry and further relaxed using Abinit taking into account the Van der Waals interactions with three body corrections as proposed by S. Grimme [16]. The geomentry minimizing the total energy has a = 4.4502 Å, b = 3.3105 Å, c_{ortho} = 10.737Å, d_1 = 2.264 Å, d_2 = 2.226 Å, θ_1 = 96.06° and θ_2 = 102.56°. The employed pseudopotential is P.psp8 provided by Abinit (Perdew-Burke-Ernzerhof GGA exchange-correlation functional [17]). The quasiparticle correction for energies have been calculated using a screened hybrid exchange-correlation functional within HSE06 formalism (Heyd-Scuseria-Ernzerhof (HSE) exchange-correlation functional [18]). Based on this relaxation, the metallic points present along ZΓ and ZA when using PBE functional disappear. Nevertheless, a spurious point with a much smaller band gap appeared very close to Z point along the ZQ direction. The tight-binding calculations [15] indicate that interlayer interactions cause an upward dispersion to the top

of the valence band and a downward one to the bottom of the conduction band along the Γ-Z line. They give rise to the direct minimum gap of about 0.3 eV at the point Z [9], which is consistent with the experimental finding. We conclude that black phosphorous has a single valley for a hole and a single valley for an electron at the point Z. Our calculation of the electronic band structure is illustrated in Fig. 4.4.

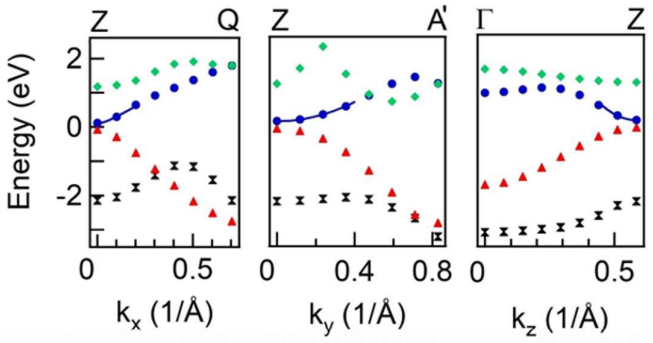

Figure 4.4: Electronic band structure along the Z −A direction (armchair), Z − Q direction (zig-zag) and Γ − Z direction (z axis) of the brillouin zone. The solid line is fit of the conduction band providing effective mass $m_x = 0.1m_e$, $m_y = 1.1m_e$ and $m_z = 0.16m_e$.

4.2 Concurrent work

Black phosphorous has many interesting properties and a long history. It has been first produced by Bridgeman [7, 9] in 1914 under the high pressure of 1.2 GPa and at 200°C. Since then, this material has been studied by many researchers. Undoped black phosphorous samples are always of p-type and show a positive Hall coefficient in the whole temperature range. The carrier density calculated from the Hall coefficient indicates that the occupation of the acceptors gets saturated from a temperature of roughly 220 K. The energy gap determined from the temperature dependence of the conductivity in the intrinsic range is 335meV, while the one determined optically at liquid He temperature is 284.3meV. Samples doped with Te atoms contain an effective donor concentration of $2\text{~}3x10^{16}$ cm^{-3} and show an inversion from p-type to n-type conduction below 220 K, therefore becoming n-type in the low-temperature region [9]. In addition, some works addressed [19-21] the local electronic properties of individual defects and dopants in black phosphorous. Zhizhan Qiu et al. employed low-temperature scanning tunneling microscope (LT-STM) to probe the local electronic structures of single acceptors in BP. They demonstrated that the charge state of individual acceptors could be reversibly switched by controlling the tip-induced band bending. Moreover, acceptor-related resonance features in the tunnelling spectra could be attributed to the formation of Rydberg-like bound hole states. The spatial mapping of the quantum bound states showed

two distinct shapes evolving from an extended ellipse shape for the 1s ground state to a dumbbell shape for the $2p_x$ excited state [19]. The wave functions of bound hole states could be well-described using the hydrogen-like model with anisotropic effective mas. Brian Kiraly et al. made use of a combination of low-temperature scanning tunneling microscopy/spectroscopy (STM/STS) and electronic structure calculations to characterize the structural and electronic properties of single atomic vacancies within several monolayers of the surface of black phosphorous. With experimental analysis and tight-binding calculations, they could depth profile these vacancies and assign them to specific sublattices within the unit cell. Measurements revealed that the single vacancies exhibit strongly anisotropic and highly delocalized charge density, laterally extended up to 20 atomic unit cells. The vacancies have been then studied with STS, revealing in-gap resonance states near the valence band edge and a strong p-doping of the bulk black phosphorous crystal. Quasiparticle interference generated near these vacancies enabled the direct visualization of the anisotropic band structure of black phosphorous [20]. Yuzheng Guo et al. calculated the atomic geometries and transition levels of point defects and substitutional dopants in few layer and bulk black phosphorous. The vacancy was found to reconstruct in the monolayer black phosphorous from a single dangling bond, giving a negative U defect with a +/− transition level at 0.24 eV above the valence band edge. The V^- state formed an unusual 4-fold coordinated site. In few-layer and bulk black phosphorous, the defect became a positive U site. The divacancy was much more stable than the monovacancy but is not yet a deep gap state. Substitutional dopants such as C, Si, O or S did not give rise to shallow donor or acceptor states but instead reconstructed to form non-doping sites. Impurities on black phosphorous adopted the 8-N rule of bonding, as in amorphous semiconductors, rather than simple substitutional geometries seen in tetrahedral semiconductors [21].

Although the equilibrium or steady state of black phosphorous has been extensively characterized, much less is known about the photoexcited state. Referring to other layered semiconductors, the band gap renormalization may be expected at moderate [22] or high excitation fluence [23,24]. Eventually, photoinduced fields at the surface may shape the band structure or lead to a spatial separation between electrons and holes in the topmost layers [25]. Furthermore, the low gap size may lead to a measurable amount of carrier's multiplication [26-28]. The time resolved experiments that have been performed so far [29–32] could not answer these questions. Therefore, it is necessary to find other effective ways to approach these issues. Here, we investigate black phosphorous by means of time and angle resolved photoemission. The non-equilibrium electronic distribution uncovers

the dynamics of photoexicted carriers in reciprocal space. The electrons are excited by the photons centered at 1.57 eV and the electrons relax at the bottom of the conduction band minimum within 1 ps. No sign of bandgap renormalization could be detected in the photoexcited process. To our great astonishment, the photoexcited state is less homogeneous than the equilibrium one. Moreover, a large photoinduced broadening smears the electronic states at early delay time. This effect arises from a spatially varying potential that builds up along the surface upon the sudden change of electronic screening. More insights on the reported phenomenon are obtained by a characterization of the photoelectron signal as a function of the pump fluence.

4.3 Results and Discussion

In the experiments on black phosphorous crystals, the overall energy resolution of the measurements is roughly 30 meV whereas the cross correlation between pump and probe pulse has FWHM of 0.16 ps. All the data have been acquired with *P* polarized probe at an incident angle of 45°. Single crystals of black phosphorous shown in Fig. 4.5 (a) from 'HQgraphene' have been cleaved and measured at the base pressure of 7×10^{-11} mbar in the TrARPES chambers. Moreover, the black phosphorous samples have been oriented by low energy electron diffraction as one can see in the following Fig. 4.5 (b) and our samples are measured at the temperature of 135 K.

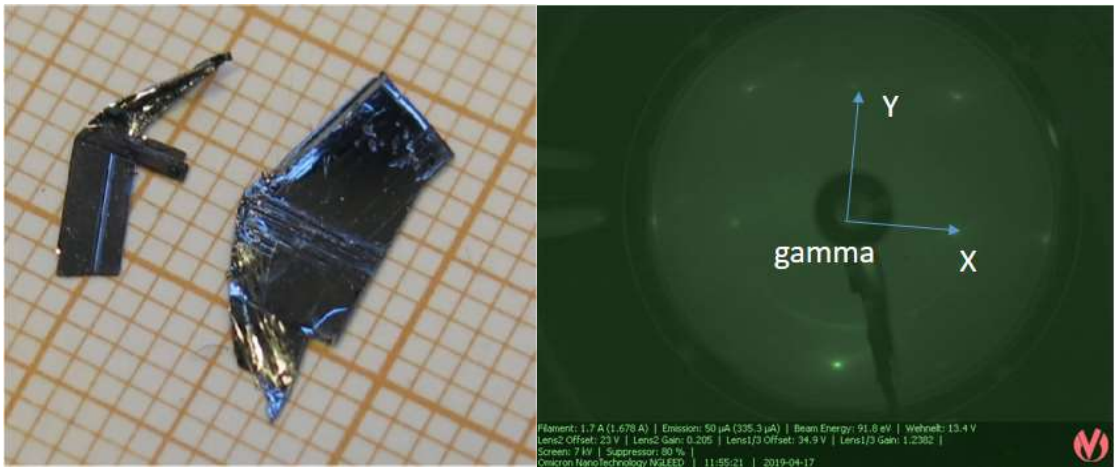

Figure 4.5: (a) picture of black phosphorous sample from 'HQgraphene'. (b) the black phosphorous sample is oriented by low energy electron diffraction.

We performed the X-ray Photoelectron Spectroscopy (XPS) on the black phosphorous sample grown by 'HQgraphene'. The spectra have been acquired on the Galaxy beamline

of Soleil, with photon energy of 3000 eV. The sample has been cleaved in vacuum at the base pressure of 5 × 10^{-7} mbar. Note in Fig. 4.6 the strong emission generated by the phosphorous 2*p* and 2*s* levels. Several shake-off satellites are spaced from the main peak by an energy step of 20 eV. Two additional peaks at -286 eV and -534 eV are due to Carbon and Oxigen contamination, respectively. In contrast to Qiu et al. [19], we do not observe any trace of Sn impurities in our samples.

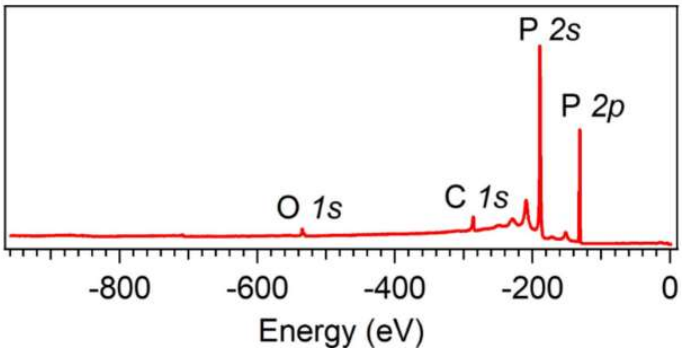

Figure 4.6: X-ray photoelectron spectrum of black phosphorous. Beside the core levels of Phosphorous, we identify Oxygen and Carbon contaminants due to poor vacuum conditions of the XPS chamber.

The time-resolved ARPES experiments performed on the femto-ARPES setup [33], provide new findings on the excited state relaxation in this layered material. Figure 4.7 (a) shows the intensity maps t = 1 ps after the arrival of a pump pulse with incident pump fluence of 230 μJ/cm^2. The wavevector asymmetry and drop of signal at the conduction band minimum are due to matrix elements of the photoemission process. These matrix elements can provide important orbital information on electronic states if specific measurement geometries are implemented. The dispersion along the armchair direction nearly follows the pseudo-relativistic expression $E = \pm[\delta + (m_x^2 v_x^4 + v_x^2 p^2)^{1/2}]$, where m_x is the effective mass and v_x is the band velocity in the linear section. As shown by the dotted lines in Fig. 4.7 (a), the parameters m_x = 0.07±0.02m_e (where m_e is the free electron mass), v_x = 0.61 ± 0.2 × 10^6 m/s and δ = 0.01 eV reproduce both the valence and conduction band with good accuracy. Along the zigzag direction (see Fig. 4.7 (b)), the band structure has the parabolic shape $E = \pm(\Delta/2 + p^2/2m_y)$ with effective mass $m_y = m_y^c$= 1.1±0.1m_e for electrons and $m_y = m_y^v$= 0.6 ± 0.05m_e for holes. Within the experimental uncertainties, the derived values are consistent with Shubnikov-de Haas oscillations in high magnetic field [9, 34] and ab-initio calculations. Table 4.1 compares the observed effective masses with the calculated ones. The theoretical values obtained by the self-consistent pseudopotential method (SCPM) are in better agreement with the observed

ones than those of the tight binding method. The average effective mass, defined by $(m_x m_y m_z)^{1/3}$, is 0.22 m_e for the electrons and 0.24 m_e for the holes.

Table 4.1 Effective masses of carriers in black phosphorous

Direction	Hole		Electron	
	Expt.	***Cal.***	***Expt.***	***Cal.***
m_x/m_e	0.076	0.09	0.0826	0.09
M_y/m_e	0.648	0.81	1.027	1.16
M_z/m_e	**0.280**	**0.36**	**0.128**	**0.17**

The extracted $\Delta = 2(m_x v_x^2 + \delta) = 0.31 \pm 0.02$ eV is in agreement with the value reported by infrared spectroscopy [5] and scanning tunneling microscopy [20]. We repeated the measurements of Fig. 4.7 (a) after reducing the pump fluence by a factor six. Figure 4.7 (c) shows that the eventual difference of bandgap is smaller than the experimental uncertainties. This means that photoexcitation does not renormalize the bandgap. The negligible bandgap renormalization is ascribed to the moderate photoexcitation density and to the 3D screening of the Coulomb interaction.

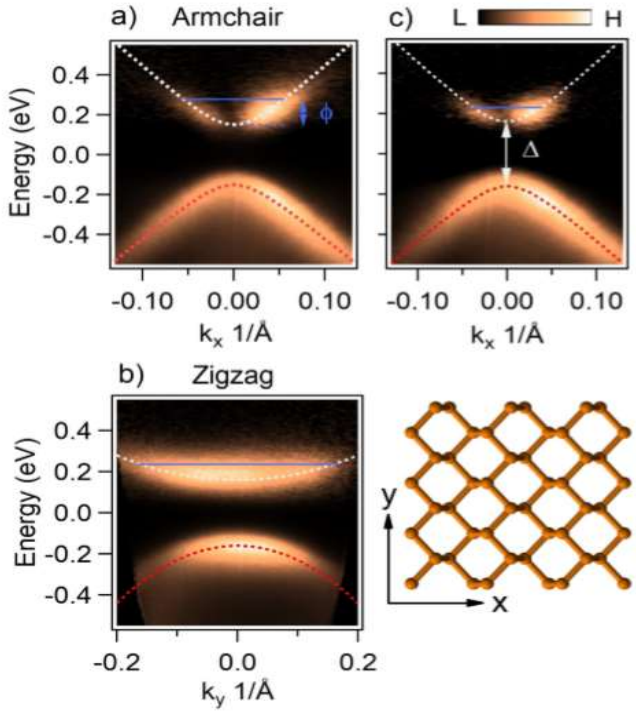

Figure 4.7: Photoelectron Intensity map acquired at pump probe delay time t = 1 ps and in the following conditions: (a) along the armchair direction with pump fluence of 230 μJ/cm^2, (b) along the zigzag direction with pump fluence of 230 μJ/cm^2, (c) along the armchair direction with pump fluence of 35 μJ/cm^2. The zero of the energy axis has been defined as the center of the band gap Δ (the actual chemical potential being 80 meV above the

valence band maximum). We multiplied the signal at positive energy by a factor between 50-300 in order to visualize conduction and valence band on the same colorscale. White and red dotted line stand for the modeled dispersion of electronic states. The blue solid line is the expected filling of the conduction band under the assumption of negligible carrier multiplication. Photoexcitation density of 6,3,1 × 10^{19} corresponds to φ = 130,80,40 meV in panel (a), (b), (c), respectively.

There are many experimental and theoretical work on the bandgap renormalization of black phosphorous that have been published in recent years. Here we will survey some these work, giving particular attention to those which are most relevant. We first stress that the dimensionality of the electronic bands is an essential aspect of the problem.

It is established that a large redistribution of spectral weight takes place in the 2D chalcogenides [22]. Upon photoexcitation of such monolayer semiconductors, the correlated electron hole plasma generated by the dissociation of strongly bound excitons deeply reshapes the optical properties. This renormalization process of the optical gap in 2D materials if sketched in Fig. 4.8 (a). However, the efficient screening of 3D black phosphorus restrains the binding of excitons below 20 meV [9]. Consistently with our experimental finding, these weakly bounds electron-hole pairs cannot have large impact on the size of the bandgap.

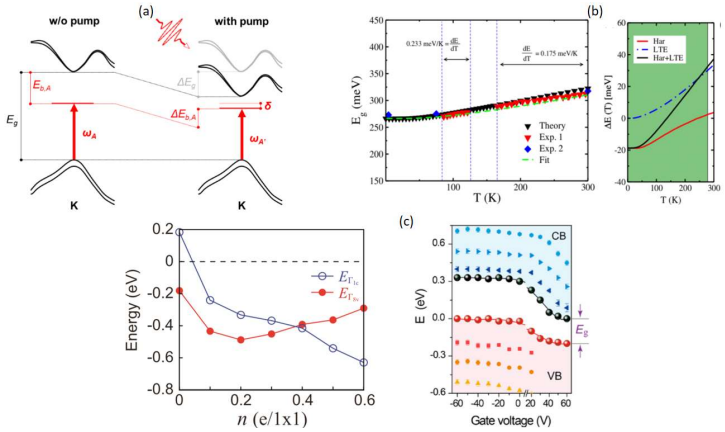

Figure 4.8: Bandgap renormalization of materials in the following conditions: (a) Electronic band structure (black line) of monolayer MoS_2 at the K point and the exciton energy (red line) in absence (left) and in presence (right) of pump pulse absorption. The overall shift of the excitonic absorption resonances (δ) results from both the shrinkage of the electronic bandgap and the renormalization of the exciton binding energy, due to the presence of photoexcited carriers, i.e., $\delta = \Delta E_g - \Delta E_b$ [35]. (b) Theoretical and experimental BP band-gap as a function of temperature. In the left frame different phononic contribution to the bandgap increase are shown [15]. (c) Calculated conduction band minimum and valence band maximum relative to chemical potential as a function of the doping level (left) [14] and Gate-controlled Stark effect in an 11-layer BP flake device: VBM (red balls), CBM (black balls) and bandgap (E_g) of 11-layer BP at different gate voltages (right) [12].

Secondly, we consider the role that hot phonons may have on the band structure. At the moderate excitation fluence of 230 μJ/cm^2 the pump pulse injects roughly 2 meV for each atom of phosphorous. Under these conditions, the effective temperature of the transverse optical branch cannot increase more than 30 K. According to the data from the ref 35, (also shown in Fig 4.8 b)) the adiabatic electron-phonon coupling and anharmonic interactions may lead to a gap increase of few meV. Such small effect is also compatible with the uncertainties in our measurement. Last but not least, our result points out that photoexcitation and surface doping have little in common. By doping the surface layer of black phosphorous with alkaline atoms, the local electronic screening lowers the binding energy of the conduction band down to an inversion point [14]. The bandgap shrinks by 25% when the electrons fill the conduction band up to 150 meV [14] (see also Fig. 4.8 c)). However, the surface dipole that induces the local band inversion upon alkaline atoms adsorption [14] or electrostatic gating [12,13] has no analogous in an optical absorption.

The photoexcitation density is an important parameter to understand the relaxation mechanism of excited carriers in black phosphorous. The reflection coefficient of a pump pulse with p polarization and incidence angle of 45° is

$$R \cong \left(\frac{1-n/\sqrt{2}}{1+n/\sqrt{2}}\right)^2,$$

where n = 3 is the refractive index of black phosphorous at wavelength of 800 nm [6]. The initial photoexcitation density ρ is obtained from the incident fluence F via the formula

$$\rho = \frac{F(1-R)}{h\nu\lambda},$$

where $h\nu$ is the photon energy and λ is the optical penetration depth. We notice that λ = 140 nm and λ = 280 nm along the armchair and zig-zag direction, respectively [7]. After the thermalization time t = 1 ps, the electronic density at the surface of the sample is

$$\rho' = \rho exp\frac{Dt}{\lambda^2}\left(1 - \mathrm{erf}\frac{\sqrt{Dt}}{\lambda}\right),$$

where the diffusion constant D = 50 cm^2/s is obtained from the mobility μ of conduction electrons along the z axis [9] and assuming the Einstein relation $D = \mu k_b T/e$.

Figure 4.9 (a) shows the pseudo-relativistic expression of the conduction band along the armchair direction and a parabolic approximation with effective mass $m_x = 0.07m_e$. The two dispersions are very similar up to a filling level of 150 meV (blue line in the figure). As a consequence, we evaluate the filling factor by the parabolic dispersion approximation:

$$\varphi = \frac{\hbar^2}{2m}(3\pi^2\rho')^{2/3},$$

where $m = (m_x m_y m_z)^{1/3}$, with $m_x = 0.07m_e$, $m_y = 1.1m_e$ and $m_z = 0.15m_e$. As shown by the table in 4.9 (b), the good agreement between time resolved ARPES data, the cyclotron resonance experiments [9] and DFT calculations provide confidence on the estimated mass value. The derived filling factor is: φ = 150 meV for a pump pulse of 230 μJ/cm^2

polarized along the armchair direction; φ = 110 meV for a pump pulse of 230 μJ/cm^2 polarized along the zig-zag direction; and φ = 45 meV for a pump pulse of 40 μJ/cm^2 polarized along the armchair direction.

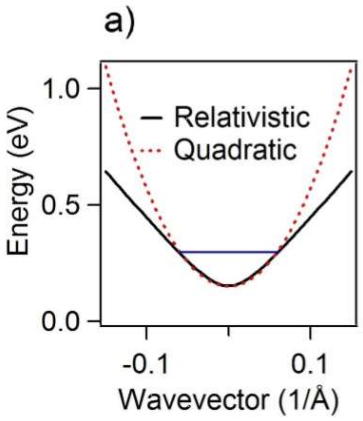

b)

Effective mass	m_x	m_y	m_z
ARPES	0.07	1.1	—
Cyclotron	0.08	1.1	0.13
DFT	0.1	1.1	0.16

Figure 4.9: (a) (solid black curve) Pseudo-relativistic dispersion fitting the experimental data and (red dotted curve) parabolic dispersion with effective mass m_x = 0.07m_e. The solid blue curve marks the filling factor φ = 150 meV. (b) Effective mass of the conduction band along the x, y, z direction. The first line reports the values extracted from time resolved ARPES data. The second line reports the values extracted from cyclotron resonance experiments [9]. The third line reports the value obtained by Density Functional Theory (DFT) calculation.

Several scattering mechanisms contribute to the thermalized state in Fig. 4.7. The excited electrons dissipate energy via phonon emission, generate new electron-hole pairs by impact ionization and interact with each other via Auger scattering. The related processes are described in Fig. 4.10. Only the first mechanism conserves the carrier density, whereas the second leads to carrier multiplication. A simple analysis establishes if the number of conducting charges is preserved. The pulse centered at 1.57 eV and polarized along the armchair direction has optical penetration depth [7] of 140 nm. By taking into account reflection losses, an incident fluence of 230 μJ/cm^2 corresponds to photoexcitation density ρ of 6×10^{19}/cm^3. Under the hypothesis that thermalization does not change this density, the electron gas at 1 ps would display a filling level φ = 130 meV. An equivalent analysis holds in the zigzag direction instead of the armchair one. However, the penetration depth of light polarized along the y axis [5-7] is twice longer because the polarization of the pump was always pointing along the slit of the analyzer. As a consequence, the intensity map acquired along the zigzag direction should display φ = 80 meV. The blue lines in Fig. 4.7 show that estimated and measured filling of the conduction band are in good agreement. This finding implies that electrons excited by 1.57 eV photons roughly conserve the initial density during the thermalization process. Either the

electron-phonon is the dominant scattering process or impact ionization is well balanced by Auger scattering [26]. Therefore, we deduce that black phosphorous behaves differently than graphene, where carrier multiplication has instead been reported [24, 27, 28]. Notice moreover that the intensity map in Fig. 4.7 (c), obtained with $\rho = 1 \times 10^{19}$ cm^{-3}, suggests that the measured filling overcomes the estimated φ = 45 meV. Although the data of Fig. 4.7 (c) could be compatible with a multiplication factor appreciably larger than one, the false impression of a larger filling may also arise from φ becoming comparable to our energy resolution.

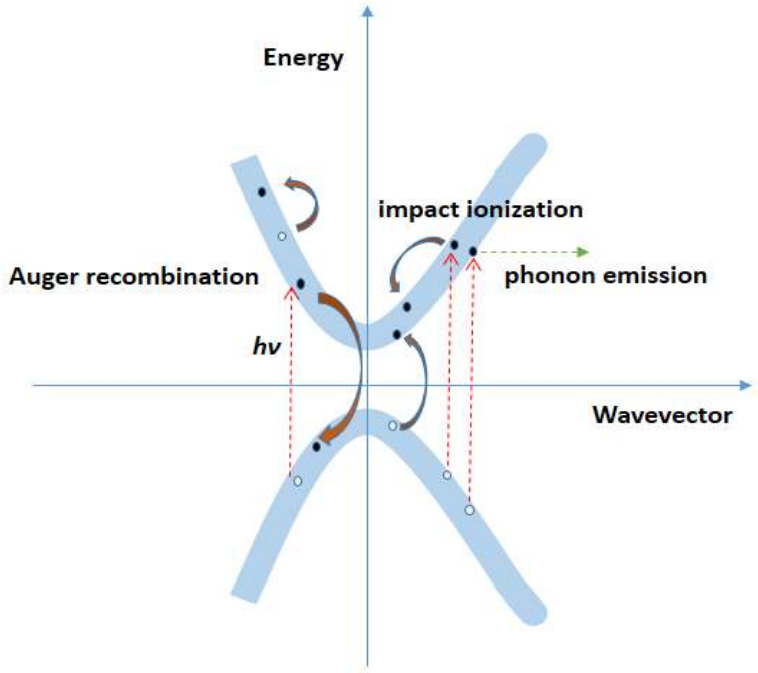

Figure 4.10: The excited electrons redistribute and dissipate energy via different mechanisms.

The full temporal evolution of the transient signal is shown in Fig. 4.11 (a), where we plot the differential intensity maps acquired for increasing pump probe delay. The signal at positive energy has been multiplied by a factor 30 to equalize the contrast of valence and conduction band. At early delay time, the electronic occupation of the conduction band still lingers below our detection limit. The carrier concentration at the bands edges gradually builds up, reaching its maximum at t = 1 ps. We show in Fig. 4.11 (b), (c) the temporal evolution of the differential signal integrated in a small area at the edge of the conduction band or valence band. In order to isolate the evolution of photoexcited hole density, the extra contribution of Stark broadening has been subtracted from the integrated signal. Fig. 4.11 (b) confirms that the holes also require 1 ps to thermalize. On the long timescale,

diffusion, drift and recombination rule the dynamics of excited carriers. A detailed modeling of such inter-twinned mechanisms is out of the scope of the present article. Nonetheless, we note that a phenomenological expression $(1 + t/\tau)^{-1}$ fits well the experimental data of Fig. 4.11 (b), (c) if $\tau = \tau_h = 10$ ps for holes and $\tau = \tau_e = 2.5$ ps for electrons. Since black phosphorous is naturally p doped, the electrons in the conduction band are captured by acceptor states. Therefore, the lifetime of minority carriers is shorter than the one of the majority one [36]. We also recall that built-in fields may restrain the diffusion of holes in the bulk of the sample [30].

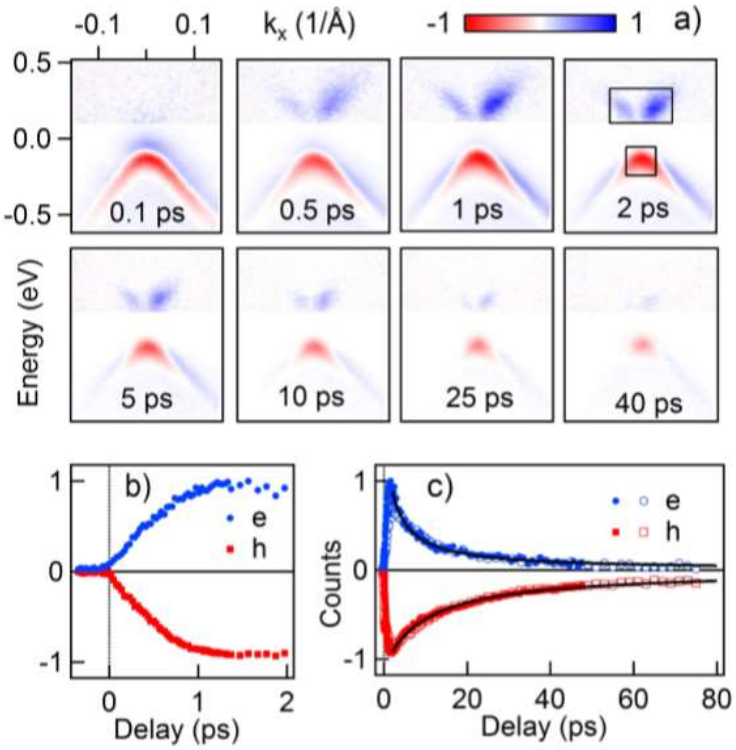

Figure 4.11 (a) Differential intensity map acquired along the armchair direction with pump fluence of 230μJ/cm^2 at increasing pump probe delays. The photoelectron intensity at positive energy has been multiplied by a factor 30. Rectangles in the upper right panel indicate the area in the conduction and valence band where the differential signal has been integrated. Temporal evolution of pump induced signal at the bottom of the conduction band (blue circles) and top of the valence band (red squares) for (b) early and (c) longer delay times. The contribution of photoinduced broadening has been removed from the integrated signal in the valence band. Filled and open symbols stand for measurements performed on two different cleaves. Solid lines are fits of the experimental data with the test function $(1 + t/\tau)^{-1}$.

Fig. 4.12 (a) shows the differential intensity map acquired along the armchair direction at delay time of 2 ps. The differential signal integrated in the black rectangle of Fig. 4.12 (a) is shown as a function of pump probe delay in Fig. 4.12 (c) (dotted red curve). Such signal arises from the superposition of two distinct effects: the depletion of the valence band due

to the photoexcited hole density, and a reduction of spectral intensity due to Stark broadening. We show in Fig. 4.12 (b) the Momentum Distribution Curves (MDCs) acquired just before and 0.1 ps after the arrival of the pump pulse. Note the sudden increase of MDCs Full Width Half Maximum upon photoexcitation. In Fig. 4.12 (c), the rescaled FWHM variation (dotted dark curve) is the Stark broadening component that we subtract from the integrated signal (dotted red curve). The result of this correction (solid red curve) provides the temporal evolution of the photoexcited hole density in the valence band.

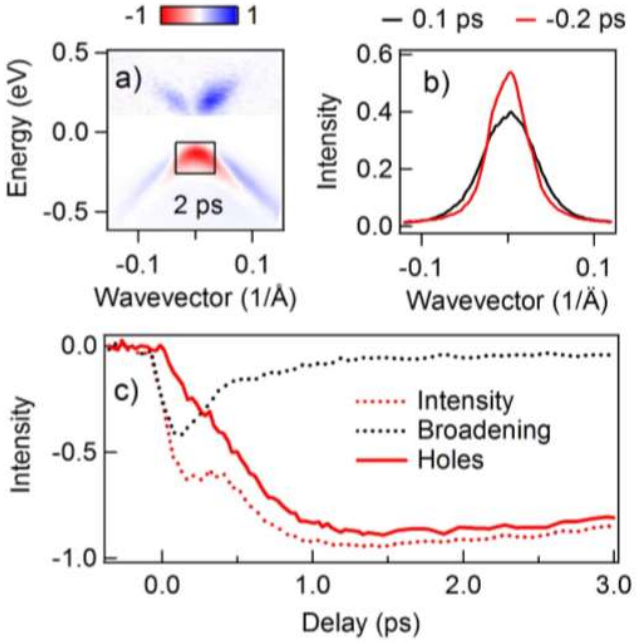

Figure 4.12: (a) Differential intensity map acquired 2 ps after photoexcitation. The black rectangle defines the area where the valence band signal has been integrated. (b) Normalized Momentum Distribution Curves (MDCs) extrated at -0.1 eV, (red curve) before and (black curve) 100 fs after the arrival of the pump beam. (c) Temporal evolution of (red dotted curve) the integrated signal, (black dotted curve) the rescaled FWHM variation of the MDCs and (red solid curve) the difference between these two curves.

Next, we discuss the result that photoexcitation has a large impact on the spectral distribution of valence band. Fig. 4.13 (a) and (b) compare the photoelectron intensity maps acquired at t = −0.5 ps and 0.1 ps along the armchair direction. Note the blurry look of the valence band at positive delay. The difference intensity map reported in Fig. 4.13 (c) is consistent with a large spectral broadening joint to a mean shift towards higher energy. Fig. 4.13 (d-f) show the analogous analysis along the zigzag direction. We ascribe the Stark broadening to the emergence of an inhomogeneous potential along the surface plane.

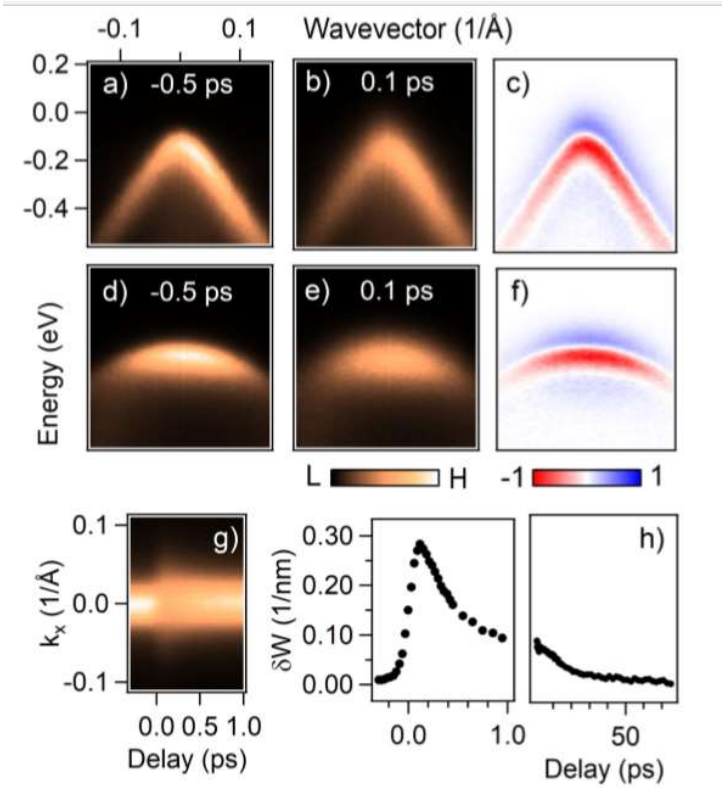

Figure 4.13: Photoelectron intensity map acquired along the armchair direction (a) at t = −0.5 ps and (b) at t = 0.1 ps. (c) Difference between the armchair maps at positive and negative delay. Photoelectron intensity map acquired along the zigzag direction (d) at t = −0.5 ps and (e) at t = 0.1 ps. (f) Difference between the zigzag maps at positive and negative delay. (g) Intensity map of Momentum Distribution Curves (MDCs) extracted at -0.1 eV as a function of pump probe delay. (h) Photoinduced variation of MDCs FWHM as a function of pump probe delay. All the data in this image have been acquired with pump fluence of 230 μJ/cm^2.

In black phosphorous, the natural source of inhomogeneity is the formation of defects during the crystal growth. Scanning Tunneling Microscopy (STM) experiments on 'HQgraphene' samples have imaged single vacancies and Sn impurities [19,20] with atomic resolution. The acceptors in the near surface region are negatively charged, therefore generating local fields [19]. Electrons bounded to these sites have a localization length d which is roughly 5 nm along the armchair direction and is roughly 2 nm along the zigzag one. According to STM data [19], the density of the acceptors N is roughly 10^{18}/cm^3 verifies $0.1 < dN^{1/3} < 1$. In this regime, impurities can be viewed as a diluted quantum system forming a narrow band [37]. Although the electronic occupation may change from site to site, charge fluctuations with long wavelength are small enough to guaranty a good pinning of the chemical potential [37]. As a consequence, each plane parallel to the surface is nearly isopotential. Upon photoexcitation, the average excess energy of the excited carriers rises abruptly to 0.3-0.6 eV. In analogy to interference patterns generated

by quasiparticles [20], the injected carriers scatter strongly with localized states. Electrons around defects are ionized or strongly perturbed, so that an inhomogeneous screening of the local potential give rise to electric fields parallel to the surface plane. Finally, we cannot exclude that a Stark renormalization of the local band-gap takes place before that electrons and holes have thermalized. This interesting issue calls for transient absorption experiments in the mid-infrared region.

Figure 4.13 (g) shows an intensity map of Momentum Distribution Curves (MDCs) extracted at energy of -0.1 eV and variable pump probe delay. The variation of the MDCs Full Width Half Maximum (FWHM) is plotted in Fig. 4.13 (h). As expected from a purely electronic process, the rise of the inhomogeneous broadening takes place within the duration of the pump pulse and recovers during the thermalization time of ≅1 ps. As displayed by Fig. 4.13 (h), the remnant effect at longer delay decays with time constant of 20 ps. Based on these results, we identify three different intervals: i) In equilibrium conditions, the chemical potential is pinned in the impurity band via screened interactions. ii) Just after photoexcitation, the large excess energy of the electrons and holes give rise to a redistribution of the charge density and inhomogeneous fields. iii) At longer delay, the thermalized and hot plasma is again capable of pinning the chemical potential, although deviations from equilibrium case can still be measured.

Fig. 4.14 shows energy distribution curves extracted (solid red curve) 0.2 ps before and (solid dark curve) 0.1 ps after the arrival of the pump pulse. The incoherent background contributing to these spectra (dotted red curve) is estimated by a Shirley method. In order to evaluate the Stark shift and Stark broadening, we subtract the background to the EDCs. The resulting intensity distribution $I(\epsilon)$ has mean energy

$$\langle\epsilon\rangle = \frac{\int \epsilon I(\epsilon) d\epsilon}{\int I(\epsilon) d\epsilon},$$

and mean standard deviation,

$$\Delta\epsilon = \left\{\frac{\int \epsilon I(\epsilon) d\epsilon}{\int I(\epsilon) d\epsilon} - \langle\epsilon\rangle^2\right\}^{1/2},$$

Upon photoexitation, $\langle\epsilon\rangle$ increases by ≅ 8 meV whereas $\Delta\epsilon$ increases by ≅ 30 meV. The Stark shift coincides with the variation of $\langle\epsilon\rangle$ whereas the Stark broadening is given by $\Delta\epsilon$ times $2(2\ln 2)^{1/2}$. In other words, the FWHM of the EDCs increases by ≅ 80 meV just after photoexcitation.

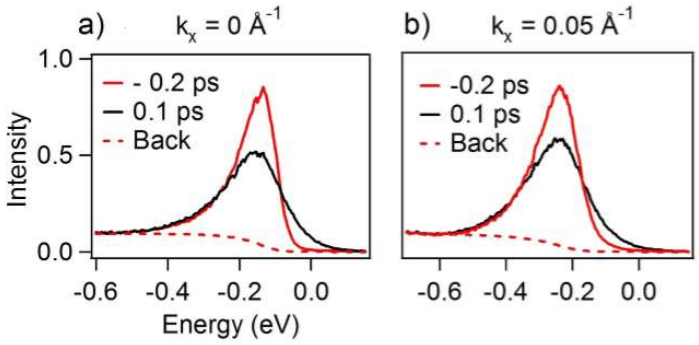

Figure 4.14: (a) Energy distribution curves (EDCs) extracted at k_x = 0 /Å (solid red curve) 0.2 ps before and (solid black curve) 0.1 ps after the arrival of the pump pulse. (b) Energy distribution curves extracted at k_x = 0.05 /Å (solid red curve) 0.2 ps before and (solid black curve) 0.1 ps after the arrival of the pump pulse. In both panels, the dashed red curve stands for the incoherent background contributing to the EDCs.

The dependence of Stark broadening on the photoexcitation density is obtained via the acquisition of differential intensity maps for different pumping fluence. The scaling of the signal in Fig. 4.15 (a) strongly deviates from a linear progression. Fig. 4.15 (b) shows that the MDCs FWHM increases with photoexcitation density as the phenomenological expression $\alpha \cdot \ln(1+\rho/\rho_0)$. The parameter, $\rho_0 = 5\times10^{17}$ cm^{-3} is comparable to the nominal acceptor density of our sample, while α = 0.061/nm constrains the energy spread of inhomogeneous fields to one third of the gap size. Such findings pave the way for the development of a microscopic model that will be able to merge: diluted quantum systems, intrinsic disorder and an ultrafast quench.

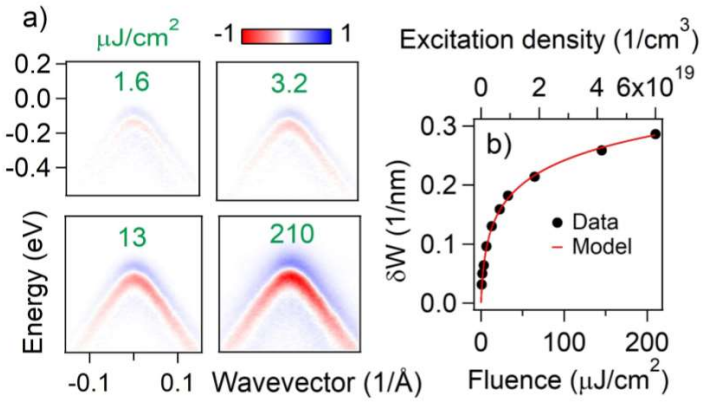

Figure 4.15: (a) Differential intensity maps along the armchair direction, acquired at t = 0.1 ps and different values of the pump fluence. b) The FWHM variation of MDCs extracted at −0.1 eV and t = 0.1 ps (circles). Experimental data (black marks) have been fit by the test function $\alpha\ln(1+\rho/\rho_0)$ (solid red line).

Finally, we measured the influence on the Stark broadening for different temperature conditions. Fig. 4.16 shows the difference between a map acquired at 100 fs and -200 fs for indicative temperatures between 140 K and 300 K. Since the colorscale is identical in all plots, the magnitude of Stark broadening is independent of temperature.

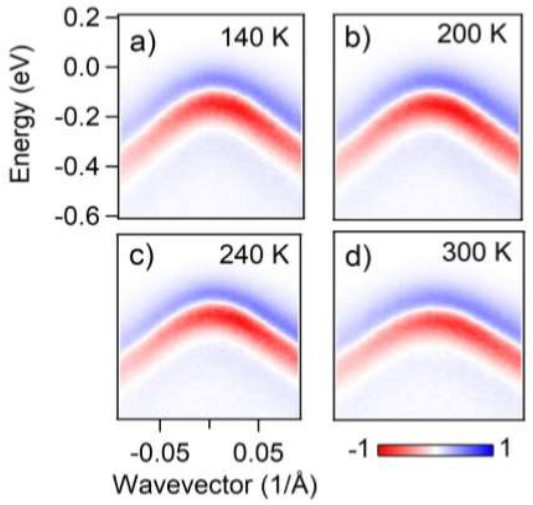

Figure 4.16: (a-d) Differential intensity map along the armchair direction acquired at various sample temperature.

4.4 Conclusions

In this chapter, we surveyed the carriers dynamics and electronic structure evolution in photoexcited black phosphorous using time- and angle- resolved photoelectron spectroscopy. In spite of a narrow band gap, the carrier multiplication is not found in our measurements due to the high dominant role of phonon emission in the thermalization process. Since the bulk black phosphorous does not have excitons with high binding energy, the bandgap renormalization is negligible after photoexcitation. Furthermore, a Stark broadening occurs in the valence band of BP at the early stage of pump photons injection. This interesting result is ascribed to the presence of inhomogeneous near surface field from the impurity band. We argue that carriers with high excess energy ionize charged defects and induce the inhomogeneous screening of a local potential. As a consequence, the pinning of the valence band is perturbed by development of fields parallel to the surface plane.

References

[1] Yin, J., Tan, Z., Hong, H. et al. Ultrafast and highly sensitive infrared photodetectors based on two-dimensional oxyselenide crystals. *Nat Commun* **9**, 3311 (2018).

[2] Li, L.; Yu, Y.; Ye, G. J.; Ge, Q.; Ou, X.; Wu, H.; Feng, D.; Hui, C. X.; Zhang, Y. Black phosphorus field-effect transistors. *Nature Nanotech* **9**, 372 (2014).

[3] Koenig, S. P.; Doganov, R. A.; Schmidt, H.; Castro Neto, A. H.; Özyilmaz, B. Electric field effect in ultrathin black phosphorus. *Appl. Phys. Lett* **104**, 103106 (2014).

[4] Buscema, M.; Groenendijk, D. J.; Blanter, S. I.; Steele, G. A.; van der Zant, H. S. J.; Castellanos-Gomez, A. Fast and Broadband Photoresponse of Few-Layer Black Phosphorus Field-Effect Transistors. *Nano Lett* **14**, 3347 (2014).

[5] Xia, F.; Wang, H.; Jia, Y. Rediscovering black phosphorus as an anisotropic layered material for optoelectronics and electronics. *Nature Comm* **5**, 4458 (2014).

[6] Yuan, H. et al. Polarization-sensitive broadband photodetector using a black phosphorus vertical p-n junction. *Nature Nanotech* **10**, 707 (2015).

[7] Ling, X. et al. Anisotropic Electron-Photon and Electron-Phonon Interactions in Black Phosphorus. *Nano Lett* **16**, 2260 (2016).

[8] Tran, V.; Soklaski, R.; Liang, Y.; Yang, L. Layer-controlled band gap and anisotropic excitons in few-layer black phosphorus. *Phys. Rev. B* **89**, 235319 (2014).

[9] Morita, A. Semiconducting black phosphorus. *Appl. Phys. A* **39**, 227 (1986).

[10] Liu, H.; Neal, A. T.; Zhu, Z.; Luo, Z.; Xu, X.; Tomnek, D.; Ye, P. D. Phosphorene: An Unexplored 2D Semiconductor with a High Hole Mobility. *ACS Nano* **8**, 4033 (2014).

[11] Hanlon, D., Backes, C., Doherty, E. et al. Liquid exfoliation of solvent-stabilized few-layer black phosphorus for applications beyond electronics. *Nat Commun* **6**, 8563 (2015).

[12] Liu, Y.; Qiu, Z.; Carvalho, A.; Bao, Y.; Xu, H.; Tan, S. J. R.; Liu, W.; Castro Neto, A. H.; Loh, K. P.; Lu, J. Gate-Tunable Giant Stark Effect in Few-Layer Black Phosphorus. *Nano Lett* **17**, 1970 (2017).

[13] Deng, B.; Tran, V.; Xie, Y.; Jiang, H.; Li, C.; Guo, Q.; Wang, X.; Tian, H.; Koester, S. J.; Wang, H.; Cha, J. J.; Xia, Q.; Yang, L.; Xia, F. Efficient electrical control of thin-film black phosphorus bandgap. *Nature Commun* **8**, 14474 (2017).

[14] Kim, J.; Baik, S. S.; Ryu, S. H.; Sohn, Y.; Park, S.; Park, B.-G.; Denlinger, J.; Yi, Y.; Choi, H. J.; Kim, K. S. Observation of tunable band gap and anisotropic Dirac semimetal state in black phosphorus. *Science* **723**, 349 (2015).

[15] Wu, J., Su, W. & Gumbs, G. Anomalous magneto-transport properties of bilayer phosphorene. *Sci Rep* **10**, 7674 (2020).

[16] Grimme, S.; Antony, J.; Ehrlich, S.; Krieg, H. A consistent and accurate ab initio parametrization of density functional dispersion correction (DFT-D) for the 94 elements H-Pu. *J. Chem. Phys* **132**, 154104 (2010).

[17] Perdew, J. P.; Burke, K.; Ernzerhof, M. Generalized Gradient Approximation Made Simple. *Phys. Rev. Lett* 77, 3865 (1996).

[18] Heyd, J.; Scuseria, G. E.; Ernzerhof, M. Hybrid functionals based on a screened Coulomb potential. *J. Chem. Phys* **118**, 8207 (2003).

[19] Qiu, Z.; Fang, H.; Carvalho, A.; Rodin, A. S.; Liu, Y.; Tan, S. J. R.; Telychko, M.; Lv, P.; Su, J.; Wang, Y.; Castro Neto, A. H.; Lu, J. Resolving the Spatial Structures of Bound Hole States in Black Phosphorus. *Nano Lett* 17, 6935 (2017).

[20] Kiraly, B.; Hauptmann, N.; Rudenko, A. N.; Katsnelson, M. I.; Khajetoorians, A. A. Probing Single Vacancies in Black Phosphorus at the Atomic Level. *Nano Lett* **17**, 3607 (2017).

[21] Guo, Y., Robertson, J. Vacancy and Doping States in Monolayer and bulk Black Phosphorus. *Sci Rep* **5**, 14165 (2015).

[22] Pogna, E. A. A.; Marsili, M.; De Fazio, D.; Dal Conte, S.; Manzoni, C.; Sangalli, D.; Yoon, D.; Lombardo, A.; Ferrari, A. C.; Marini, A.; Cerullo, G.; Prezzi, D. PhotoInduced Bandgap Renormalization Governs the Ultrafast Response of Single-Layer MoS_2. *ACS Nano* **10**, 1188 (2016).

[23] Soren Ulstrup, Antonija Grubisic Cabo, Jill A. Miwa, Jonathon M. Riley, Signe S. Gronborg, Jens C. Johannsen, Cephise Cacho, Oliver Alexander, Richard T. Chapman, Emma Springate, Marco Bianchi, Maciej Dendzik, Jeppe V. Lauritsen, Phil D. C. King, and Philip Hofmann. Ultrafast Band Structure Control of a Two-Dimensional Heterostructure. *ACS Nano* **10**, 6, 6315–6322 (2016).

[24] Jiang Pu, Keichiro Matsuki, Leiqiang Chu, Yu Kobayashi, Shogo Sasaki, Yasumitsu Miyata, Goki Eda, Taishi Takenobu. Exciton Polarization and Renormalization Effect for Optical Modulation in Monolayer Semiconductors. *ACS Nano* **13** (8), 9218-9226 (2019).

[25] Shaofeng Ge, Chaokai Li, Zhiming Zhang, Chenglong Zhang, Yudao Zhang, Jun Qiu, Qinsheng Wang, Junku Liu, Shuang Jia, Ji Feng, and Dong Sun. Dynamical Evolution of Anisotropic Response in Black Phosphorus under Ultrafast Photoexcitation. *Nano Lett*. **15**, 4650 (2015).

[26] Winzer, T.; A., K.; Malic, E. Carrier multiplication in graphene. *Nano Lett* **10**, 4839 (2010).

[27] Plotzing, T.; Winzer, T.; Malic, E.; Neumaier, D.; Knorr, A.; Kurz, H. Experimental Verification of Carrier Multiplication in Graphene. *Nano Lett* **14**, 5371 (2014).

[28] Johannsen, J. C. et al. Tunable carrier multiplication and cooling in graphene. *Nano Lett* **15**, 326 (2014).

[29] Chen, Z.; Giorgetti, C.; Sjakste, J.; Cabouat, R.; Veniard, V.; Zhang, Z.; TalebIbrahimi, A.; Papalazarou, E.; Marsi, M.; Shukla, A.; J., P.; Perfetti, L. Ultrafast electron dynamics reveal the high potential of InSe for hot-carrier optoelectronics. *Physical Review B* **97**, 241201 (2018).

[30] Papalazarou, E.; Khalil, L.; Caputo, M.; Perfetti, L.; Nilforoushan, N.; Deng, H.; Chen, Z.; Zhao, S.; Taleb-Ibrahimi, A.; Konczykowski, M.; Hruban, A.; Wolos, A.; Materna, A.; Krusin-Elbaum, L.; M., M. Unraveling the Dirac fermion dynamics of the bulk-insulating topological system Bi_2Te_2Se. *Phys. Rev. Materials* **2**, 104202 (2018).

[31] Chen, Z.; Lee, M.-i.; Zhang, Z.; Diab, H.; Garrot, D.; Lédée, F.; Fertey, P.; Papalazarou, E.; Marsi, M.; Ponseca, C.; Deleporte, E.; Tejeda, A.; Perfetti, L. Time-resolved photoemission spectroscopy of electronic cooling and localization in $CH_3NH_3PbI_3$ crystals. *Phys. Rev. Materials* 1, 045402 (2017).

[32] Jiaqi He, Dawei He, Yongsheng Wang, and Hui Zhao. Photocarrier Dynamics in Transition Metal Dichalcogenide Alloy $Mo_{0.5}W_{0.5}S_2$. *Optics Express* **23**, 33370-33377 (2015).

[33] Faure, J.; Mauchain, J.; Papalazarou, E.; Yan, W.; Pinon, J.; Marsi, M.; Perfetti, L. Full characterization and optimization of a femtosecond ultraviolet laser source for time and angle-resolved photoemission on solid surfaces. *Rev. Sci. Instrum* **83**, 043109 (2012).

[34] Hou, Z., Yang, B., Wang, Y. et al. Large and Anisotropic Linear Magnetoresistance in Single Crystals of Black Phosphorus Arising From Mobility Fluctuations. *Sci Rep* **6**, 23807 (2016).

[35] Paul D. Cunningham, Aubrey T. Hanbicki, Kathleen M. McCreary, and Berend T. Jonker. Photoinduced Bandgap Renormalization and Exciton Binding Energy Reduction in WS_2. *ACS Nano* **11**, 12, 12601–12608 (2017).

[36] Schultes, F. J.; Christian, T.; Jones-Albertus, R.; Pickett, E.; Alberi, K.; Fluegel, B.; Liu, T.; Misra, P.; Sukiasyan, A.; Yuen, H.; Haegel, N. M. Visualizing optical phase anisotropy in black phosphorus. *Appl. Rev. Lett* **103**, 242106 (2013).

[37] Shklovskii, B.; Efros, A. L. Electronic Properties of Doped Semiconductors. Springer, Heidelberg 1984.

Chapter 5 Spectroscopy of buried states in black phosphorous with surface doping

5.1 Motivation

Many layered materials are receiving strong interest for their potential applications in field effect transistors [1]. In this domain, the scientists have first focused their attention on graphene. Indeed, graphene has high carrier mobility and can be a nearly transparent conductor [2-4]. However, the zero bandgap limits the on-off current ratio in field-effect transistors [5] and many practical limits hinder the capability of inducing a sizable bandgap without compromising its electronic quality [6-8]. Thus, the development of other 2D materials, with widely tunable bandgap, is an essential step for the development of 2D nanoelectronics.

Black phosphorus (BP) is one of the most promising alternatives to graphene and consists of stacked layers of phosphorene. Figure 5.1 recalls the puckered honeycomb lattice structure (armchair-shaped along x, and zigzag-shaped along y) of black phosphorous. The strong anisotropic structure also explains the large anisotropic thermal, optical, and electronic transport properties [10-12]. Bingchen Deng and his colleagues revealed the unique thickness-dependent bandgap tuning properties in few layers black phosphorous, arising from the strong interlayer electronic-state coupling [9]. The band gap is roughly 0.3 eV in the bulk limit but increases to 2 eV when the layer number decreases down to the monoatomic thickness.

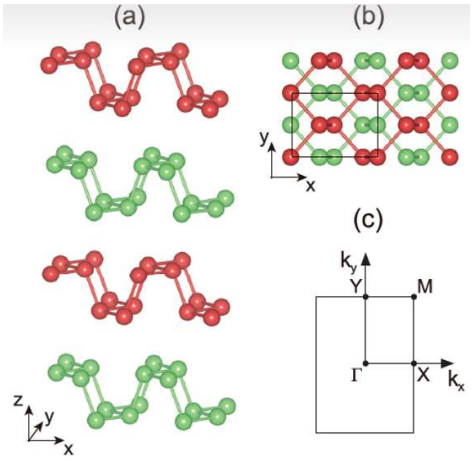

Figure 5.1: (a) Side view and (b) top view of the optimized structure of four-layer BP. For distinction, BP layers are alternately drawn with red and green spheres. In (b), the solid line represents the 1×1 unit cell. (c) Surface Brillouin zone.

Besides, the band gap of layered BP is extremely sensitive to external factors [13-15]. Several research groups made use of external parameters to tune the bandgap of few-

layer B such as strain [14, 16, 17], external electric field [15, 17-20] and alkali metals doping [21-23]. A depletion layer induced via electrostatic gating can shrink the band-gap by 35% [24]. Upon dual gating [9], it is possible to further approach the transition from a semiconductor to a Dirac semimetal. It has been even shown that the bandgap can be tuned from ~300 to below 50 meV by leveraging black phosphorous down to 10 nm-thick and using a moderate gate fields up to 1.1 $V \cdot nm^{-1}$. Such tuning of bandgap may not only extend the operational wavelength range of tunable black phosphorous photonic devices, but also pave the way for the investigation of electrically tunable topological insulators and semimetals [10, 25, 26]. Other authors have employed angle resolved photoelectron spectroscopy measurements to show that adsorption of alkaline metals at the sample surface generates a two dimensional electron gas that can be tuned across the band inversion point [21].

5.2 Concurrent work

Before discussing our measurements, we refer in this section to the previous work that has been done on a similar subject. As shown in Fig. 5.2, J. Kim et al. reported the realization of a widely tunable band gap in few-layer black phosphorus doped with potassium using an in situ surface doping technique [21]. Through band structure measurements and calculations, they demonstrated that a vertical electric field from dopants modulates the band gap, owing to the giant Stark effect based on surface dipoles formation, and tunes the material from a moderate-gap semiconductor to a band-inverted semimetal. And they argue that at the critical field of this band inversion, the material becomes a Dirac semimetal with anisotropic dispersion, linear along the armchair and quadratic along the zigzag directions.

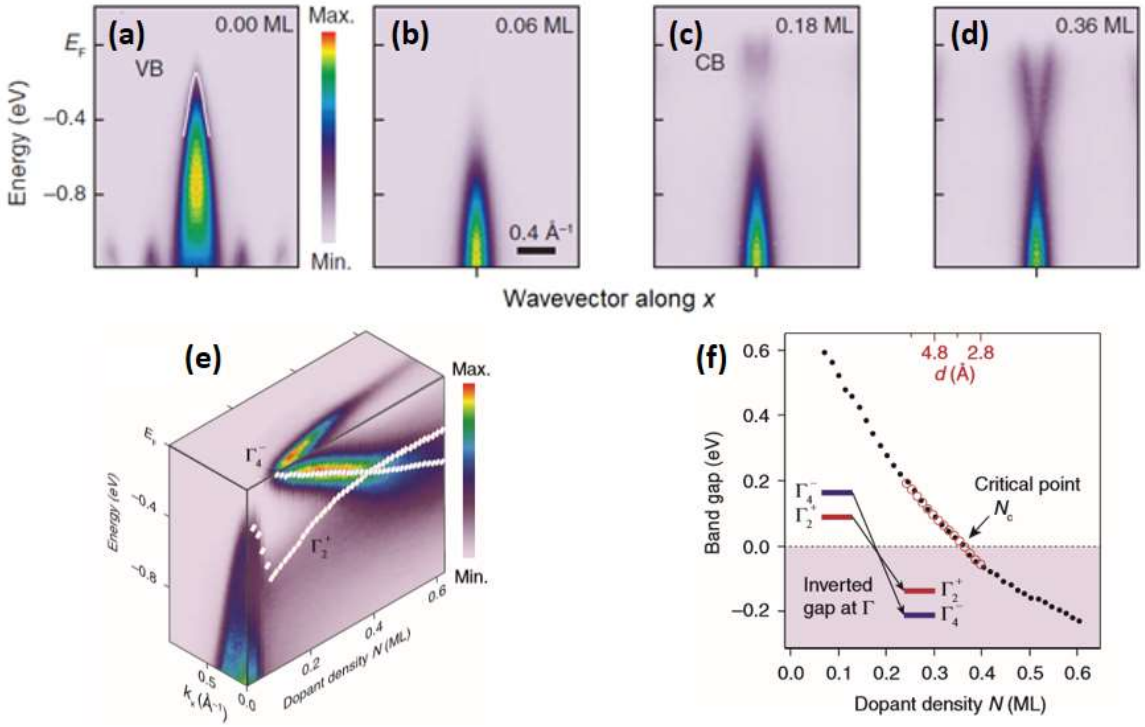

Figure 5.2: (a-d) Experimental band structure of BP taken at 15K near E_F along k_x with dopant density marked at the upper right of each panel. The photon energy is 104 eV for k_z at the Z point of the bulk Brillouin zone. The dopant density is estimated in units of monolayers from simultaneously taken K 3p core-level spectra. The white line overlaid in (a) is a fit to the VB with the k·p perturbation formula. (e) A 3D representation of the band evolution as a function of dopant density N, taken at 15 K. Diamonds and circles denote the positions of E_v and E_c, respectively. (f) E_g as a function of N. The negative gap in the shaded region represents the inverted gap at the G point. Overlaid red circles denote E_g from DFT band calculations where varying dopant density is simulated by changing the vertical distance d between K and BP [21].

As illustrated in Fig. 5.3, using density-functional theory calculations, S-W. Kim and his collaborators demonstrated that the donated electrons from K dopants are mostly localized in the topmost BP layer and this surface charging efficiently screens the K ion potential [22]. Moreover, they found that, at increasing of K doping, the extreme surface charging is mainly screened by electrons in the conduction band states, therefore decreasing the energy of the conducting band minimum. The electrons in the valence band maximum are less involved is such screening effect, so that the top of the valence band is display a smaller energy shift upon K atom evaporation. The authors write that such process explains the observed tunable band gap but also stress that such effect cannot be simply considered as equivalent to a giant Stark effect where a vertical electric field from the positively ionized K over layer to the negatively charged BP layers shifts the conduction band minimum Γ_{1c} (valence band minimum Γ_{8v}) downwards (upwards). The calculated

energy of Γ_{1c} and Γ_{8v} energies as a function of the K doping can qualitatively reproduces the tunable bandgap, anisotropic Dirac semimetal state, and band-inverted semimetal state that has been observed in an angle-resolved photoemission spectroscopy experiment [21].

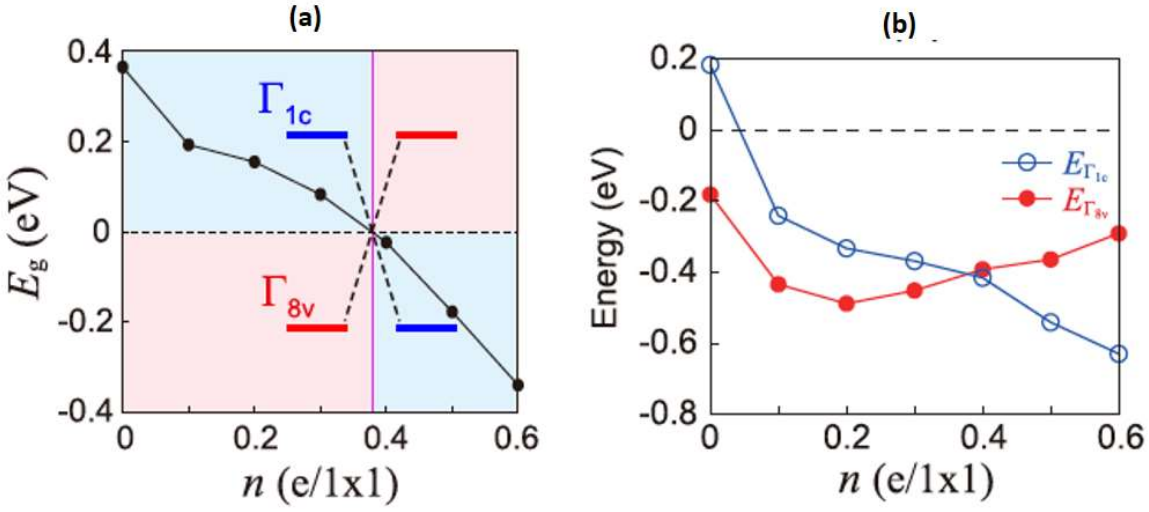

Figure 5.3: (a) E_g is displayed as a function of dopant density n, where the inversion of the C_1 and V_1 bands is shown schematically. (b) Calculated $E\Gamma_{1c}$ and $E\Gamma_{8v}$ relative to E_F as a function of n [22].

Figure 5.4 shows some angle-resolved photoemission spectroscopy measurements of N. Ehlen et al. on black phosphorus doped by evaporation of Cs atoms. As shown in Fig. 5.4, by selectively inducing a higher electron concentration (1.7×10^{14} cm^{-2}) in the topmost layer, the changes in the Coulomb potential are sufficiently large to cause surface band inversion between the parabolic valence band of BP and a parabolic surface state around the Γ point of the Brillouin zone. Besides they report the direct observation of a surface resonance state with an elliptical Fermi surface [23]. Tight-binding calculations show that band gap opening at the crossing points in the two high-symmetry directions of the Brillouin zone requires out-of-plane hopping and breaking of the glide mirror symmetry. Ab initio calculations are in very good agreement with the experiment if a stacking fault on the BP surface is taken into account.

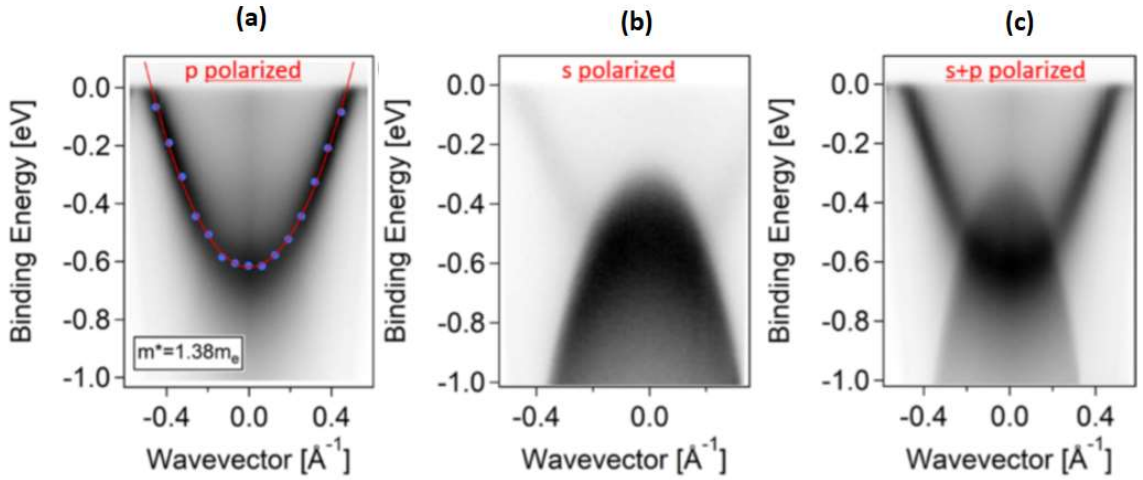

Figure 5.4: Two-dimensional, k-dependent ARPES spectra along the ΓY direction measured with (a) p- and (b) s-polarized light. A fit of the effective electron mass yielding $m_* = 1.38m_e$ is shown (m_e is the free-electron mass). (c) The s- and p-polarized spectra added together [23].

In spite of the published work on the subject, there is still a significant discrepancy between the evolution of bandgap that has been experimentally measured and theoretically predicted. In the general case, a rigid band bending occurs at very initial doping level whereas the band gap renormalization takes place only upon strong electron doping. Due to the formation of the accumulation layer, the wave functions of conduction band and valence band spatially redistribute in the puckered layer structure. This process has extreme consequences when alkali atoms are deposited on the surface of black phosphorous. Moreover, the reported experiments employed conventional ARPES in the soft-X-rays spectral region. Therefore, two limiting issues still challenge a quantitative analysis of the band gap collapse: 1) since BP is an intrinsic p-doped semiconductor [27], conventional ARPES cannot be employed to extract the band gap until the chemical potential crosses the conduction band minimum. As a consequence, the doping dependent evolution of the band gap can be monitored only at high carrier concentration [21, 28]. 2) As shown in Fig. 5.5, the surface dipole created by alkali metal evaporation pokes the wavefunction of the valence band towards the inner layers of BP [24]. It is therefore questionable whether a highly surface sensitive technique as ARPES can monitor the buried wavefunction of the valence band. As a matter of facts, the previous ARPES experiments at 20-100 eV observed an anomalous band gap of ~0.6 eV at the initial stage of electronic doping [21]. This trend is not compatible with scanning tunneling spectroscopy measurements [24] or ab-initio calculation of the band structure [22], casting doubts on the electronic nature of electronic states that have been effectively probed. In

order to shade light on this issue, we adopt time- and angle- resolved photoelectron spectroscopy (TrARPES) together with Cs doping to uncover the electron dynamics and band inversion in BP upon high surface doping.

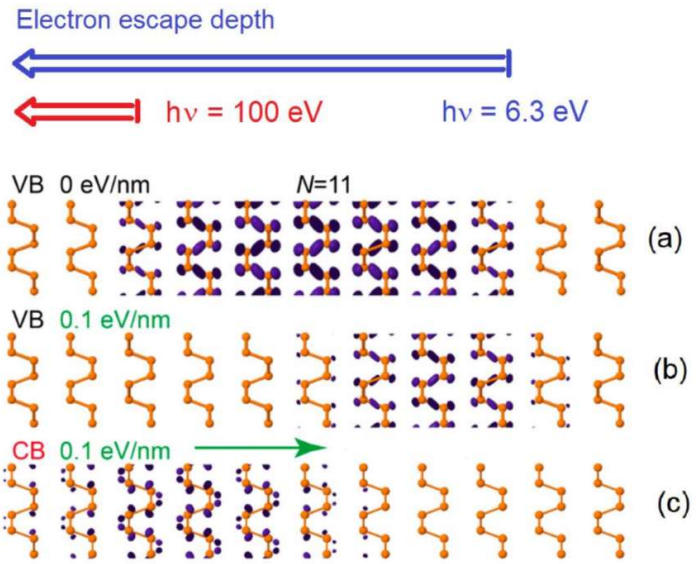

Figure 5.5: (a) Calculated spatial distribution of electronic density obtained by projecting the states at the top of the valence band on the atoms of a slab. (b) Puckering of valence band states after the application of 0.1 eV/nm field directed towards the right side of the slab. (c) Projected states of the conduction band minimum in the presence of the polarizing electric field. The blue and red arrow indicate the escape depth of photoelectrons probed by 6.3 eV and 100 eV, respectively. This image has been readapted from the calculations and pictures of reference 24.

5.3 Results and Discussion

The evaporation of alkali metals is a common approach to generate accumulation layers at the surface of semiconductors. Generally, the carrier concentration in the topmost layer is linearly dependent on the surface density of alkali atoms. We deposited increasing doses of Cesium (Cs) atoms by a commercial getter source. Fig. 5.6 shows a series of photoelectron intensity maps of the photoexcited state as function of surface doping along the armchair and zigzag direction. Due to matrix elements effects, the p-polarized probe couples strongly to the minimum of the conduction band. As a consequence, we choose p-polarized photons when the occupation of the conduction band is weak (panels a-m in Fig. 5.6) while we polarize at 30° with respect to p orientation at higher filling level (panels n-p in Fig. 5.6). We set the surface chemical potential μ of the photoexcited state (see white dashed line in the plots of Fig. 5.6) at the equilibrium value plus the Surface PhotoVoltage (SPV) shift.

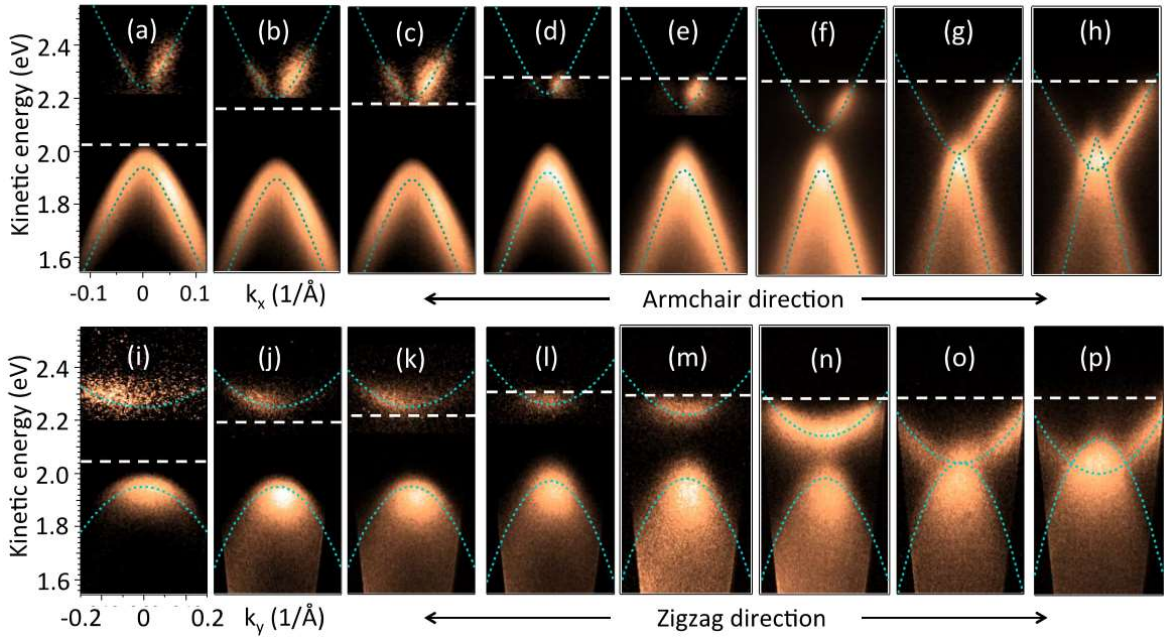

Figure 5.6: (a-h) Time-resolved ARPES data of BP along the armchair direction, as function of surface doping. (i-p) Time-resolved ARPES data of BP along the armchair direction, as function of surface doping. The dashed lines indicate the position of Fermi level. At low doping levels in (a-c) and (i-k), the gap has been visualized by measuring the photoelectron intensity maps at delay time of 1 ps after photoexcitation. At high doping levels in (d-h) and (l-p), the gap has been visualized by measuring the photoelectron intensity maps at negative delay. The conduction band signal of (a-e) and (i-l) has been multiplied by factors between 5 to 200, in order to equalize the intensity of the color scale.

The equilibrium chemical potential is obtained by acquiring an ARPES intensity map without pump pulse. Upon photoexcitation, a steady SPV shifts the photoelectron intensity map with respect to the equilibrium case. Near to the surface of a doped semiconductor, the local equilibration of charge balance induces a depletion layer of roughly 100 nanometers thick. In this region a built in field is responsible for a rigid bending of the conduction and valence bands. The application of a pump beam generates a density of free carriers that screens the built in field of the depletion layer and induces a steady state with flat bands. We can quantify the pre-existing band bending by comparing the photoelectrons intensity maps acquired without pump beam and with pump beam at negative delay. The two photoelectron intensity maps differ by a rigid shift that is called SPV and equals the pre-existing band-bending in the high photoexcitation regime. Figure 5.7 shows the SPV amplitude of BP with various doping levels as a function of pump fluence (ρ). In pristine BP ($\mu - E_{CB} = -0.22$ eV), after irradiation by the pump ($\rho > 1$ μJ/cm^{-2}), the SPV amplitude saturates at -0.013 eV. The slightly negative SPV amplitude corresponds to a pre-existing upward band bending when BP sample is cleaved in

vacuum. At the initial stage of Cs evaporation (-0.22 eV< μ - E_{CB} < 0 eV), the SPV amplitude changes sign (from negative to positive) and then it increases up to the maximal value of 0.25 eV. The data shown in the next part have been acquired at pump fluence ρ > 230 μJ/cm^{-2}, corresponding to the saturation regime of the SPV. As a consequence, the measured SPV provides a direct estimate of the pre-existing band bending for different amount of the surface electron doping. As stated in the next discussion, the internal reference μ is defined as the surface chemical potential in equilibrium plus the SPV shift.

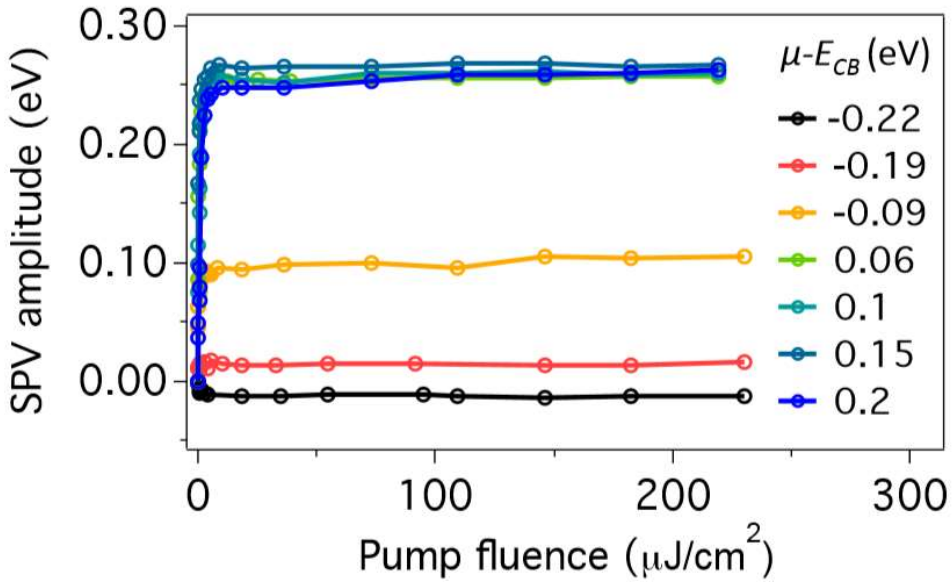

Figure 5.7: SPV amplitude in surface electron doped BP as function of pump fluence. The doping level is quantified by the difference between chemical potential μ and the minimum of conduction band energy E_{CB}.

In agreement with previous finding, the alkali metal evaporation induces a surface dipole that dramatically restructures the electronic states in the accumulation layer. Fig. 5.8 shows the energy shifts of conduction band minimum E_{CB} and valence band maximum E_{VB} as a function of electron doping. The energies E_{CB} and E_{VB} are referred with respect to the surface chemical potential μ. As a function of Cs deposition, E_{CB} decreases ~0.52 eV monotonously whereas E_{VB} decreases ~0.29 eV linearly for μ–E_{CB} ≤ 0.07 eV and subsequently increases for μ–E_{CB} > 0.07 eV. Our observations are in excellent agreement with the density-functional theory (DFT) calculations with generalized-gradient approximation functional of Perdew-Burke-Ernzerhof (PBE) performed by S-W. Kim et al [22]. In their calculations, the E_{CB} decreases ~0.6 eV monotonously until the band gap closes, the E_{VB} decreases ~0.3 eV at the initial doping level (carrier concentration ~0.2 electron per 1x1 unit cell) while increases ~0.1 eV afterwards.

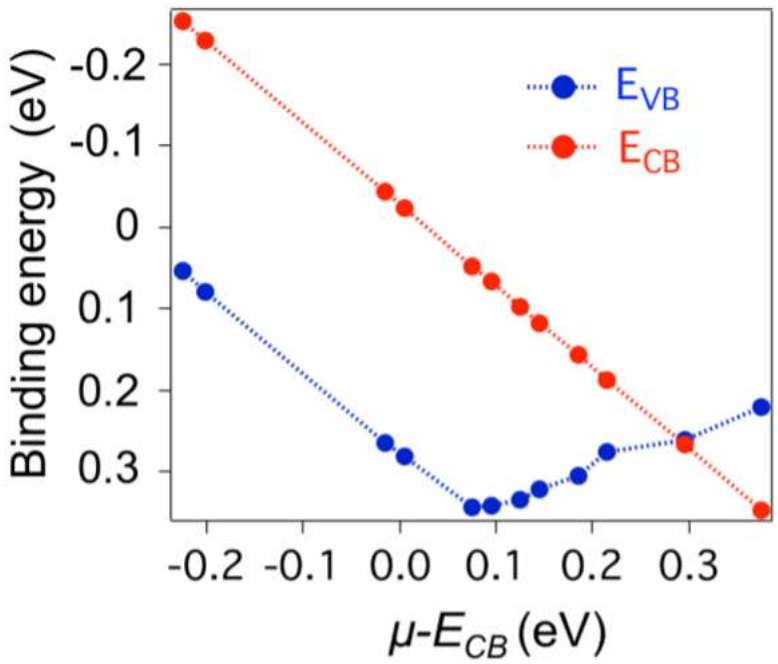

Figure 5.8: the rigid shifts of conduction band (valence band) as a function of electron doping.

In Fig. 5.9, we plot the gap value Δ (energy of the conduction band minimum E_{CB} minus energy valence band maximum E_{VB}) as a function of the energy distance μ - E_{CB}. Note that the band gap of BP keeps constant at ~0.32 eV as long as the chemical potential lies within the gap (μ - E_{CB} <0). In this regime the surface doping mainly compensates the acceptor states due to intrinsic vacancies. Note that the initial Δ = 0.32 eV is in good agreement with scanning tunneling spectroscopy data acquired on a pristine surface [24] and with infrared measurements of a bulk sample [27]. The band gap decreases linearly with μ - E_{CB} when the charge transfer starts to fill the conduction band of the topmost layers. The inversion point E_{CB} = E_{VB} takes place when μ - E_{CB} = 0.35 eV, while Δ reaches the negative value of -0.2 eV at the largest doping level. We can estimate the electronic density in the accumulation layer from the area of the electronic pocket at a given filling of the conduction band (Luttinger theorem). The ellipsoid area $\pi k^F_x k^F_y$ results in an electronic density of 4.5 × 10^{13} 1/cm^2 at the inversion point. This value is roughly a factor of two lower than the critical surface density reported by ARPES experiments at higher photon energy [21].

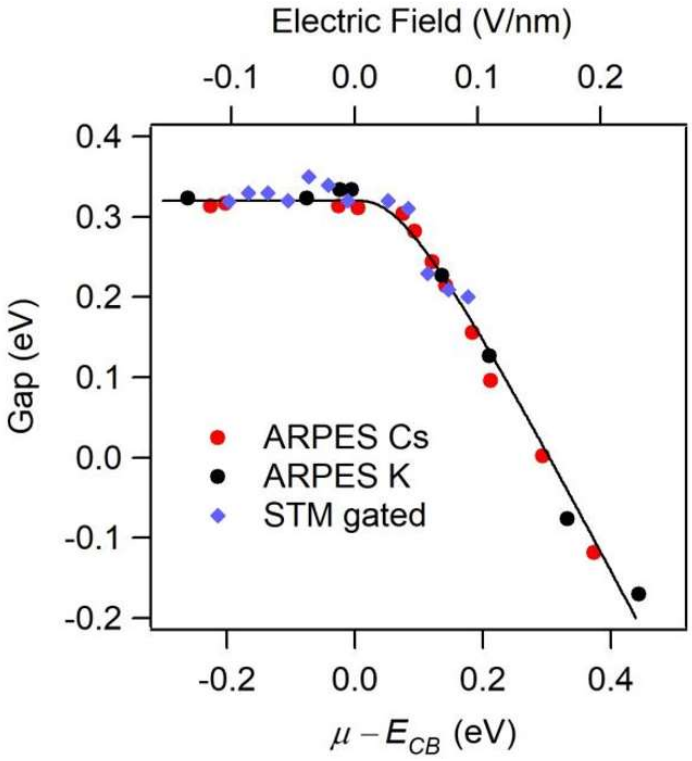

Figure 5.9: Band gap at the surface of BP as function of surface doping by deposition of Cs atoms (red filled circles) and K atoms (black filled circles), respectively. The surface doping (bottom axis) is quantified by the difference between chemical potential μ and the minimum of the conduction band energy E_{CB}. The solid line is a guide to the eye. As a term of comparison, the gap value (blue diamond) as function of polarizing field (top axis) is extracted from Ref. 24.

As shown by Fig. 5.9, the evaporation of potassium (K) instead of Cs atoms generate very similar results. It is interesting to compare in Fig. 5.9 the band gap evolution of our experiment with scanning tunneling spectroscopy of a gated BP flake [24]. The agreement between the two different measurements is excellent if we assume that a stark field of 0.1 V/nm displaces the chemical potential by 0.2 eV. Furthermore, our data are consistent with the monotonic decrease of gap value that has been reported by density-functional theory (DFT) calculations [22]. These favorable comparisons indicate that our experiment is indeed detecting the conduction and valence band states of the accumulation layer. The calculated local density of electronic states supports our claim. As shown in Fig. 5.5, the square wavefunction of electronic states at the top of the E_{VB} shifts by roughly 5 nm away from the surface upon the application of an external electric field of 0.1 V/nm [24]. This distance is comparable to the escape depth of photoelectrons generated by 6.3 eV photons whereas is 5 times longer than the photoelectron escape depth of a ~100 eV probing source. We have recently shown that topological states buried by absorbed

molecules can be visible by laser based ARPES while they go undetected at higher photon energy [29]. By the same token, we think that the synchrotron based experiments would fail to observe the top of valence band of the accumulation layer. This conjecture would naturally explain the unrealistic estimate of gap size that has been previously reported [21,28].

In order to gain quantitative insights on the evolution of electronic states, we fit the dispersions along the armchair direction by the pseudorelativistic expression $E = E_0 \pm (\delta + (m^2v_x^4 + v_x^2p^2)^{1/2})$, where $m_x = m_x^c (m_x = m_x^v)$ is the effective mass for conduction band (valence band), $v_x = v_x^c$ ($v_x = v_x^v$) is the band velocity in the linear section of conduction band (valence band) and δ is a constant. Along the zigzag direction, the dispersion follows the parabolic form $E = \Delta/2 \pm p^2/2m_y$, where Δ is the band gap, $m_y = m_y^c$ ($m_y = m_y^v$) is the effective mass of the conduction band (valence band). As shown by the dotted lines in Fig. 5.6, the fitting curves reproduce with high accuracy the band dispersion along both crystallographic axes. The band gap is identified with $2(\delta + m_x v_x^2)$ in the armchair direction and with Δ in the zigzag one. As expected, $\Delta = 2(\delta + m_x v_x^2)$ is satisfied for each of the doping levels (with error bars of ± 0.03 eV). The deformation of band dispersion upon electron doping is quantified by extracting fitting parameters for each band and high symmetry direction. Along zigzag direction, the fitting parameters m_y does not depend on Cs deposition, neither for the conduction band ($m_y^c = 0.9 \pm 0.2 m_e$) nor for valence band ($m_y^v = 0.4 \pm 0.1 m_e$)). Along armchair direction, the Cs evaporation does not modify the fitting in the conduction band parameter $m_x^c = 0.055 \pm 0.01 m_e$ and $v_x^c = 0.7 \pm 0.1 \times 10^6$ m/s. Nonetheless, Fig. 5.6 (a-h) show a very interesting evolution of the valence band along the armchair direction.

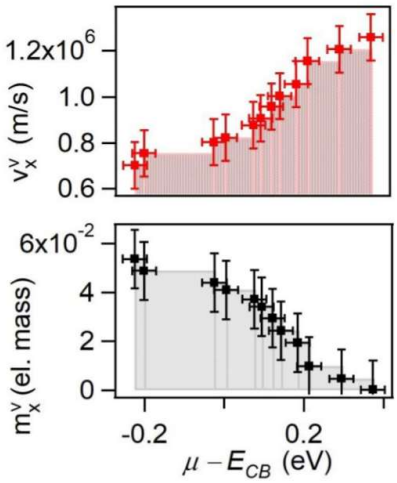

Figure 5.10: The fermi velocity (top panel) and effective mass (bottom panel) of the valence band along armchair direction and as function of doping level.

Fig. 5.10 shows the values of v_x^v and m_x^v as a function of μ - E_{CB}. Upon increasing doping level, the effective mass m_x^v shrinks below the detection limit while v_x^v increases by nearly two times (from v_x^v = 0.7 ± 0.1 × 10^6 m/s to v_x^v = 1.25 ± 0.1 × 10^6 m/s). A similar tuning of Fermi velocity has been previously achieved in graphene by employing substrates of different dielectric constant [30]. The maximal v_x^v = 1.25 × 10^6 m/s value of this work is already higher than the Fermi velocity reported for graphene on SiC substrate and it is only a factor of two lower that the value reported in suspended graphene sheets [31]. The electron-electron interaction and the substrate polarizability explain the modified dispersion observed in graphene. Here instead, the formation of an accumulation layer shapes the Fermi velocity and effective mass. Eventually, the anisotropic screening due to the self-organization of alkali metals should also be considered [32]. Further theoretical and experimental investigations will be necessary in order to clarify this issue.

5.4 Conclusions

In this work, we performed time- and angle- resolved photoelectron spectroscopy of BP with surface doping. Awing for the larger escape depth of electrons emitted by a probe photon energy of 6.3 eV, we could observe the evolution of the buried valence band as a function of alkali metal deposition. Our data show that the band gap decreases monotonically from the bulk value of 0.32 eV down to the inversion point. This finding is in excellent agreement with scanning tunneling spectroscopy measurements of gated BP and first principle calculations. A closer inspection reveals that the Fermi velocity of the electrons in the valence band increases by a factor of 2 upon doping the BP surface by Cs atoms. At the highest carrier concentration Fermi velocity of doped BP exceeds the value of the Dirac fermions in graphene on Silicon Carbide. This observation suggests that mobility of excited electrons in the accumulation layer of black phosphorous may considerably increase at large carrier density.

References

[1] Geim, A., Grigorieva, I. Van der Waals heterostructures. *Nature* **499**, 419–425 (2013).

[2] K.S.Novoselov, A.K.Geim, S.V.Morozov, D.Jiang, Y.Zhang, S. V. Dubonos, I. V. Grigorieva, and A. A. Firsov. Electric Field Effect in Atomically Thin Carbon Films. *Science* **306**, 666 (2004).

[3] Novoselov, K., Geim, A., Morozov, S. et al. Two-dimensional gas of massless Dirac fermions in graphene. *Nature* **438**, 197–200 (2005).

[4] Zhang, Y., Tan, Y., Stormer, H. et al. Experimental observation of the quantum Hall effect and Berry's phase in graphene. *Nature* **438**, 201–204 (2005).

[5] F. Xia, D. B. Farmer, Y.-M. Lin, and P. Avouris. Graphene field-effect transistors with high on/off current ratio and large transport band gap at room temperature. *Nano Lett*. **10**, 715 (2010).

[6] Kim, G., Shao, L., Zhang, K. et al. Engineered doping of organic semiconductors for enhanced thermoelectric efficiency. *Nature Mater* **12**, 719–723 (2013).

[7] E. S. Reich, Phosphorene excites materials scientists. *Nature* **506**, 19 (2014).

[8] Churchill, H., Jarillo-Herrero, P. Phosphorus joins the family. *Nature Nanotech* **9**, 330–331 (2014).

[9] Deng, B.; Tran, V.; Xie, Y.; Jiang, H.; Li, C.; Guo, Q.; Wang, X.; Tian, H.; Koester, S. J.; Wang, H.; Cha, J. J.; Xia, Q.; Yang, L.; Xia, F. Efficient electrical control of thin-film black phosphorus bandgap. *Nature Comm*. **8**, 14474 (2017).

[10] L. Kou, C. Chen, and S. C. Smith. Phosphorene as a Superior Gas Sensor: Selective Adsorption and Distinct I–V Response. *J. Phys. Chem. Lett*. **6**, 2794 (2015).

[11] X. Ling, H. Wang, S. Huang, F. Xia, and M. S. Dresselhaus, The renaissance of black phosphorus. *Proc. Natl. Acad. Sci. USA* **112**, 4523 (2015).

[12] Z. Li, T. Cao, M. Wu, and S. G. Louie, Generation of Anisotropic Massless Dirac Fermions and Asymmetric Klein Tunneling in Few-Layer Black Phosphorus Superlattices. *Nano Lett*. **17**, 2280 (2017).

[13] R. Fei and L. Yang. Strain-Engineering the Anisotropic Electrical Conductance of Few-Layer Black Phosphorus. *Nano Lett*. **14**, 2884 (2014).

[14] A. S. Rodin, A. Carvalho, and A. H. Castro Neto. Strain-Induced Gap Modification in Black Phosphorus. *Phys. Rev. Lett.* **112**, 176801 (2014).

[15] Q. Liu, X. Zhang, L. B. Abdalla, A. Fazzio and A. Zunger, Switching a Normal Insulator into a Topological Insulator via Electric Field with Application to Phosphorene. *Nano Lett*. **15**, 1222 (2015).

[16] X. Peng, Q. Wei, A. Copple. Strain-engineered direct-indirect band gap transition and its mechanism in two-dimensional phosphorene. *Phys. Rev. B* **90**, 085402 (2014).

[17] Y. Li, S. Yang, J. Li. Modulation of the Electronic Properties of Ultrathin Black Phosphorus by Strain and Electrical Field. *J. Phys. Chem. C* **118**, 23970–23976 (2014).

[18] J. Dai, X. C. Zeng. Bilayer Phosphorene: Effect of Stacking Order on Bandgap and Its Potential Applications in Thin-Film Solar Cells. *J. Phys. Chem. Lett*. **5**, 1289–1293 (2014).

[19] H. Guo, N. Lu, J. Dai, X. Wu, X. C. Zeng. Phosphorene Nanoribbons, Phosphorus Nanotubes, and van der Waals Multilayers. *J. Phys. Chem. C* **118**, 14051–14059 (2014).

[20] Qingyun Wu, Lei Shen, Ming Yang, Yongqing Cai, Zhigao Huang, and Yuan Ping Feng. Electronic and transport properties of phosphorene nanoribbons. *Phys. Rev. B* **92**, 035436 (2015).

[21] Kim, J.; Baik, S. S.; Ryu, S. H.; Sohn, Y.; Park, S.; Park, B.-G.; Denlinger, J.; Yi, Y.; Choi, H. J.; Kim, K. S. Observation of tunable band gap and anisotropic Dirac semimetal state in black phosphorus. *Science* **723**, 349 (2015).

[22] Sun-Woo Kim, Hyun Jung, Hyun-Jung Kim, Jin-Ho Choi, Su-Huai Wei, and Jun-Hyung Cho. Microscopic mechanism of the tunable band gap in potassium-doped few-layer black phosphorus. *Phys. Rev. B* **96**, 075416 (2017).

[23] N. Ehlen, A. Sanna, B. V. Senkovskiy, L. Petaccia, A. V. Fedorov, G. Profeta, and A. Grüneis. Direct observation of a surface resonance state and surface band inversion control in black phosphorus. *Phys. Rev. B* **97**, 045143 (2018).

[24] Liu, Y.; Qiu, Z.; Carvalho, A.; Bao, Y.; Xu, H.; Tan, S. J. R.; Liu, W.; Castro Neto, A. H.; Loh, K. P.; Lu, J. Gate-Tunable Giant Stark Effect in Few-Layer Black Phosphorus. *Nano Lett* **17**, 1970 (2017).

[25] Liu, H.; Neal, A. T.; Zhu, Z.; Luo, Z.; Xu, X.; Tomnek, D.; Ye, P. D. Phosphorene: An Unexplored 2D Semiconductor with a High Hole Mobility. *ACS Nano* **8**, 4033 (2014).

[26] Li, L., Kim, J., Jin, C. et al. Direct observation of the layer-dependent electronic structure in phosphorene. *Nature Nanotech* **12**, 21–25 (2017).

[27] Morita, A. Semiconducting black phosphorus. *Appl. Phys. A* **39**, 227 (1986).

[28] J. Kim, M. Huh, S.W. Jung, S.H. Ryu, Y. Sohn, K.S. Kim, Electronic band structure of surface-doped black phosphorus. *J. Electron Spectrosc*. **219** 86–91 (2017).

[29] Caputo, M.; Panighel, M.; Lisi, S.; Khalil, L.; Di Santo, G.; Papalazarou, E.; Hruban, A.; Konczykowski, M.; Krusin-Elbaum, L.; Aliev, Z. S.; Babanly, M. B.; Otrokov, M. M.; Politano, A., Chulkov, E. V.; Arnau, A.; Marinova, V.; Das, P. K.; Fujii, J.; Vobornik, I.; Perfetti, L.; Mugarza, A.; Goldoni, A.; Marsi M. Manipulating the Topological Interface by Molecular Adsorbates: Adsorption of Co-Phthalocyanine on Bi_2Se_3. *Nano Lett*. **16**, 34093414 (2016).

[30] Hwang C, Siegel D A, Mo S-K, Regan W, Ismach A, Zhang Y, Zettl A and Lanzara A. Fermi velocity engineering in graphene by substrate modification. *Sci. Rep*. 2590 (2012).

[31] Elias, D., Gorbachev, R., Mayorov, A. et al. Erratum: Dirac cones reshaped by interaction effects in suspended graphene. *Nature Phys* **8**, 172 (2012).

[32] Kiraly, B., Knol, E. J.; Volckaert, K.; Biswas, D.; Rudenko, A. N.; Prishchenko, Vladimir, D. A.; Mazurenko, G.; Katsnelson, M. I.; Hofmann, P.; Wegner, D.; and Khajetoorians, A. A. Anisotropic Two-Dimensional Screening at the Surface of Black Phosphorus. *Phys. Rev. Lett.* **123**, 216403 (2019).

Chapter 6 Tunability of hot-carrier dynamics in black phosphorus

As described in chapter 4, the band gap of BP can be closed with the formation of a Dirac point and even inversed, eventually leading to a pair of Weyl points with twofold degeneracy [1]. In addition to the bandgap modulation, also the hot-carrier dynamics can be tuned by changing the surface carrier density or by other means [2-5]. An active control of the underlying ultrafast charge carrier dynamics will be helpful to gain more insights into the different mechanisms leading to carrier's relaxation. In the following section we introduce some relevant experimental results on this issue.

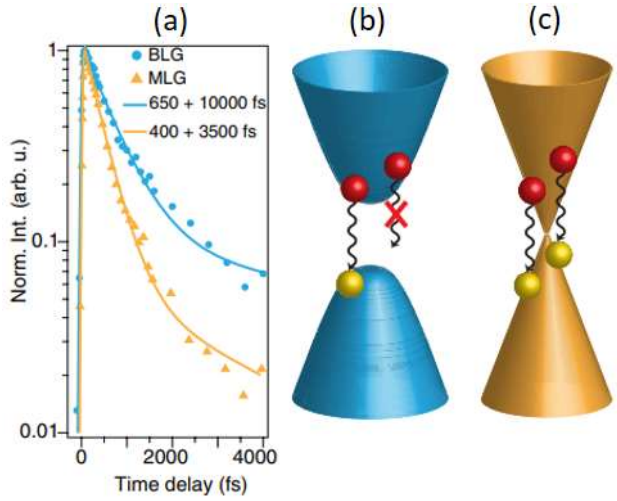

Figure 6.1: (a) Integrated intensity in the bottom of the conduction band of both BLG and MLG. Lines correspond to double-exponential function fits with the given time constants. The fluence is 0.6 mJ/cm^2 for all data presented here. (b), (c) Sketch of the relaxation dynamics involving hot electrons (red spheres), holes (yellow spheres), and phonon emission (wiggled arrows) around the Dirac point for (b) massive Dirac Fermions and (c) massless Dirac Fermions [6].

6.1 Concurrent work

Søren Ulstrup and his collaborators directly followed the excited carriers in bilayer graphene on a femtosecond time scale, using ultrafast time- and angle-resolved photoemission [6]. They found a behavior consistent with a single-particle band gap. Compared to monolayer graphene, the existence of this band gap leads to an increased carrier lifetime in the minimum of the lowest conduction band. Figure 6.1 (a) show the different evolution of electronic occupation factor at very bottom of the conduction band for bilayer graphene (BLG) and monolayer graphene (MLG). The data sets for BLG (MLG)

can be well-described by a double-exponential decay, where an initial fast decay with a decay time of 650 fs (400 fs) is followed by a slow decay with 10 ps (3.5 ps). Without a gap, hot electrons can cascade down continuously via acoustic phonon scattering, whereas the presence of the gap requires relaxations by optical phonons, giving rise to a bottleneck for the decay [see sketch in Figs. 6.1 (b) and 6.1 (c)].

Johannsen, J. C. et al took advantage of TR-ARPES to show in a direct manner that the dynamical response of the Dirac carriers in graphene to a photoexcitation can be tuned by varying the doping level, that is, the position of the fermi level (FL) relative to the Dirac point (DP) [7]. The subsequent recombination of the hot carriers via phonon-emitting processes is significantly more efficient in the strongly n-doped graphene compared to the weakly p-doped graphene, as a consequence of the reduced phase-space for decay imposed by the vanishing density of states at the DP. The detailed experimental result is displayed in Fig. 6.2. Both data sets can be also well-fitted by a double-exponential decay where an initial fast decay with a decay time of 335 fs (87 fs) for p-doped graphene (n-doped graphene) is followed by a slow decay with 2750 fs (490 fs). This proof of principle on graphene has not been obtained by fine tuning the doping level. Moreover, lack of reports addresses the dynamics of the photoexcited electron distribution in BP upon varying doping level. Clarification of this issue is suitable for assessing microscopic scattering mechanisms in electron doped BP and defining whether charge carriers exhibit a metallic or a semiconducting relaxation after photoexcitation.

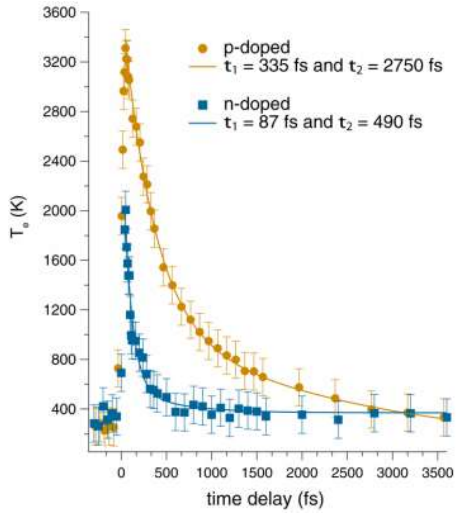

Figure 6.2: The fitted electronic temperature (with error-bars added) for the *n*- (blue markers) and the *p*-doped graphene (amber markers) as a function of time delay. Lines are the result of double exponential function fits to the data. The obtained time constants are indicated [7].

6.2 Results and Discussion

Here we combine ultrafast photoemission spectroscopy (pump fluence of 230 μJ/cm^2) with in situ electron doping technique, in order to directly map the transient occupation of dispersive electronic states in momentum space as functions of delay time and carrier concentration. It is worth to address that BP is an ideal system for this study as the Fermi level and band gap can be tuned significantly according to the doping and rich playground of physical phenomena can be directly observed such as: i) Under initial and weak electron doping, the chemical potential can be tuned from an energy position near the top of valence band to near the bottom of conduction band, which corresponds a p- to n-type conversion of the surface. At moderate electron doping, the chemical potential enters into conduction band and becomes the Fermi level of a two dimensional electron gas. It is our aim to monitor the behavior of hot-carrier dynamics at these doping levels. ii) Under strong electron doping, the band gap of BP monotonically shrinks to zero, changing the material from a moderate-gap semiconductor to a band-inverted semimetal. It is in this respect interesting to investigate the evolution of hot-carrier dynamics starting from the semiconductor behavior all the way to a semimetallic one. The tunability of the ultrafast dynamics at different doping levels may enable an effective manipulation of BP's optoelectronic properties for specific applications.

Figure 6.3 (a) shows a series of photoelectron intensity maps as function of surface doping along the armchair direction, acquired before pump excitation. The band gap of BP is linearly dependent on carrier concentration and we will use it as indication of the doping level. The band gap of BP is Δ= 0.31 eV, 0.27 eV, 0.21 eV, 0.12 eV and -0.02 eV respectively from the left panel to the right panel in Fig. 6.3 (a). The modulation of valence band maximum, conduction band minimum and band gap of BP as function of electron doping are similar to the previous ARPES measurement and theoretical calculations [8, 9]. Sudden injection of hot carriers in the conduction band of BP by an ultrafast pump pulse centered at 1.57 eV induces a direct transition of electrons from the valence band to conduction band. Since the band gap in pristine and p-type doped BP of our crystal is roughly 0.31 eV, the excess energy of excited carriers is always much larger than the band gap. We choose the corresponding photoelectron intensity maps as a function of doping at delay time of 0.8 ps as presented in Fig. 6.3 (b). At the same delay time, one can observe that the hot-carrier distribution is closer to the Fermi level as function of doping, which is an indication of a faster thermalization process induced by electron-electron interaction. Figure 6.3 (c) shows the integrated intensity of photoelectron intensity maps at negative delay and positive delay (t = 0.8 ps). The hot electron temperature T_e at delay time of 0.8

ps can be extracted from the fitting of the integrated curve with a Fermi-Dirac distribution. The only notable exception is on the pristine BP where it is not possible to extract it because the Fermi level is inside the gap. As we can see from the result, the K_BT_e decreases from 60 meV at Δ= 0.27 eV to 30 meV at Δ= -0.02 eV by a factor of two at the same delay time, mainly due the higher filling level of the conduction band.

The effect of bringing the electronic system out of its thermodynamic equilibrium state can be visualized by taking the difference between each photoelectron intensity map acquired for positive delay time and the equilibrium maps taken at a negative delay time, as show in Fig. 6.4 (a-d). Red and blue colors represent an increase or depletion of spectral weight, respectively. These panels offer a visual guide of the thermalization and recombination processes at four doping levels: pristine BP in Fig. 6.4 (a) (Δ= 0.31 eV), the moderate electrons doped BP in Fig. 6.4 (b-c) (Δ= 0.27 eV and 0.21 eV) and strong electron doped BP (Δ= -0.02 eV) in Fig. 6.4 (d). When the Fermi level enters in the conduction band, the distribution hot electrons with energy above the chemical potential is restrained to small excess energy. Second, the intensity of hot electrons signal attains the maximal value on a thermalization timescale that becomes faster under the moderate and strong doping level (in comparison to pristine BP). We also noticed that when BP is slightly electron doped and the Fermi level is in the gap, the thermalization dynamics is basically identical to the result observed from the pristine BP.

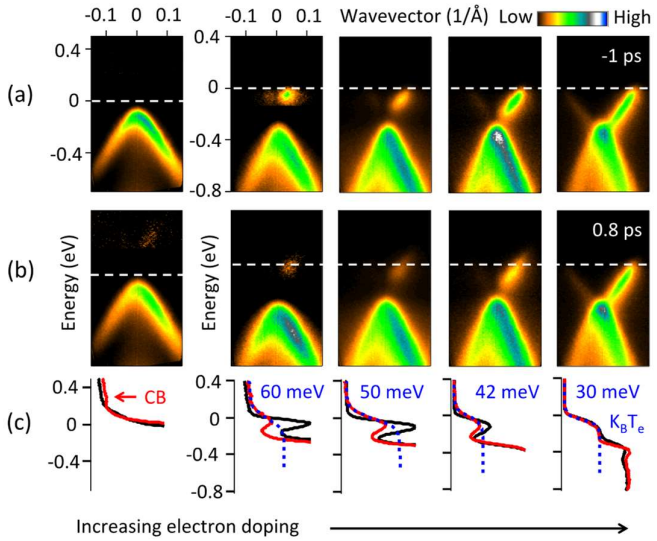

Figure 6.3: (a) Photoelectron intensity maps of BP as function of electron doping acquired at negative delay. (b) Photoelectron intensity maps of BP as function of electron doping acquired at delay time of 0.8 ps. The dashed white lines indicate Fermi levels. The photoelectron intensity in pristine and initial doped BP has been multiplied by a factor of 60 and 10 in order to visualize the conduction band. (c) Wavevector integrated intensity at negative delay (black curve) and 0.8 ps after photoexcitation (red curve). The dashed blue curve is the estimated Fermi-Dirac distribution. The electronic temperature is extracted from the distribution.

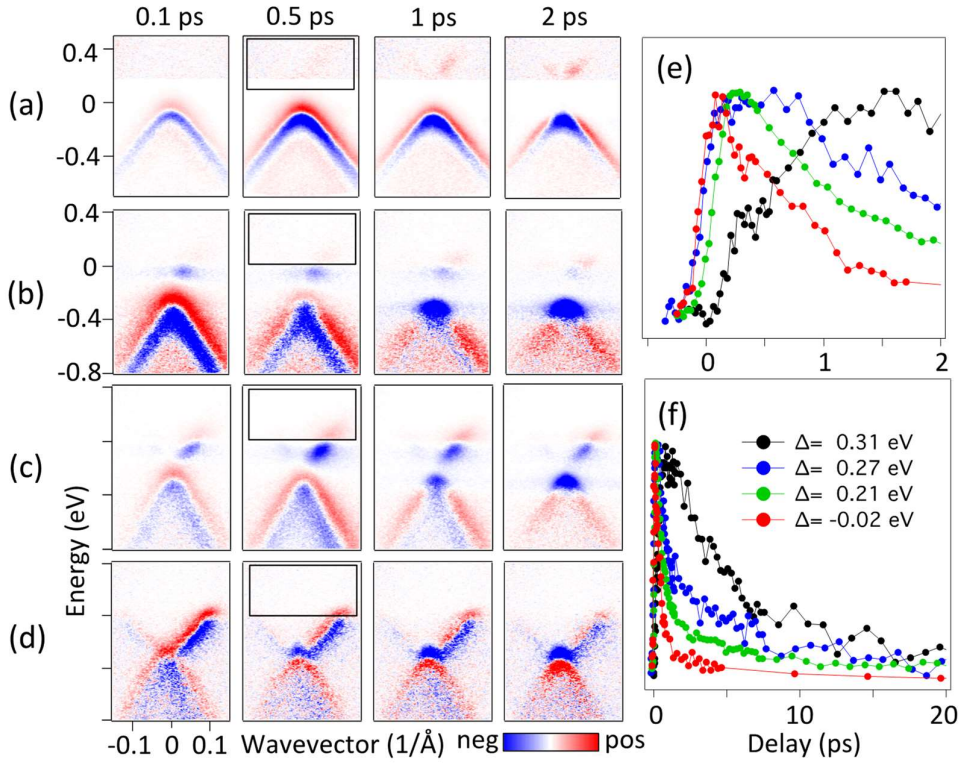

Figure 6.4: (a-d) Differential intensity map obtained by subtracting the photoelectron intensity at negative delay from the photoelectron intensity at positive delay. The panels from left to right display data acquired at increasing delay time after photoexcitation. (a), (b) (c) and (d) columns correspond to the different doping levels with band gap Δ= 0.31, 0.27, 0.21, -0.02 eV respectively. (e-f) Temporal evolution of the pump induced signal integrated from the rectangles in (a-d) for short and long delay times.

In order to extract the effects of electron doping on the dynamics, Fig. 6.4 (e-f) shows the integrated intensity of photo induced excited states (integrated from the rectangles in Fig. 6.4 (a-d)) above the Fermi level at short and long delay time, respectively. The thermalization time can be associated to the delay at which photoexcited electron intensity becomes maximal above the chemical potential (area marked by the black rectangle). By looking at the temporal evolution of the excited carrier density at early delay (from 0 to 2 ps), it is clear that the thermalization of photoexcited electrons becomes significantly faster by increasing electron doping. In pristine BP, the intensity gradually builds up, reaching its maximum at t ≈1.5 ps. However, the thermalization time drops exponentially after moderate electron doping, becoming 0.76 ps and 0.26 ps when Δ= 0.27 eV and Δ= 0.21 eV, respectively. At strong electrons doping, when the band gap vanishes, the thermalization time of hot carriers is 0.15 ps, which approaches the time resolution of our setup. In total, the thermalization time decreases more than 10 times in strong electron doped BP compared to the pristine one. The recombination time of hot carriers can be

extracted from the longer decay process shown in Fig. 6.4 (f). It is obvious that the recombination process is much faster in electron doped than in pristine BP. The recombination time constant τ can be obtained by fitting the curves with an exponential decay function. The recombination process is relatively long in pristine BP, where τ has the value of 9.4 ps. Interestingly, the recombination time follows the same trend of thermalization time in Fig. 6.5, which drops down quickly and then decreases slowly as function of electron doping. This result strongly suggests that both the reduction of thermalization time and recombination time are affected by an increase phase space for scattering events upon increasing doping level. However, the thermalization time is mainly driven by electron-electron interaction whereas the recombination time may also be sizably affected by electron-phonon scattering. The change of hot carriers dynamics in BP is more pronounced than in graphene where the recombination time drops only by a factor 5 times when going from the p-doped sample than in the n-doped one [7].

Since the electrons doping changes both the chemical potential and bandgap of BP, it is important to clarify which of the two effects is most relevant to the relaxation processes. Remember that the hot carriers dynamics keeps almost the same when BP is slightly electron doped and the Fermi level is in the gap, even though the semiconductor type has been tuned from p to n. Furthermore, the band gap keeps constant under this condition from our recent study. Note that the dynamics gets faster immediately after the Fermi level enters conduction band and BP becomes metallic. In this case, new channels of electron scattering can be access by a largely increased phase space. At larger doping levels, the further reduction of band gap does not change much the relaxation time.

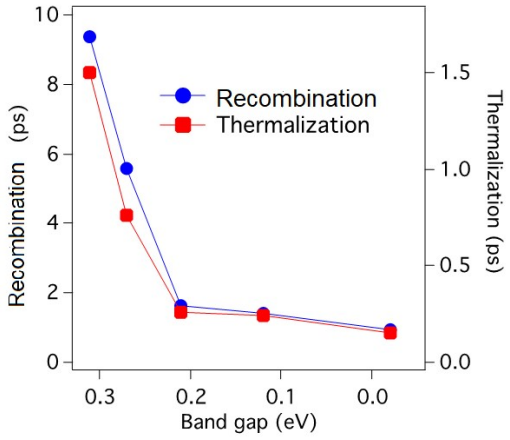

Figure 6.5: The thermalization time and recombination time τ in a series of electron doped BP. The band gap shrinks linearly with doping level as is employed here as reference. The thermalization time is defined as pump probe delay value when the photoelectron intensity above the Fermi level attains the maximal value. The recombination time τ is the time constant obtained from the exponential fitting of the subsequent decay of hot electrons signal.

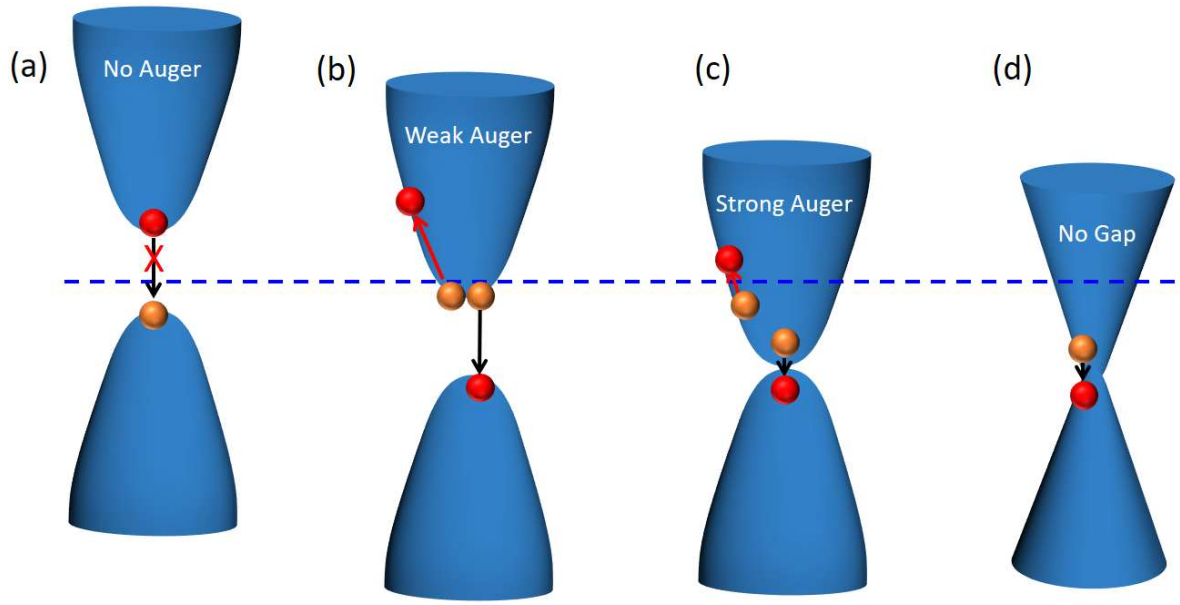

Figure 6.6: Sketch of the relaxation dynamics involving hot electrons (red spheres), holes (yellow spheres), and auger recombination (black arrows) for a series of electron doped BP. The dashed blue line indicates Fermi level.

We sketch in Fig. 6.6 our interpretation of the data. The appearance of a two dimensional electron gas dominates the hot carrier dynamics in the thermalization and recombination processes. Indeed, the significant electron-electron scattering in the moderate and strong electrons doped BP leads to impact ionization and auger processes. As a consequence of these new scattering channels, the thermalization time becomes faster as function of doping. For the recombination process of pristine BP, the presence of the gap requires that hot electrons and hot holes recombine via defects. This slower process lead to a bottleneck for the decay process, as shown in Fig. 6.6 (a). However, in moderate electron doped BP shown in Fig. 6.6 (b-c), part of the conduction band states become occupied. This filling opens a recombination channel in which the phonon emission is assisted by auger scattering in the conduction band. As a consequence, the recombination of hot carriers is more efficient in the electron doped BP (Fig. 6.6 (c)) compared to in the pristine BP (Fig. 6.6 (b)). In strong electron doped BP where the gap is closed as shown in Fig. 6.6 (d), hot electrons can even cascade down continuously without any constrain imposed by phonons scattering. Our findings are in consistent with the reports of doping dependent hot carrier dynamics shown in monolayer and bilayer graphene [6] but can more systematically explain the underlying physical processes. This preliminary analysis is based on the dynamics of hot electrons with positive excess energy (energy larger than zero). Clearly, it should be corroborated by the temporal evolution of the signal below the

chemical potential. Indeed, the hot hole signal that is observed at the valence band maximum should also follow a recombination time similar to the one of hot electrons in the conduction band. The analysis becomes more complex because the differential signal below the chemical potential does not contain only the contribution of hot hole's but also the one of stark broadening and stark shift. We are nonetheless confident, that we will soon find a reliable and effective procedure to disentangle the different components. Finally, we are in discussion with close collaborators who could perform ab-initio calculation that may explain our results based on the calculated density of electronic states and on the matrix elements of the electron-phonon scattering.

6.3 Conclusions

Here, we performed TR-ARPES experiment in BP as function of electron doping and directly observe the evolution of hot carrier dynamics. The thermalization time drops by a factor of 10 at high doping level, due to the opening of new scattering channels involving electron-electron interaction. Similar to the thermalization dynamics, also the recombination time of hot carriers decreases drastically when the surface becomes metallic. This result is ascribed to the appearance of recombination processes where phonon emission comes together with auger scattering processes. In the strong electron doped BP, the gap is fully collapsed and an even faster timescale of hot carrier's recombination is observed. This preliminary work on black phosphorous provides new insights on the hot carrier's dynamics in inversion layers with variable gap size and will be of guidance to understand the microscopic scattering mechanisms in doped semiconductor in general.

References

[1] Zhesheng Chen, Jingwei Dong, Christine Giorgetti, Evangelos Papalazarou, Marino Marsi, Zailan Zhang, Bingbing Tian, Qingwei Ma, Yingchun Cheng, Jean-Pascal Rueff, Armina Taleb-Ibrahimi, Luca Perfetti. Spectroscopy of buried states in black phosphorus with surface doping. *2D Materials*. **7**, 3 (2020).

[2] Tagliabue, G., DuChene, J.S., Abdellah, M. et al. Ultrafast hot-hole injection modifies hot-electron dynamics in Au/p-GaN heterostructures. *Nat. Mater*. **19**, 1312–1318 (2020).

[3] Brongersma, M., Halas, N. & Nordlander, P. Plasmon-induced hot carrier science and technology. *Nature Nanotech* **10**, 25–34 (2015).

[4] Kadi, F., Winzer, T., Knorr, A. et al. Impact of doping on the carrier dynamics in graphene. *Sci Rep* **5**, 16841 (2015).

[5] Esmaielpour, H., Dorman, K.R., Ferry, D.K. et al. Exploiting intervalley scattering to harness hot carriers in III–V solar cells. *Nat Energy* **5**, 336–343 (2020).

[6] Ulstrup, S. et al. Ultrafast Dynamics of Massive Dirac Fermions in Bilayer Graphene. *Phys. Rev. Lett*. **112**, 257401–5 (2014).

[7] Johannsen, J. C. et al. Tunable carrier multiplication and cooling in graphene. *Nano Letters* **15**, 326 (2014).

[8] Sun-Woo Kim, Hyun Jung, Hyun-Jung Kim, Jin-Ho Choi, Su-Huai Wei, and Jun-Hyung Cho. Microscopic mechanism of the tunable band gap in potassium-doped few-layer black phosphorus. *Phys. Rev. B* **96**, 075416 (2017).

[9] J. Kim, M. Huh, S.W. Jung, S.H. Ryu, Y. Sohn, K.S. Kim, Electronic band structure of surface-doped black phosphorus. *J. Electron Spectrosc* **219** 86–91 (2017).

Chapter 7 Ultrafast dynamics of hot carriers in a quasi-two-dimensional electron gas on InSe

7.1 Motivation

Indium selenide (InSe) displays many interesting characteristics. The thickness of InSe crystals can be decreased to a few layers from a bulk and encapsulated in hexagonal boron nitride (hBN) [1]. Via these methods, researchers demonstrated two main aspects which make InSe worth to investigation. First, the mobility of charge carriers is extremely high and it rivals with the value observed in graphene [2,3]. Second, the bandgap value of bulk InSe, which is 1.26 eV, is ideal for optoelectronic applications. Finally, InSe crystal is one of the best polar materials to fabricate field effect transistors [4].

Here we choose ε-InSe crystal as a polar material where to grow a two Dimensional Electron Gas (2DEG) [5-8]. A two-dimensional electron gas is a scientific model in solid-state physics. As shown in Fig. 7.1, an electron gas is free to move in two dimensions but tightly confined in the third one. And this tight confinement leads to quantized energy levels for motion in the third direction. 2DEGs have recently been employed in several research fields as computing [9], metrology [10], spin to charge conversion [11] and optoelectronics [12]. The 2DEGs can develop at the interfaces of polar materials either spontaneously or via electrostatic gating. At these interfaces, the conducting carriers can interact with the Longitudinal Optical (LO) phonons by Fröhlich coupling [13] This interaction has a long range and can limit the electron mobility. Indeed, phonon emission reduces the mean free path, whereas the virtual phonons lead to the formation of a quasi-particle with enhanced effective mass and known as polaron. Figure 7.2 depicts the origin of the Fröhlich interaction. A conduction electron in an ionic crystal or a polar semiconductor repels the negative ions and attracts the positive ions. A self-induced potential arises, which acts back on the electron and modifies its physical properties. Even if the electronic screening drastically reduces the strength of the Fröhlich interaction [14], the 2DEG can still suffer of Coulomb scattering with dipoles of the surrounding medium, thereby reducing the mobility of few layer devices [15, 16]. Up to now, the remote LO coupling has been of concern in gate insulators with a high dielectric constant. These new nanotechnologies make use of field effect transistors based on high-κ gates, they are partially replacing silicon dioxide [5] and have been already integrated in aggressively downscaled CMOS.

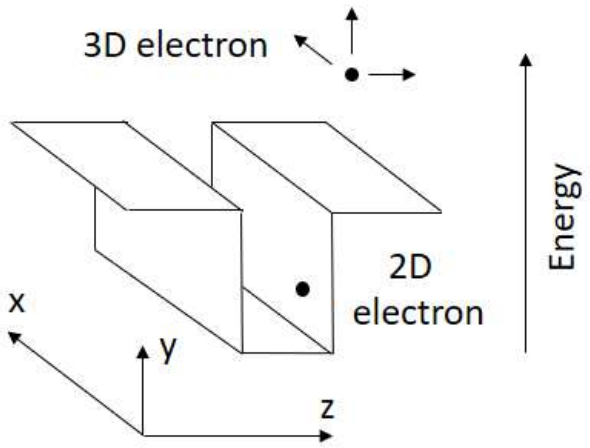

Figure 7.1: Electrons confined in a quantum well.

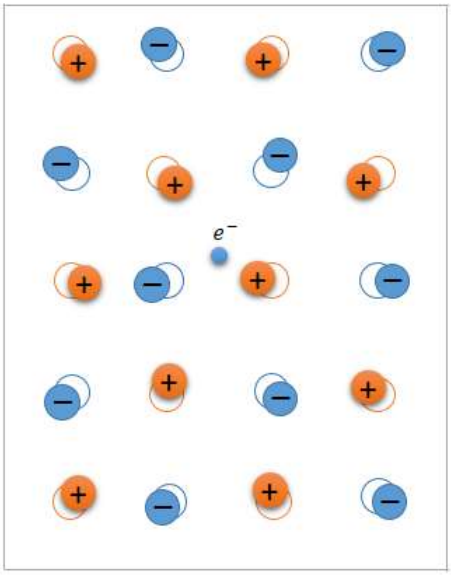

Figure 7.2: Artist view of a polaron. A conduction electron in an ionic crystal or a polar semiconductor repels the negative ions and attracts the positive ions. A self-induced potential arises, which acts back on the electron and modifies its physical properties.

7.2 Concurrent work

Several researchers explored the Fröhlich interaction of a two dimensional electron gas with a LO mode of oxides as $SrTiO_3$ [17] and TiO_2 [18]. Z. Wang and his collaborators revealed that shake-off replicas of the quasi-particle peak disappear above a critical density of electrons in accumulation layer. The crossover from long-range to screened interaction takes place at the electron density of ~ 4 – 8 x 10^{13} 1/cm^2 in $SrTiO^3$ (~ 2 x 10^{12} 1/cm^2 in InSe, shown in the following results and discussion). S. Moser and co-workers also found a similar behavior in the case in TiO_2. In these oxides the polar coupling is in

the wide antiadiabatic regime. Indeed, Z. Wang and his collaborators showed that the LO phonon energy is $\hbar\Omega \cong 100$ meV and the 2DEG effective mass is $m_{eff} \cong m_e$ in $SrTiO_3$. Since the screening becomes most effective in the adiabatic regime (i.e. $\hbar\Omega/E_F < 1$, E_F is the Fermi energy of the 2DEG), the crossover from unscreened to screened interaction occurs at high critical density in the case of $SrTiO_3$.

In addition, the electron- phonon coupling between graphene and a polar substrate was investigated by Chen and his co-workers [15] and, independently, by Fratini [19]. Simulations of transport properties predicted that remote coupling limits the mobility of charge carriers in the two dimensional semimetal [19]. Indeed, the transport measurements of graphene [15] on SiO_2 indicate that scattering with interface phonons has high impact on the transport properties of the electrons.

7.3 Methods

In this work we uncover the relevance of remote phonon coupling by analyzing in real time the cooling rate of a 2DEG with increasing carrier's concentration. The 2DEG with variable carrier density is obtained by evaporating Cs atoms on the surface of InSe at low temperature and in ultrahigh vacuum chamber. This doping method simulates with good accuracy the electrostatic gating and can be easily implemented in our experiment. We make use of Time and Angle Resolved Photoelectron Spectroscopy (TrARPES) [20] to directly monitor the electronic state and distribution function of hot electrons in the accumulation layer of a single crystal of ε-InSe. Our approach is well suited because: i) the probing depth compared to the localization length of the 2DEG [21]; ii) it can reveal if excited electrons are in extended bulk or in confined 2D states [22] via the momentum selectivity; iii) the electronic distribution discriminates between the semiconducting and metallic regime of hot carriers; iv) the electronic cooling is slower than the typical pulse duration of mode-locked laser pulses [20, 23-25].

To better understand the structure of electronic states in ε-InSe, our collaborators Cristine Giorgetti and Jelena Sjakste performed ab-initio simulations. The calculations for the band structure, vibrational properties and electron-phonon coupling in three dimentional ε-polytype of InSe were performed with QUANTUM ESPRESSO package [26], the three-dimentional single crystals of ε-InSe (space group D_{3h}^1 in Schoenflies notation) has been build using the lattice parameters from Ref. 27 (a = 3.9553 Å, d_{MM} = 2.741 Å, d_{XX} = 5.298 Å, c = 16.64 Å) and AB stacking. In these studies, there are many direct applications for the package. For examples, in order to describe the Fröhlich coupling in ε-InSe, we use

Vogl's model [28] together with *ab initio* parameters. To model the Fröhlich interaction in 2D InSe, we adopt the model and findings of Ref. 29. And we use the Thomas-Fermi approach to model the screening in 3D case. Conversely, for the case of 2D electron gas in dielectric medium, the result of Thomas-Fermi approach to the screening was obtained in Ref. 30.

The ε-InSe samples used in our experiments have been grown by the Bridgmann method from a nonstoichiometric melt [31]. As displayed in Fig. 7.3(a), Fig. 7.3(b) and Fig. 7.3(c), separately, the crystallographic structure (top and side views, respectively, left and right), and the calculated bulk band structure projected on the surface plane, along the $\overline{\Gamma}$ -$\overline{M}$ of the hexagonal Brillouin zone (BZ) (see inset), the bulk and surface Brillouin zone of ε-InSe can be seen clearly, and in Fig. 7.3(b), the red dashed and orange dotted point out the extension of the projected first conduction band. As illustrated in the Fig. 7.3(c), the *M-L* direction of the bulk BZ is projected on the $\overline{M}$ point of surface BZ.

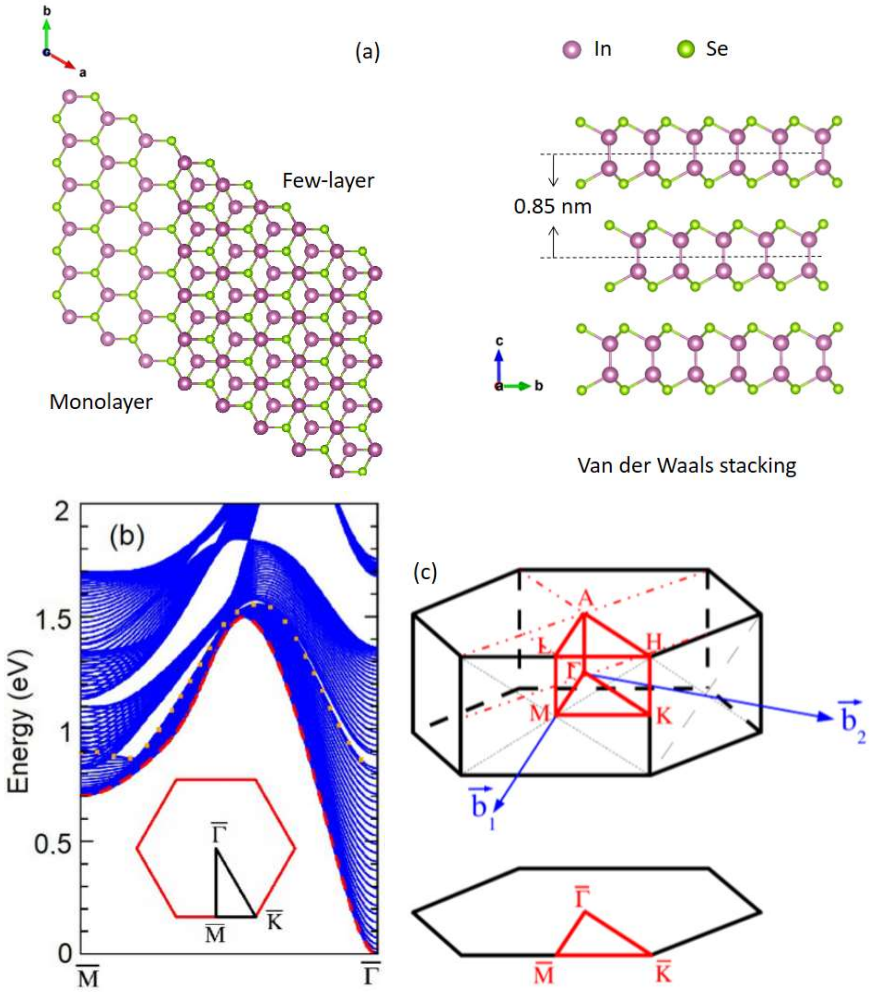

Figure 7.3: (a) Crystal structure of ε-InSe. (b) Projected band structure along the high-symmetry direction $\overline{\Gamma}$ -$\overline{M}$. (c) Bulk and surface Brillouin zone of ε-InSe.

In order to gain further information on the band structure of our ε-InSe samples, the photoluminescence spectroscopy [1] is exhibited in Fig. 7.4, through the figure, we know that the ε-InSe crystal has a direct band gap of 1.26 eV. Upon decreasing of the thickness of layered ε-InSe, the band gap increases and can be changed from direct to indirect one when reducing the thickness of InSe to a monolayer. Moreover, ultraviolet photoemission spectra exhibit that the ε-InSe sample is naturally *n* doped [4].

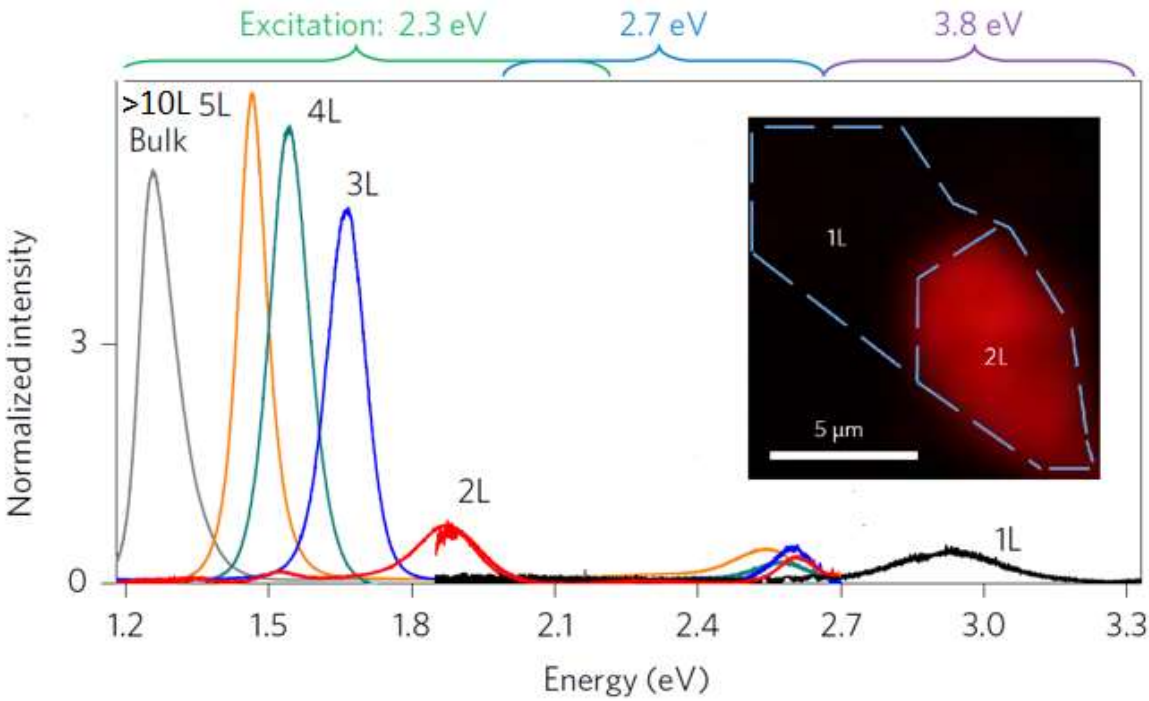

Figure 7.4: Photoluminescence of layered InSe crystal. Inset: map of PL intensity integrated over the spectral range 1.85-2.7 eV for excitation at 2.7 eV. The blue contours indicate the position of mono- and bilayer regions. The black to red color scale indicates the intensity variations from zero to maximum.

7.4 Results and discussion

First, we focus our effort on understanding the electrons dynamics on the pristine surface of InSe. Figure 7.5 shows the photoelectron intensity maps acquired along the $\bar{\Gamma}$ - $\bar{M}$ direction at different delay times t between the pump pulse centered at 1.5 eV and the probe pulse centered at 6.3 eV. In Fig. 7.5(a), the image collected 1 ps before the arrival of the pump beam is representative of the system in equilibrium conditions. According to the nominal n doping, few the electrons are visible at the conduction band minimum. Two image-potential states below $E_{\bar{\Gamma}}$ are excited by the 6.3 eV beam and are detected, at negative t, by the 1.5 eV pulse (Figs. 7.5(b) and 7.5(c)). Due to the short life time, the

lowest image-potential state is clearly visible only in the intensity map of Fig. 7.5(c). This map has been acquired at a nominal value of zero delay and can be viewed as a snapshot of the primary excitations. We remark in Fig. 7.5(c) that the 1.5 eV pulse populates the conduction band up to E = ω−Δ =0.25 eV where Δ is the bandgap of InSe. The internal thermalization of such hot carriers proceeds faster than the cooling, probably because of an additional contribution of electron-electron scattering.

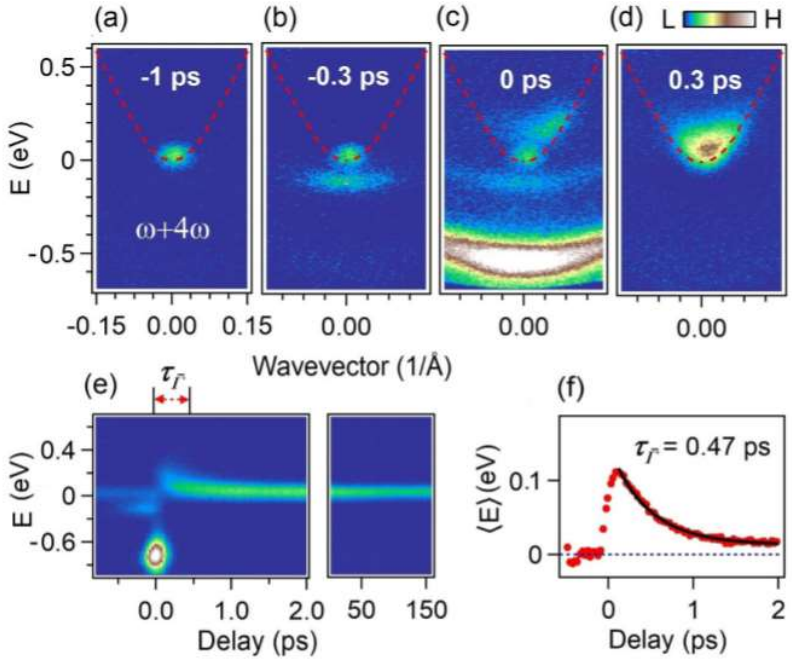

Figure 7.5: The 2PPE data of this figure is generated by ω =1.56 eV and 4ω =6.24 eV photons. (a)–(d) Photoelectron intensity maps acquired along the $\bar{\Gamma}$ - $\bar{M}$ direction and plotted as a function of excess energy for different delay times. The red dashed line is the conduction band dispersion. (e) Dynamics of photoelectron intensity integrated in the wave-vector interval [−0.1,0.1] $Å^{-1}$. (f) Average excess energy of the electrons in the conduction band as a function of pump-probe delay. The solid line is an exponential fit with decay time $\tau_{\bar{\Gamma}}$ =0.47ps.

Fig. 7.5(e) shows the photoelectron intensity I(E,t) integrated in the wave-vector window [−0.1,0.1] $Å^{-1}$ and plotted as a function of pump-probe delay. The average excess energy <E> of the electrons in the conduction band is obtained by evaluating the integral $\int E\, I(E,t)dE \,/\, \int I(E,t)dE$ in the interval $E \in$[0, 0.5] eV. As shown by Fig. 7.5(f), the <E> has an initial value of $\langle E \rangle_0$ =0.12 eV and it follows an exponential decay with time constant $\tau_{\bar{\Gamma}}$ =0.47±0.2 ps. This timescale elucidates the main relaxation mechanism of hot carriers in the $\bar{\Gamma}$ valley. We recall that a long-range Fröhlich interaction diverges in a material with three-dimensional periodicity. Therefore, the polar optical coupling becomes

the dominant electron-phonon scattering channel for small momentum transfer [32]. In addition, through the theoretical calculation, we estimate the energy dissipation rate $\lambda = d\langle E\rangle/dt$ between 0.21 and 0.24 eV/ps at 125 K. Due to the long-range nature of the Fröhlich coupling, the phonon emission is weakly sensitive to the variation of the electronic density of states. Therefore, λ is almost independent on $\langle E\rangle$ as long as the excess energy is sufficiently larger than the phonon frequency. According to our theoretical estimate, hot carriers with an initial value $\langle E\rangle_0 = 0.12$ eV require a characteristic time $\langle E\rangle_0 / \lambda = 0.57$ ps to approach the asymptotic level. The reasonably good agreement between $\langle E\rangle_0/\lambda$ and the experimental $\tau_{\bar{\Gamma}}$ confirms that our analysis provides an accurate description of the observed cooling.

As next step, we explore the ultrafast electron dynamics in 2DEGs generated by Cs doping on the InSe surface. Since the bulk crystal of InSe is naturally n-doped, a downward band bending of roughly 150 meV takes place at the surface. As shown by Figs. 7.6, the chemical potential of a freshly cleaved surface lies 10 meV above the conduction band minimum. We estimate the position of the chemical potential in the bulk of the crystal from the Surface PhotoVoltage (SPV) effect. Figure 7.6(a), shows that the kinetic energy of surface chemical potential displays an upward shift of ~ 150 meV upon photoexcitation. This steady SPV does not change by increasing pump fluence, indicating that the pump beam brings the sample in flat band condition. Since the chemical potential of the pristine surface is very near to the conduction band minimum (the estimated filling E_F is 10 meV), the downward band bending is roughly 150 meV. As displayed in Fig. 7.6(b), the chemical potential in the bulk of the sample potential is therefore located 150 meV below the conduction band minimum. Note that SPV and band bending are independent on Cs doping. This finding is not in contrast with the fact that Cs doping induces a deep confining potential within ~ 5 nanometers from the surface. The corresponding band bending diagram and confining potential are sketched in Fig. 7.6(c). It is important to make a clear distinction between the band bending that occurs in a depletion region of roughly 100 nanometers and the confining 2DEG potential that develops within few atomic layers from the surface [33].

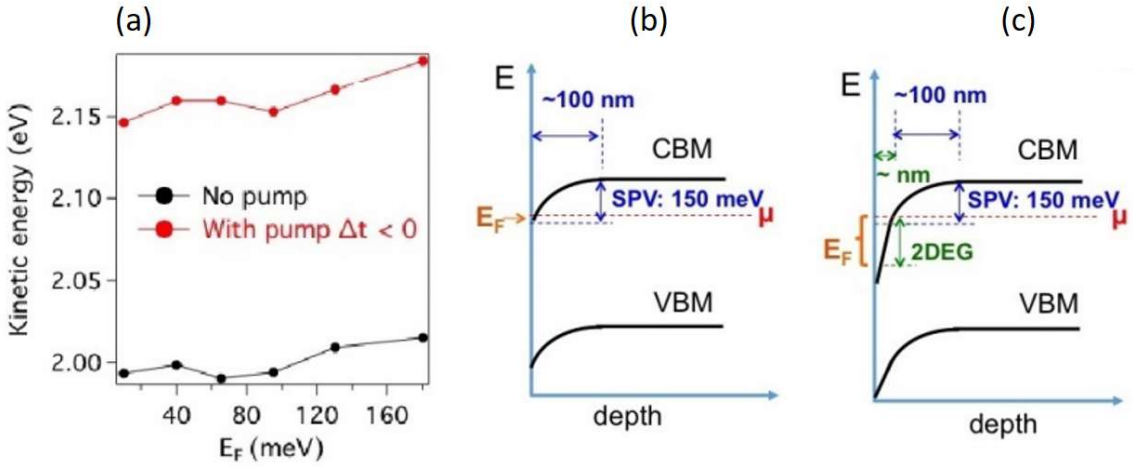

Figure 7.6: (a) The kinetic energy of the surface chemical potential without pump (black marks) and with pump at negative delay (red marks). (b) Band bending diagram in pristine InSe. (c) Band bending diagram in InSe after Cs deposition.

Accumulation layers with different charge concentration can be obtained via subsequent evaporation doses of Cs on the surface of InSe. The Fermi Energy E_F of the electrons can be varied from 10 meV up to 200 meV by increasing the density of the absorbed alkali atoms (see Fig. 7.7(a)). These 2D states penetrate the interface over a distance of several nanometers but are highly dispersing in the surface plane. At the highest doping level an additional feature can be observed near zero wavevector and zero energy. These states could be the bottom of the underlying 3D conduction band or the second sub-band of the quasi-2DEG. In one case as in the other, the occurrence of an extra band is in agreement with the 2D quantization of the electronic states in the confining potential. It is instructing to estimate the maximal carrier density ρ_M in the accumulation layer. The little effective mass of the 2DEG, which is 10 times smaller than the one of a free electron, leads to a carrier concentration ρ = 9×10^{12} 1/cm^2 for E_F = 200 meV. Such ρ value is comparable to the maximal doping level achieved via electrostatic gating [1]. At even higher alkali concentration the surface of InSe becomes unstable and the quasi-2DEG disappears [34]. Since InSe has a direct electronic gap of ~1.26 eV, after suddenly injecting hot carriers in the conduction band by photoexciting the sample via an ultrafast laser pulse centered at 1.55 eV, the excited carriers attain a maximal excess energy of 0.3 eV. The electron-electron interaction efficiently redistributes the energy density in the accumulation layer. Being near to the conduction band minimum of a polar material, the electrons will mainly relax their excess energy via emission of LO optical modes [35]. As displayed by Fig. 7.7(c), the electronic distribution at pump probe delay of 0.1 ps matches well a thermalized state with effective electronic temperature T_e. The only notable exception is observed on

the pristine surface (E_F = 10 meV), where the distribution near the conduction band minimum differs from the one expected from a thermal gas. We estimate the electronic temperature for each E_F by fitting the high energy tail of the excited electronic spectrum with a Fermi Dirac function that is also called Fermi function, which provides the probability of occupancy of energy levels by Fermions (Fermions are half-integer spin particles, which obey the Pauli exclusion principle). In addition, the average excess energy in the electron gas is obtained by calculating the integral, which is the same as the formula that is used to described the average excess energy in pristine InSe after photoexcitation (as shown above):

$$E_x(t) = \int E|I(E,t) - I(E,-)|dE \,/\, \int |I(E,t) - I(E,-)|dE\,, \qquad (7.1)$$

where $I(E,t)$ is the angle integrated spectrum at delay time t while $I(E,t)$ is the angle integrated spectrum at negative delay. The integration range is between -0.3 and 0.3 eV. Note that the excitation density after internal thermalization can be different than one initially injected by the pump pulse because of an imbalance between impact ionization and Auger processes.

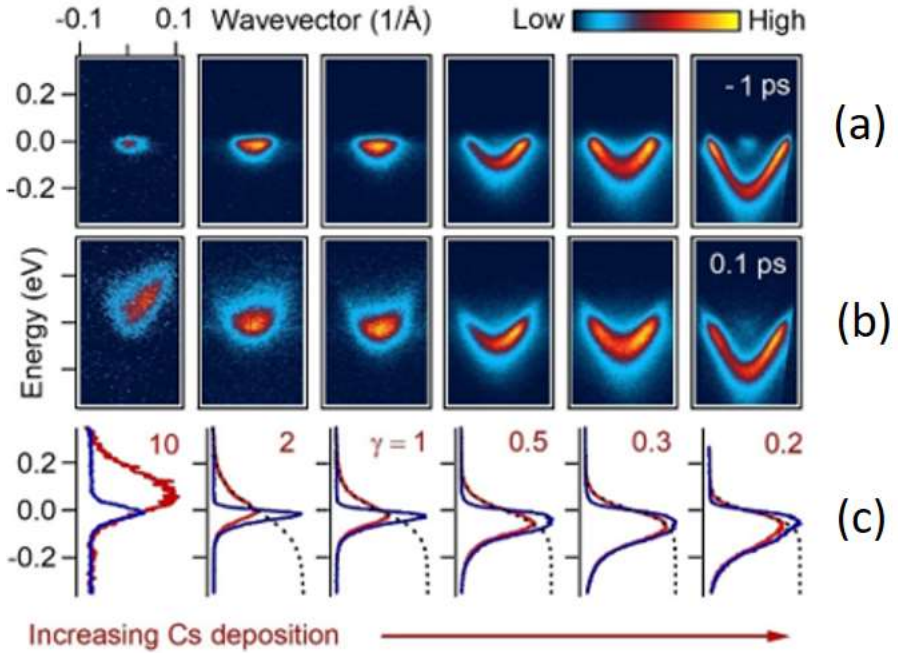

Figure 7.7: (a) Photoelectron intensity maps acquired at negative pump-probe delay. (b) Photoelectron intensity maps acquired at delay time of 0.1 ps. (c) Wavevector integrated intensity at negative delay time (blue curve) and 0.1 ps after photoexcitation (red curve). The black dashed curve is the estimated Fermi-Dirac distribution. We indicate with γ the ratio between the average excess energy Ex and the Fermi energy E_F. Here E_F is the energy distance between the bottom of the dispersing parabola and the chemical potential in the low temperature limit (zero of the energy axis). Panels of each line have been acquired for a given exposure to the Cs vapor. From left to right, the Fermi energy of the electron gas is E_F = 10,40,65,95,130,200 meV.

As illustrated in Fig. 7.8, the E_x at 0.1 ps scales as (1.3±0.1) k_bT_e within the entire doping range and decreases by 70% at high cesium concentration. Since the pump pulse always injects the same energy density, the drop is due to the energy redistribution between a fixed amount of photoexcited carriers and the increasing number of electrons in the accumulation layer. As a consequence, the parameter $\gamma = E_x/E_F$ spans from the semiconducting regime ($\gamma = 10$) to the metallic regime of a deeply degenerate quasi-2DEG ($\gamma = 0.2$). When the electronic density in accumulation level increases, three effects reduce the energy dissipation of the photoexicted gas: i) the metallic electrons efficiently screens the long range Fröhlich interaction between electrons and LO phonons, ii) the Fermi statistics hinders dissipation channels near to the chemical potential and, iii) the average excess energy of the electrons approaches the threshold value for an emission of LO phonon ($\hbar\Omega_{LO}$ = 24 meV).

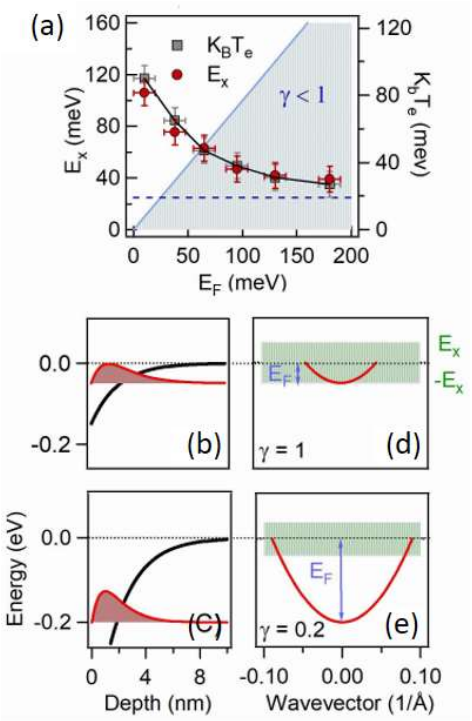

Figure 7.8: (a) Average excess energy (red circles) and electronic temperature (gray squares) as a function of Fermi energy. The shaded blue area indicates the region where the average excess energy of electrons becomes lower than the Fermi energy. The dashed blue line indicates the threshold electron energy for LO phonon emission. (b) Sketch of near surface potential leading to the accumulation layer as a function of energy (solid line) and local probability density (red dashed area) of the confined state at the bottom of the 2DEG dispersion as a function of distance from the surface. The choosen parameters are E_F = 50 meV and E_x = 50 meV. (c) Same as for the previous panel but with parameters E_F = 200 meV and E_x = 40 meV. (d) Sketch of the dispersion of quasi-2DEG for E_F = 50 meV and E_x = 50 meV. (e) Same as for the previous panel but with parameters E_F = 200 meV and E_x = 40 meV.

Besides, the surface doping also induces a dimensionality crossover of the hot carriers [36]. When E_F is small compared to E_x, the confining potential plays the role of a small perturbation. Therefore, hot electrons occupy bulk like states with 3D character. Conversely, the 2D confinement becomes effective once the E_F is larger than the average excess energy. At E_F > 100 meV hot electrons with low E_x accumulate in wavefunctions that extends only few nanometers in the bulk. Although an effective dimensionality of hot electrons is not sharply defined, we remark that $\gamma = E_x/E_F$ is a meaningful measure of the 3D-2D crossover.

Furthermore, the full dynamics of hot electrons elucidate the evolution of cooling process at different doping levels. Fig. 7.9(a) shows the differential signal obtained by subtracting the map acquired at negative to the one acquired at positive values of the pump-probe delay. Blue and red colors stand for photoexcited electrons and holes in the electronic system, respectively. These panels offer a visual guide of the electronic cooling for three indicative densities (E_F = 10,40,130 meV). A qualitative analysis of the differential intensity maps provides clear evidence of the dimensionality crossover. Note that excited electrons are distributed in a broad area of reciprocal space when E_F = 10 meV. This signal originates from many 3D states with different values of the perpendicular wavevector k_z. Since these 3D states disperse along the z axis, the excited electrons cover part of the projected band structure. In contrast, with the increasing of Cs doping, the differential intensity is concentrated along a nearly free electron parabola that has no dispersion in the z direction when E_F = 130 meV. From this map, we deduce that hot electrons become confined in the high doping regime. Figure 7.9(b) plots the temporal evolution of the excess energy normalized to its maximal value. Initially, the excited electrons experience a subpicosecond relaxation due to emission of LO phonon with small momentum transfer. After 1-2 ps, such subset of phonon modes enters in equilibrium with hot electrons. The subsequent dynamics is dictated by anharmonic decay of the hot optical phonons in the lattice modes of lower energy. Here we are interested only in the relaxation at early delay, namely when LO phonons are still near to equilibrium conditions. As shown by Fig. 7.9 (b), the initial cooling time τ becomes twice slower at high carrier concentration. Measurements on two different cleaves confirm that τ is roughly 0.4 ps in the pristine surface, while it saturates to 0.8 ps upon increasing the concentration of absorbed Cs as displayed in Fig. 7.9(c).

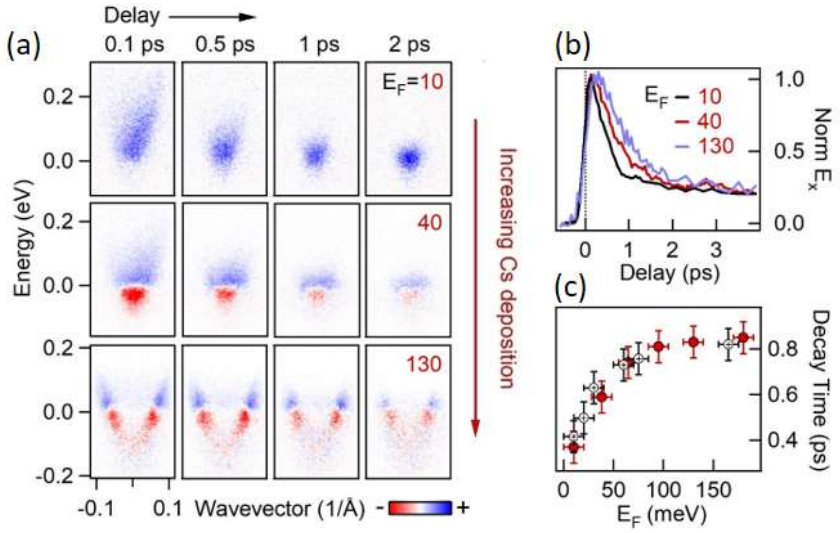

Figure 7.9: (a) Differential intensity maps obtained by subtracting the photoelectron intensity at negative delay from the photoelectron intensity at positive delay. The panels from left to right display data acquired at increasing delay time after photoexcitation. Top, middle and bottom columns correspond to an electron gas with Fermi energy E_F = 10,40,130 meV. (b) Temporal evolution of the average excess energy E_x in the electron gas with different Fermi Energy. The curves have been normalized to the maximal E_x value for better comparison. (c) Initial decay time of average excess energy versus the Fermi energy. Filled and open symbols indicate the results of two independent set of measurements.

The cooling rate η of the electronic system is estimated as the average excess energy at 0.1 ps divided by cooling time τ. Fig. 7.10(a) shows that such rate decreases by nearly one order of magnitude when moving from the semiconducting to the metallic regime. Since at low doping levels the hot electrons show 3D behavior, a less restrictive confinement could, in principle, open transport channels into the bulk conduction band. Transport effects can contribute to the energy relaxation of the electrons when the diffusion length $L = \sqrt{Dt}$ covered during the relaxation time t is larger than the depth d of the excitation profile [24]. An upper bound of the out-of-plane-diffusion constant D can be estimated from the in-plane mobility [1] μ_e (the out of-plane being lower) and the Einstein relation $D = \mu_e k_b T_e/e$. With $\mu_e < 1000$ cm^2/V/s, $k_b T_e < 100$ meV and $t < 1$ ps we obtain $L < 0.1\mu$m. Since our pump pulse excites electrons just above the bandgap, the penetration depth d of the pump pulse is particularly long. From the absorption coefficient [37] at 1.55 eV, we find $d = 10\mu$m. Being L two orders of magnitude smaller than d, we conclude that diffusion effects can be safely ignored. In order to simulate the cooling rate, we calculated the phonon spectrum by density functional perturbation theory (DFPT) (see Fig. 7.10(b)). We identify the polar and the nonpolar branches for each direction in wavevector space.

Since the Γ valley is very narrow (effective mass of 0.1 electron mass) and there are no adjacent valleys, the energy and momentum conservation rules limits the phonon emission to wavevector transfer of q < 0.2 1/Å. In the 3D case, the unscreened scattering with polar optical phonons is long ranged in real space and diverges when the phonon wavevector q tends to zero [28]. As a consequence, due to the absence of intervalley scattering, we expect LO emission to be the largely dominant electron-phonon scattering mechanism. Indeed, the preeminence of Fröhlich scattering at low excess energies is a general property of polar semiconductors, such as for example GaAs [35]. To illustrate this point, we compare on Fig. 7.10(c) the strength of the electron-phonon matrix elements for all phonon modes of ε-InSe in the Γ−*M* direction. Our numerical results show that the coupling of the E' polar mode is in average more than 10 times larger than the one of the best coupled non-polar mode (the mode with A_1' symmetry). The contribution of the polar coupling to the energy relaxation rate scales as coupling matrix element squared, being at least 100 times larger than the A_1' non-polar one. With respect to the other nonpolar modes this ratio becomes even larger, so that the black curves in Fig. 7.10(c) collapse to values near to the ordinate axis. Fig. 7.10(c) also shows that the matrix elements of the polar E' mode nearly follow the q dependence predicted by the Vogl's model [28]. This result allows us to use Vogl's model for the electron-phonon coupling instead of the DFPT description.

We explore the doping effect on the Fröhlich interaction by calculating the cooling rate [38] as

$$\eta = (1-f(E_x - \hbar\Omega_{em}))\Gamma_{em}\Omega_{em} - (1-f(E_x + \hbar\Omega_{abs}))\Gamma_{abs}\Omega_{abs} \quad (7.2)$$

Here, f is Fermi-Dirac distribution function, which is mentioned as before, depends on the electronic temperature T_e and on the chemical potential, Γ_{em} and Γ_{abs} are the total probabilities for emission and absorption, while Ω_{em} and Ω_{abs} are effective LO phonon frequencies for emission and absorption (the detailed calculations are shown in the following section). For each value of the Fermi energy E_F, we extract the electronic temperature T_e from the experimental curve in Fig. 7.8 and derive the chemical potential μ on the base of a free electron model [39]. The values of Γ_{em} and Γ_{abs} strongly depend on the effective electron-phonon coupling strength of the polar modes. The non-polar modes would contribute to the cooling rate with an extra term below 0.01 eV/ps and can be neglected with respect to the emission of LO optical phonons. We first consider the case of a 3D electron gas with unscreened Fröhlich interaction. As already shown by our previous work on the pristine surface (40), this approach provides an estimated value of the cooling rate that is in agreement with tr-ARPES experiments. Upon increasing the doping level, the available momentum transfer increase by a small amount. On the other hand, the drop

of excess energy combined to Fermi Dirac statistic generate a stronger Pauli blocking of the scattering channels. The effects of quantum electron statistic on excitons has been evinced by pioneering experiments on GaAs Quantum Wells (23). In our case, the Pauli blocking alone would explain the moderate decrease of calculated η for $\gamma \cong 1$. Nonetheless, this unscreened coupling badly overestimates the experimental behavior even at moderate carriers concentration that is demonstrated as the red dotted line in Fig. 7.10(a).

To reproduce the experimental data, we consider a 3D model of the Fröhlich interaction [28] with Thomas-Fermi screening (a theoretical approach to calculate the effects of electric field screening by electrons in a solid). We expect these simulations to be accurate for the regime $\gamma > 1$, namely when hot electrons retain their 3D character. Amazingly, the black line in Fig. 7.10(a) shows that the screened 3D interaction matches well the experimental data even in the case of a quasi-2DEG. This result needs to be carefully addressed, since a dimensionality crossover towards 2D states is observed in photoelectron intensity maps with $\gamma < 1$. In this limit, a 3D treatment of the electronic degrees of freedom is clearly non justified. In order to gain more insights, we compute the η expected in a strictly two dimensional system, with 2D fröhlich coupling [29] and 2D dielectric screening [30]. Remark that such model assumes that all particles and interactions are fully constrained in a plane. Therefore, it differs profoundly from the real physical case in which a metallic 2D slab has a three dimensional coupling with a surrounding dielectric. The perfect confinement of the strictly 2D model does cut off the divergence of the polar interaction at small wavevector (the details are displayed in the below section). Moreover, the electron-hole excitations that are responsible for the screening response acquire a higher density in the phase space (consider that in a strictly 1D system the collective excitations become so strong that even the Fermi liquid picture breaks down). Such an increase of phase space for electron-phonon scattering has strong effects, so that the η of a strictly 2D model drops dramatically already a small doping level. It is clear from the dashed blue line of Fig. 7.10(a) that such model grossly underestimates the experimental cooling rate. The difference between the 2D model and experimental data is ascribed to a remote coupling between the quasi-2DEG and 3D phonons. This interaction could arise from an energy transfer mediated by surface plasmons-polaritons or any other channel that couples the confined electrons with LO modes that are not strictly two dimensional. An accurate simulation of such remote interaction would be a challenging task which is beyond the scope of the present work. However, Fig. 7.10(a) shows that a

3D model with Thomas Fermi screening already reproduces remarkably well the experimental data.

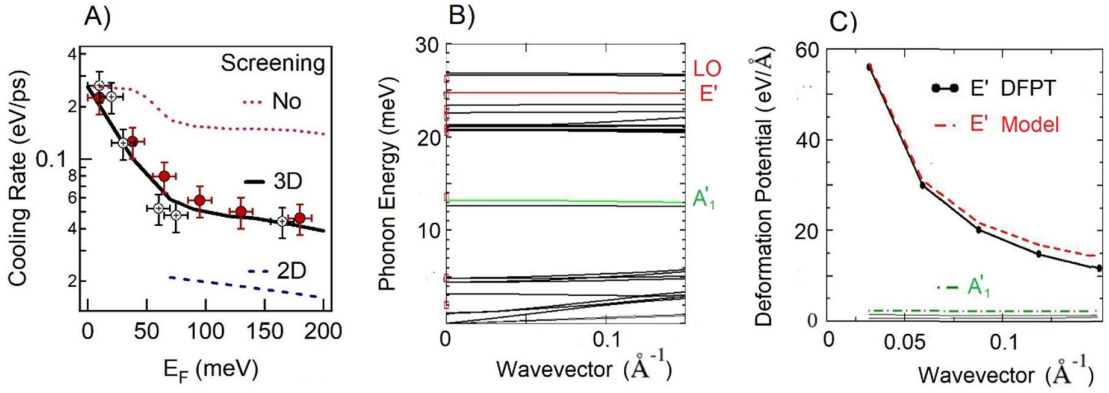

Figure 7.10: (a) Electronic cooling rate η as a function of Fermi energy. Filled and open symbols represent data from two independent set of measurements. The black solid, dashed blue and dotted red curves are the cooling rates calculated by an ab-initio model with 3D, 2D and no screening of the Fröhlich interaction, respectively. (b) Calculated phonon dispersion of ε-InSe in Γ−M direction of the Brillouin zone. Polar optical mode E' is shown in red, while the acoustical A_1' mode is shown in green. Red squares at q = 0 stand for experimental from Ref.41. (c) Calculated electron-phonon deformation potentials as a function of the phonon wavevector q along the Γ−M direction. The initial electronic state is in the conduction band at k = (0,0.11,0)2π/a. For the polar mode, both the results of the DFPT (Black circles) and Vogl model (red dotted line) are shown.

7.5 Theoretical calculations

In this part, we describe the technical details of the ab initio and model calculations which were performed in order to describe the electronic structure and vibrational properties of ***ε***-InSe, as well as the models used to estimate the electron-phonon scattering times on the basis of *ab* initio results, and to take into account the effect of the screening in 3D and 2D material.

Fröhlich interaction model in 3D *ε*-InSe

InSe is a polar semiconductor. Inside the narrow Γ valley below 0.7 eV excess energy (next $\bar{M}$ valley threshold), and in contrast with higher excess energies, the Fröhlich interaction between electrons and polar optical phonons is expected to be the dominant energy relaxation mechanism [35]. Indeed, in Ref. 40 we have shown that the energy relaxation rate due to coupling of electrons to polar optical phonons explains the experimentally measured energy relaxation rate of electrons extited in Γ valley of ***ε***-InSe at energies below that of $\bar{M}$ valley threshold. In this work, Jelena used Vogl's model [28] in order to describe the Fröhlich coupling in ***ε***-InSe, together with ab initio parameters. The

matrix element for Fröhlich electron-phonon interaction, which depends on the phonon momentum q, reads:

$$|g_{fr}^{3D}(q)| = (4\pi e^2/(V\epsilon_{bulk}|q|)) \sum_s \sum_{\lambda'} \frac{q_{\lambda'}}{|q|} Z_{\lambda'\lambda s}\, e_\lambda^s(q)/\sqrt{2M_s\omega_q} \quad (7.3)$$

In Eq. (7.3), ***e*** is electronic charge, *V* is unit cell volume, $Z_{\lambda'\lambda s}$ is the Born effective charges tensor for atom ***s***, and λ, λ' denote the cartesian components. $e_\lambda^s(q)$ is the phonon eigenvector which describes atomic displacements associated with a particular mode, ϵ_{bulk} is the bulk dielectric tensor, M_s are atomic masses [28]. As it was already shown before for GaAs for example [32], Fröhlich model reproduces very well the small-q behaviour of the electron-phonon matrix elements for polar optical phonons calculated within DFPT. We have checked that this is also the case for ***ε***-InSe.

Fröhlich interaction in 2D InSe

We use the model and findings of Ref. 29 to model the Fröhlich interaction in 2D InSe. Indeed, it was shown in Ref. 29 that for the LO phonon with in-plane wave vector q_p, the Fröhlich matrix element in 2D material can be described as:

$$|g_{fr}^{3D}(q)| = C_z/(e_{eef}^0 + r_{eef}|q_p|) \quad (7.4)$$

where

$$C_z = (2\pi e^2/(A)) \times \sum_s \sum_{\lambda'} \frac{q_{\lambda'}}{|q_p|} Z_{\lambda'\lambda s}\, e_\lambda^s(q)/\sqrt{2M_s\omega_q} \quad (7.5)$$

where A is the area of the unit cell, and e_{eef}^0 and r_{eff} are the effective parameters related to the dielectric properties of the 2D material and surrounding media. In particular, is was shown in Ref. 29 that the in-plane matrix elements of Fröhlich interaction in 3D and 2D materials (dichalcogenides) were found to be of the same order of magnitude for the case $e_{eef}^0 \approx 1$ and $r_{eff} \approx \epsilon_{iso} t_{iso}/2$. where ϵ_{iso} can be taken equal to the in-plane component of ϵ_{bulk} and t_{iso} is close to the interlayer distance of 3D material c. Moreover, the in-plane effective charges and phonon frequencies for 2D dichalcogenide studied in [29] were found to be very close to the corresponding in-plane bulk values. The model of Eq. (7.4) was shown in [29] to reproduce well the an initio results for the electron-phonon matrix elements in 2D materials. Based on the findings of [29], in this work, Jelena modelised the Fröhlich interaction in our 2D limiting case using the equation 7.3 with bulk in-plane ab initio

parameters for the effective charges and phonon frequencies, and take e^0_{eef} = 1 and $r_{eff} \approx \epsilon_{iso} t_{iso}/2$ where $\epsilon_{iso} = \epsilon_{bulk}$ and $t_{iso} = c$.

On upper panels of Fig. 7.11, we show the behaviour of 3D and 2D Fröhlich matrix elements (deformation potentials) for **q** in *y* direction in Brillouin zone (black curves), calculated in this work with models of Eqs. (7.3) and (7.4) and ab initio parameters. As one can see, the deformation potentials obtained are indeed very similar in 2D and 3D cases. As discussed in [29], the main difference resides in q →0 behaviour: while the 3D Fröhlich interaction matrix elements are divergent, the 2D ones grow rapidly when q →0 towards a constant value.

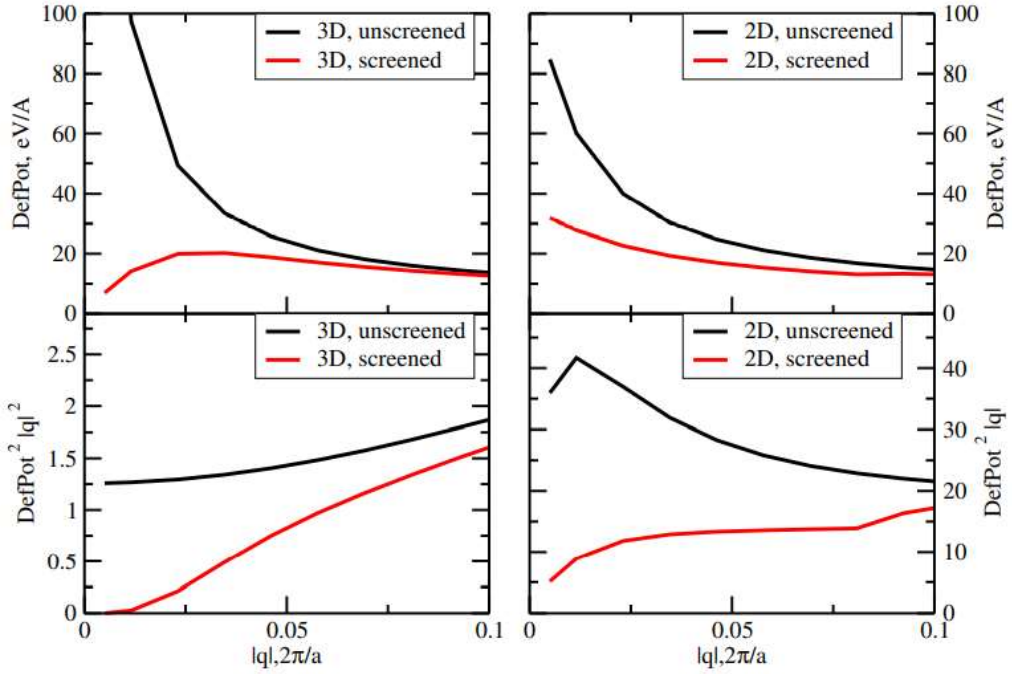

Figure 7.11: Upper pannels: the polar oplical (Fröhlich) electron-phonon coupling (deformation potential) as a function of phonon wavevector q along the y direction of the Brillouin zone, in 3D (left) and 2D (right) cases. Electron-phonon coupling is shown in the unscreened (black curves) and screened (red curves) cases. The screened case corresponds to E_F =175 meV. Lower panels: the effect of screening on the contribution to the scattering rate: the squared deformation potentials are multiplied by q^2 in 3D case and by q in 2D case.

Screening in 3D case

Jelena used the Thomas-Fermi approach to model the screening:

$$\epsilon^{scr}_{bulk} = \epsilon_{bulk}(1+(q_0^{3D})^2/q^2) \tag{7.6}$$

where

$$(q_0^{3D})^2 = k_F\,(4 * m_{eff}\, e^2)/(\epsilon_{bulk}\pi\hbar^2) \qquad (7.7)$$

Here, m_{eff} is the effective mass of the Γ valley of InSe, and k_F is the Fermi wave vector of the electron gas at the bottom of the Γ valley. k_F is determined numerically from the Fermi energy E_F which is measured experimentally as explained in the above text. In the case of 3D screening, we have checked by direct *ab initio* calculation of the electron phonon matrix elements that in the case of the presence of electron gas at the bottom of Γ valley, Fröhlich coupling at small *q*-vectors can be well reproduced by the model of Eq.(7.3) with ϵ_{bulk} replaced by ϵ_{bulk}^{scr}.

Screening in 2D case

In the case of 2D electron gas in dielectric medium, the result of Thomas-Fermi approach to the screening was obtained in Ref.30:

$$\epsilon_{iso}^{scr} = \epsilon_{iso}(1+(q_0^{2D})/q_p) \qquad q_p \le 2k_F \qquad (7.8)$$
$$\epsilon_{iso}^{scr} = \epsilon_{iso}(1+(q_0^{2D})/q_p(1-(1-(2k_F/q_p)^2)^{1/2})) \qquad q_p > 2k_F$$

where

$$q_0^{2D} = 2m_{eff}\, e^2/(\epsilon_{iso}\hbar^2) \qquad (7.9)$$

The effects of screening on the electron-phonon matrix elements are similar in 3D and 2D cases, as one can see on Fig. 7.11, where the screened Fröhlich coupling is shown on the upper panels (red curves) for the case of doping with E_F =175 meV, which is the highest doping considered experimentally in this work. As one can see, for E_F =175 meV, in both 3D and 2D cases the effect of doping starts to play a significant role at q<0.05 2π/a. The reduction rates of the deformation potentials (unscreened vs. screened) are similar in 2D and 3D. In both 2D and 3D cases, the screening is described by the parameters (q_0 in 3D case, k_F in 2D case) which are uniquely determined by the E_F, the Fermi energy of the electron gas created by doping. In Jelena's calculations E_F is treated as a parameter which can vary in the range between 0 and 200 meV, similar to the experimental one.

Scattering rates

For every initial electronic state $|\mathrm{n}, \mathbf{k}\rangle$, characterized by the band index *n* and wave vector **k**, the total probabilities (rates) for phonon emission and absorption Γ^{em} and Γ^{abs} as well as the effective phonon frequencies of emitted and absorbed phonons ω_{em} and ω_{abs} can be calculated using Fermi's Golden Rule, taking into account all processes allowed by energy and momentum conservation [35]. Similarly, the energy loss (gain) rates due to phonon emission (absorption), $\omega_{em}\Gamma^{em}$ ($\omega_{abs}\Gamma^{abs}$) are calculated as:

$$\omega_{em}\Gamma_{\mathrm{n,k}}^{em} = \frac{2\pi}{\hbar}\sum_{n'}\sum_{\nu}\frac{1}{L^d}\sum_{q\in BZ}\omega_q^{\nu}|\mathrm{g}_{n,k}^{\nu}(\mathrm{q})|^2\,\delta(\varepsilon_{n,k}-\varepsilon_{n',k+q}-\hbar\omega_q^{\nu})(N_q^{\nu}(T)+1) \qquad (7.11)$$

$$\omega_{abs}\Gamma^{abs}_{\mathrm{n,k}} = \frac{2\pi}{\hbar}\sum_{n'}\sum_{\nu}\frac{1}{L^d}\sum_{q\in BZ}\omega_q^{\nu}|\mathrm{g}^{\nu}_{n,k}(\mathrm{q})|^2\,\delta(\varepsilon_{n,k}-\varepsilon_{n',k+q}+\hbar\omega_q^{\nu})\,N_q^{\nu}(T) \qquad (7.12)$$

In Eqns. (7.11) and (7.12), $\varepsilon_{n,k}$ and $\varepsilon_{n',k+q}$ are the energies of the initial and final electronic states. ω_q^{ν} is the frequency of the phonon $|\nu,\mathbf{k}\rangle$. $g_{n,k}^{\nu}(q)$ is the electron-phonon matrix element, $N_q^{\nu}(T)$ is the temperature-dependent phonon distribution function: the Bose-Einstein distribution in our case. The Dirac delta functions $\delta(\varepsilon_{n,k}-\varepsilon_{n',k+q}-\hbar\omega_q^{\nu})$ and $\delta(\varepsilon_{n,k}-\varepsilon_{n',k+q}+\hbar\omega_q^{\nu})$ represent the energy- and momentum-conservation laws for respectively phonon emission and absorption. The sum (or integral) $\frac{1}{L^d}\sum_{q\in BZ}$ runs over all of the wave vectors in the Brillouin Zone (BZ), L^d being the normalization factor. In this work, Jelena calculates the electron-phonon matrix elements $g_{n,k}^{\nu}(q)$ using Fröhlich coupling model, as in our previous work [40]. The converged integrals for $\omega_{em}\Gamma^{em}$ and $\omega_{abs}\Gamma^{abs}$ require 100×100×100 points in **q**-space.

The energy loss (gain) rates due to phonon emission (absorption) are calculated for a given initial electronic state, characterized by the initial band number n, momentum k and energy $E_{n,k}$ and are subsequently averaged over several initial states which belong to the same energy isosurface. The electron-phonon scattering rates are then calculated as a function of energy of hot electrons with respect to the bottom of the conduction band, as in our previous work [40]. Note that in the case of the dominant Fröhlich coupling (and contrary to intervalley scattering case), the electron-phonon scattering rates does not depend on the energy of hot electrons with respect to the bottom of the conduction band. This has been shown in the case of undoped InSe [40] for excess energy up to the minimum of the $\bar{M}$ valley. Indeed, the available phase space has very little impact on the Fröhlich scattering rates because of the dominant role played by vanishing **q** vectors. The upper panels of Fig. 7.11 show that the effect of screening on the electron-phonon matrix elements is similar in 2D and 3D cases. Nonetheless, the effect of screening on the scattering rates is stronger in 2D than in 3D case. This finding arises from the change of phase space in reduced dimensionality, since the volume element scales as $\mathbf{q}^2 d\mathbf{q}$ in 3D while the area element scales as $\mathbf{q}d\mathbf{q}$ in 2D. The lower panels of Fig. 7.11 show the squared deformation potentials multiplied by $\mathbf{q}^2$ for the 3D case and multiplied by **q** in 2D case.

Electronic temperature and chemical potential

Except for the case of the pristine surface, the distributions of hot electrons of this work can be described by Fermi-Dirac distribution $f(E, T_e, \mu)$, where T_e is the electronic temperature and μ is the chemical potential. The electronic temperature of hot electrons T_e

for a given Fermi Energy E_F, is the unique input parameters that we extract from the experiment and that Jelena injects in the model calculations. For a given electronic temperature T_e and Fermi energy E_F, in the case of 2D electrons, μ can be calculated as follows [39]:

$$\mu^{2D} = E_F + k_b T_e \log(1-\exp(-(E_F/k_b T_e))) \quad (7.13)$$

In the case of 3D electrons, we use formulas for high-temperature and low-temperature limits of μ [39]:

$$\mu^{3D}_{\gamma>1} = k_b T_e(\log \nu + \nu/2^{3/2}) \quad (7.14)$$

$$\mu^{3D}_{\gamma<1} = E_F + \pi^2(k_b T_e)^2/12E_F - 18.0*\pi^4(k_b T_e)^4/1440\mathrm{E}_\mathrm{F}^3 \quad (7.15)$$

Where $\nu = \frac{4}{3\sqrt{\pi}}(E_F/k_b T)^{3/2}$. Here, $\gamma = T_e/E_F$.

In the case of $\gamma << 1$ (low-temperature limit), μ is close to E_F, both in 2D and 3D cases. In the case of $\gamma >> 1$ (high-temperature case) μ is large and negative.

Excess energy

Although the electronic distribution is fully characterized by the T_e at a given E_F, in the experimental part of our work, the excess energies of hot electron's E_x were also determined. Thus, we can compare the experimental and calculated E_x, checking the effect of the 2D and 3D models of the chemical potential, and substantiating the method of calculation of the energy relaxation rate described below.

In analogy with the Eq. (7.3) of the main paper that has been used to determine Ex experimentally, we calculate:

$$\mathrm{Ex} = \frac{\int(f(\varepsilon,T_e,\mu)-f_0(\varepsilon,T))\varepsilon d\varepsilon}{\int(f(\varepsilon,T_e,\mu)-f_0(\varepsilon,T))d\varepsilon} \quad (7.16)$$

Here, $f_0(E, T)$ is the Fermi-Dirac distribution at equilibrium temperature T = 40K. Note that the equation (7.16) can be considered as analogous to Eq. (7.3) of the main paper if we assume that the differential ARPES signal follows nearly the differential electronic occupation. Fig. 7.12 shows the values of Ex determined experimentally and the ones obtained via Eq. (7.16), with chemical potentials of Eqs. (7.13) or (14-15). In each case when the experimental distribution is thermal, the average excess energy of hot electrons calculated with Eq. (7.16) describes well the experimental E_x extracted by means of Eq. (7.3) in the main text. The employment of a 2D and 3D model for the evaluation of the chemical potential has little impact on the obtained excess energy.

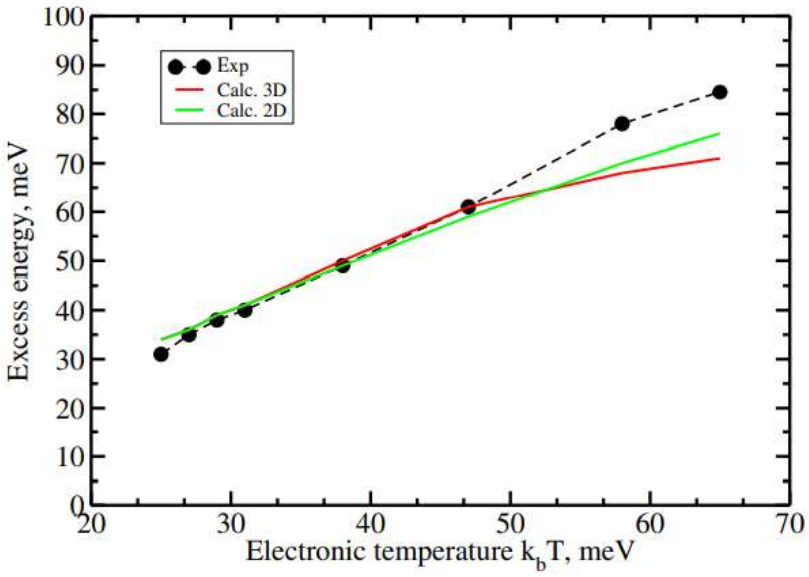

Figure 7.12: Excess energies of hot electrons determined experimentally in this work using Eq. (7.1) (black dots) and calculated using Eq. (7.16) and the chemical potentials of Eqs. (7.13) or (14-15): green and red curves.

Energy relaxation rate

Jelena then calculates the energy relaxation rate of hot electrons [38]:

$$\eta = \frac{d\langle E\rangle}{dt}(Ex) = \frac{\int (f(\varepsilon,T_e,\mu)-f_0(\varepsilon,T))[(1-f(\varepsilon-\hbar\omega_{em},T_e,\mu)\Gamma_{em}\omega_{em} - (1-f(\varepsilon+\hbar\omega_{abs},T_e,\mu)\Gamma_{abs}\omega_{abs}]d\varepsilon}{\int (f(\varepsilon,T_e,\mu)-f_0(\varepsilon,T))d\varepsilon} \quad (7.17)$$

Note that, as shown in [40], the Γ_{em} and Γ_{abs} of the Fröhlich coupling have negligible dependence on *E*. As a consequence, the Eq. (7.16) and the integral mean value theorem, can be employed to express energy relaxation rate of Eq. (7.18) via the simpler expression:

$$\eta = \frac{d\langle E\rangle}{dt}(Ex) = (1-f(E_x - \hbar\omega_{em}, T_e, \mu))\Gamma_{em}\,\omega_{em} - (1-f(E_x + \hbar\omega_{abs}, T_e, \mu))\Gamma_{abs}\,\omega_{abs} \quad (7.18)$$

Here, E_x is the excess energy of Eq. (7.16).

The Pauli blocking factors, $1 - f(E_x - \hbar\omega_{em})$ and $1 - f(E_x + \hbar\omega_{em})$, play an important role when $\gamma = T_e/E_F < 1$, reducing the calculated energy relaxation rate by 40% in the limit $\gamma = T_e/E_F << 1$. On the contrary, when $\gamma = T_e/E_F > 1$, the Pauli blocking factors are very close to one and the energy relaxation rate of the "hot electron tail" reduces to the formula we used in our previous work [40]:

$$d\langle E\rangle / dt = \Gamma_{em}\omega_{em} - \Gamma_{abs}\omega_{abs} \quad (7.19)$$

The Pauli blocking factor for emission, $1 - f(E_x - \hbar\omega_{em})$, is shown on Fig. 7.13. The adoption of 2D and 3D models for chemical potential have very limited impact on values of the Pauli blocking factor, which in both cases varies from 0.6 to 1 over the range of considered electronic temperatures. Moreover, as one can see on Fig. 7.13, the calculated values for the Pauli blocking factor are also is good agreement with the ones estimated

experimentally from the measured electronic occupation just after photoexcitation. Note that for the case of the lowest doping the assumption of an electronic temperature and chemical potential is highly questionable. Despite it, in this limit the electronic occupation in the hot electron tails is very low. As a consequence, the Pauli-Blocking is always very near to one, independently if considering the thermalized 2D model, thermalized 3D model or if estimating this value directly from the experiment.

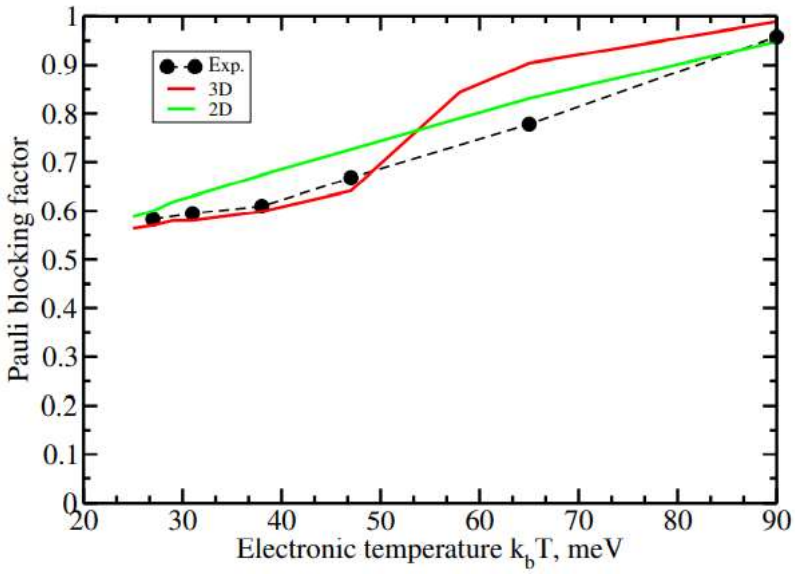

Figure 7.13: Pauli blocking factor for optical phonon emission estimated experimentally in this work (black dots) and calculated using E_x of Eq. (16) and chemical potentials of Eqs. (13) or (14-15): green and red curves.

7.6 Conclusions

Through the combination of the TrARPES measurements and theoretical calculations, we reveal that hot electrons in quasi-2DEGs display a remote coupling to polar optical phonons persisting up to high electronic density. The accurate modeling of such interaction should include the wavefunctions of confined 2D electrons, dynamical screening effects, surface plasmons polaritons and interface phonons. Nonetheless, the static screening of bulk phonons by 3D electrons can quantitatively reproduce the experimental cooling rate. This finding highlights that electrons in accumulation layers or 2D conductors at the interface with a polar medium experience 3D dissipation channels. The outcome is of high relevance for the carrier mobility in FET devices with high κ dielectric gates, van der Waals heterostrutures and 2DEGs at the interface between oxides.

References

[1] Bandurin, D., Tyurnina, A., Yu, G. et al. High electron mobility, quantum Hall effect and anomalous optical response in atomically thin InSe. *Nature Nanotech* **12**, 223–227 (2017).

[2] K. I. Bolotin, K. J. Sikes, Z. Jiang, M. Klima, G. Fudenberg, J. Hone, P. Kim, and H. L. Stormera. Ultrahigh electron mobility in suspended graphene. *Solid State Commun*. **146**, 351 (2008).

[3] Dean, C., Young, A., Meric, I. et al. Boron nitride substrates for high-quality graphene electronics. *Nature Nanotech* **5**, 722–726 (2010).

[4] Bandurin, D. A. et al. High electron mobility, quantum Hall effect and anomalous optical response in atomically thin Inse. *Nat. Nanotechnol*. **12**, 223–227 (2017).

[5] Houssa, M. High κ dielectrics. (2003).

[6] del Alamo, J. Nanometre-scale electronics with III–V compound semiconductors. *Nature* **479**, 317–323 (2011).

[7] Ohtomo, A., Hwang, H. A high-mobility electron gas at the $LaAlO_3/SrTiO_3$ heterointerface. Nature 427, 423–426 (2004).

[8] Radisavljevic, B., Radenovic, A., Brivio, J. et al. Single-layer MoS_2 transistors. *Nature Nanotech* **6**, 147–150 (2011).

[9] Chau, R., Doyle, B., Datta, S. et al. Integrated nanoelectronics for the future. *Nature Mater* **6**, 810–812 (2007).

[10] B. Jeckelmann and B. Jeanneret. The quantum hall effect as an electrical resistance standard. *Report on progress in Physics*, **64**:1603, (2001).

[11] Lesne, E., Fu, Y., Oyarzun, S. et al. Highly efficient and tunable spin-to-charge conversion through Rashba coupling at oxide interfaces. *Nature Mater* **15**, 1261–1266 (2016).

[12] A. Liu, R. Jones, L. Liao, D. Samara-Rubio, D. Rubin, O. Cohen, Nicolaescu R., and M. Paniccia. A high-speed silicon optical modulator based on a metal–oxide–semiconductor capacitor. *Nature*, **427**:615, (2004).

[13] T. Sohier, M. Calandra, and F. Mauri. Two-dimensional fröhlich interaction in transition-metal dichalcogenide monolayers: Theoretical modeling and first-principles calculations. *Phys. Rev. B*, **94**:085415, (2016).

[14] Ando, T.; Fowler, A. B.; Stern, F. Electronic Properties of Two-Dimensional Systems. *Review of Modern Physics*, **54**, 437 (1982).

[15] J.-H. Chen, C. Jang, S. Xiao, Ishigami M., and M. S. Fuhrer. Intrinsic and extrinsic performance limits of graphene devices on sio_2. *Nature Nanotechnology*, **3**:206, (2008).

[16] M. V. Fischetti, D. A. Neumayer, and E. A. Cartier. Effective electron mobility in si inversion layers in metal–oxide–semiconductor systems with a high-k insulator: The role of remote phonon scattering. *Journal of Applied Physics*, **90**:4587, (2001).

[17] Wang, Z., McKeown Walker, S., Tamai, A. *et al.* Tailoring the nature and strength of electron–phonon interactions in the $SrTiO_3$(001) 2D electron liquid. *Nature Mater* **15,** 835–839 (2016).

[18] S. Moser, L. Moreschini, J. Jaćimović, O. S. Barisic, H. Berger, A. Magrez, Y. J. Chang, K. S. Kim, A. Bostwick, E. Rotenberg, L. Forró, and Grioni M. Tunable polaronic conduction in anatase TiO_2. *Phys. Rev. Lett*., **110**:196403, (2013).

[19] S. Fratini and Guinea. F. Substrate-limited electron dynamics in graphene. *Phys. Rev. B.* **77**: 471195415, 2008.

[20] Faure, J.; Mauchain, J.; Papalazarou, E.; Yan, W.; Pinon, J.; Marsi, M.; Perfetti, L. Full characterization and optimization of a femtosecond ultraviolet laser source for time and angle resolved photoemission on solid surfaces. *Rev. Sci. Instrum.* **83**:043109, 2012.

[21] Meevasana, W., King, P., He, R. *et al.* Creation and control of a two-dimensional electron liquid at the bare $SrTiO_3$ surface. *Nature Mater* **10,** 114–118 (2011).

[22] Hsieh, D., Xia, Y., Qian, D. *et al.* A tunable topological insulator in the spin helical Dirac transport regime. *Nature* **460,** 1101–1105 (2009).

[23] H. Knox, C. Hirlimann, D. A. B. Miller, J. Shah, D. S. Chemla, and C. V. Shank. Femtosecond excitation of nonthermal carrier populations in gas quantum wells. *Phys. Rev. Lett*. **56**:1191, (1986).

[24] Z. Chen, J. Dong, E. Papalazarou, M. Marsi, C. Giorgetti, Z. Zhang, B. Tian, J.-P. Rueff, A. Taleb-Ibrahimi, and L. Perfetti. Band gap renormalization, carrier multiplication, and stark broadening in photoexcited black phosphorus. *Nano Lett.* **19**:488, (2019).

[25] Z. Chen, M.-i Lee, Z. Zhang, H. Diab, D. Garrot, F. Lédée, P. Fertey, E. Papalazarou, M. Marsi, C. Ponseca, E. Deleporte, A. Tejeda, and Perfetti L. Time-resolved photoemission spectroscopy of electronic cooling and localization in $ch_3nh_3pbi_3$ crystals. *Phys. Rev. Materials*,**1**:045402, (2017).

[26] P Giannozzi, et al., Advanced capabilities for materials modelling with quantum espresso. *J. Phys.: Condens. Matter* **29**, 465901 (2017).

[27] SJ Magorrian, V Zólyomi, VI Fal'ko, Giant anisotropy of spin-orbit splitting at the bismuth surface. *Phys. Rev. Lett.* **94**, 245431 (2O16).

[28] P Vogl, Microscopic theory of electron-phonon interaction in insulators or semiconductors. *Phys. Rev. B.* **13**, 694 (1976).

[29] T Sohier, M Calandra, F Mauri, Two-dimensional fröhlich interaction in transition-metal dichalcogenide monolayers: Theoretical modeling and first-principles calculations. *Phys. Rev. B* **94**, 085415 (2016).

[30] F Stern, Polarizability of a two-dimensional electron gas. *Phys. Rev. Lett*. **18**, 546 (1967).

[31] A. Chevy. Improvement of growth parameters for bridgman-grown inse crystals. *Journal of Crystal Growth,* **67**:119, (1984).

[32] Sjakste, J.; Vast, N.; Calandra, M.; Mauri, F. Wannier interpolation of the electron-phonon matrix elements in polar semiconductors: Polar-optical coupling in GaAs. *Phys.Rev. B*. **92**, 054307(2015).

[33] E Papalazarou, et al., Unraveling the dirac fermion dynamics of the bulk-insulating topological system. *Phys. Rev. Mater*. **2**, 104202 (2018).

[34] Z. Zhang, Z. Chen, M. Bouaziz, C. Giorgetti, H. Yi, J. Avila, B. Tian, A. Shukla, L. Perfetti, D. Fan, Y. Li, and A. Bendounan. Direct observation of band gap renormalization in layered indium selenide. *ACS Nano*, **13**:13486, (2019).

[35] J. Sjakste, K. Tanimura, G. Barbarino, L. Perfetti, and N. Vast. Hot electron relaxation dynamics in semiconductors: assessing the strength of the electron–phonon coupling from the theoretical and experimental viewpoints. *Journal of Physics: Condensed Matter*, **30**:353001, (2018).

[36] S. Moser, Jovic V., Koch R., L. Moreschini, J.-S. Oh, C. Jozwiak, A. Bostwick, and E. Rotenberg. How to extract the surface potential profile from the arpes signature of a 2deg. *J. Electron Spectrosc.,* **225**:16, (2018).

[37] A. Segura, J. Bouvier, M. V. Andrés, F. J. Manjón, and Munoz V. Strong optical nonlinearities in gallium and indium selenides related to inter-valence-band transitions induced by light pulses. *J. Phys.: Condens. Matter,* **56**:4075, (1997).

[38] P. Allen. Theory of thermal relaxation of electrons in metals. *Phys. Rev. Lett*. **59**:1460, (1987).

[39] S. Panda and Panda B. K. Theory of thermal relaxation of electrons in metals. *J. Phys. Condens. Matter*, **20**:485201, (2008).

[40] Chen, Z.; Giorgetti, C.; Sjakste, J.; Cabouat, R.; Véniard, V.; Zhang, Z.; Taleb Ibrahimi, A.; Papalazarou, E.; Marsi, M.; Shukla, A.; Peretti, J.; Perfetti, L. Ultrafast electron dynamics reveal the high potential of InSe for hot-carrier optoelectronics. *Phys. Rev. B*, **97**:241201, (2018).

[41] O. Madelung, U. Rössler, and M. Schulz. Indium selenide (inse) phonon wavenumbers. *Datasheet from Landolt-Börnstein, - Group III Condensed Matter Volume 41C: Non469 Tetrahedrally Bonded Elements and Binary Compounds*, -:–(1998).

Chapter 8 Transition from Band Insulator to Mott Insulator in 1T-TaS2 based on photoinjection

8.1 Introduction

The transition metal dichalcogenide (TMDC) 1T-TaS_2 is a Charge Density wave (CDW) system that has promising applications in the development of neuromorphic memories [1,2]. The emergent orders observed in layered 1T-TaS_2 result from a subtle interplay between Coulomb repulsion, electron−lattice coupling and van der Waals interactions [3-6]. This TMDC has been intensively investigated, with the aim of better elucidating the microscopic nature of the collective instabilities in the phase diagram [7-11]. Upon the variation of temperature or pressure, the 1T-TaS_2 crystal shows indeed a complex phase diagram, which is further enriched by the occurrence of metastable phases attained via photoexcitation or electrical pulses. The application of external pressure can change the CDW structure and can even induce a superconducting state [12-14]. The temperature variation induces a variety of charge-ordered instabilities [15-17], some of which favoring a Mott localization of the conducting electrons. In some specific conditions, photoexcitation or current injection can even generate a metastable state with glassy like arrangement of the periodic distortion [18-21]. In the following we will be mainly interested in the phase transitions that can be observed by varying the sample temperature. The 1T-TaS_2 system develops an InCommensurate CDW (IC-CDW) phase below 550 K, a Nearly-Commensurate CDW (NC-CDW) phase below 350 K and, finally, a Commensurate CDW (C-CDW) phase below 180 K. Upon heating, the crystal also displays a Triclinic CDW (T-CDW) phase between the C-CDW phase and NC-CDW phase [22-24]. Figure 8.1 plots the change of resistivity across the several phase transitions that have been observed by varying the temperature of 1T-TaS_2 [24]. In their recent work, Y. D. Wang and colleagues combined transport measurements, Angle-resolved photoemission spectroscopy and X-Ray diffraction [24] to correlate structural with electronic properties across the phase transitions. They revealed the appearance of half-integer-indexed diffraction peaks along the c axis when the system enters the C-CDW phase. Together with the out of plane dispersion of electronic states, this finding indicates the presence of an interlayer dimerization in the ground state of 1T-TaS_2. Although the electronic interactions also may be important in the C-CDW phase, this gapped state of a dimerized structure is compatible with band structure theory, questioning the common view of a Mott phase being responsible for a gap in the excitation spectrum. Upon heating, the surface of the system

undergoes a transition into a new insulating state, which only exists in a narrow temperature window between 217 K and 233 K. This result highlights that the competition between on-site Coulomb repulsion and interlayer hopping plays a crucial role in defining the electronic properties of this material [25-27]. The new Intermediate CDW (I-CDW) shown in Figure 8.2 has been observed by ARPES measurements but remains elusive by the bulk sensitive probes as X-ray scattering and electronic transport.

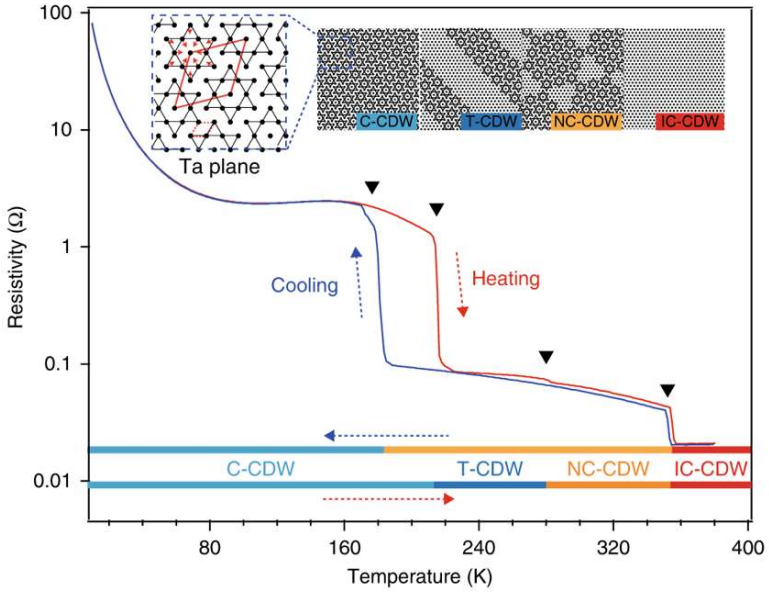

Figure 8.1: Temperature dependence of in-plane resistivity taken upon heating and cooling. The black arrows mark the first-order transition temperatures. The bars below the curves indicate temperature intervals corresponding to the different phases. Inset panels are schematic illustrations for the in-plane lattice modulations in the commensurate CDW (C-CDW) phase, nearly commensurate CDW (NC-CDW) phase, Triclinic CDW (T-CDW) phase, and Incommensurate CDW (IC-CDW) phase, respectively. The SD clusters are marked with the dark outlines. Black dots stand for the Ta atoms [24].

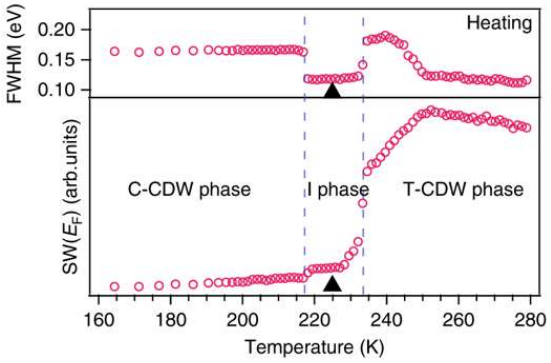

Figure 8.2: Temperature dependence of full width at half maximum (FWHM) and the spectral weight (SW) of the highest occupied band. The analyzed spectra are at the Γ point, where the Ta 5d band crosses E_F ([−0.1, 0.1 eV], [−0.4, −0.3 $Å^{-1}$]) upon heating [24].

Although significant attention has been focused on the different phases in 1T-TaS_2 at low temperature [15-17, 28, 29], the occurrence of the I-CDW state is still debated. In order provide new insights on this subject we study here the electronic structures of 1T-TaS_2 by varying the temperature and photo injection. During the heating cycle, we also observe an intermediate I-CDW state in a narrow temperature window between the C-CDW phase and T-CDW phase. This finding is indeed in agreement with the work of the group of Y. D. Wang. In addition, we show some temperature dependent LEED measurements, suggesting that the surface structure of the I-CDW is slightly different from the one of the C-CDW. Our data are consistent with the interpretation that the C-CDW phase at low temperatures is a band insulator with interlayer dimerization and likely favored by the presence of strong correlations. Instead, the I-CDW phase should be ascribed to a surface reconstruction, probably due to the decoupling of the outermost layer and that would lead to a Mott insulating surface. Finally, we try to follow the dynamics of this phase by injecting femtosecond pulses. However, the continuous wave heating generated by the pump beam make difficult the time resolved acquisition in a stable phase. More detailed investigations will be necessary to unambiguously identify the structure and electronic properties of such surface reconstruction [30, 31].

8.2 Experimental details

Our experiments were performed on the femto-ARPES setup [32], using a Ti: Sapphire laser system delivering 6 μJ pulses with a 250 kHz repetition rate. In order to gain the two-photon photoemission spectra, part of the laser source (50 fs pulse, 1.57 eV) is used to excite the sample while the rest is employed to generate 6.3 eV photons as probe beam through cascade frequency mixing in BaB_2O_4 (BBO) crystals. Besides, the polarization directions are both P polarized for the pump beam and probe beam. The overall energy resolution of the experiment is around 30 meV and the cross correlation between two beams has full width at half maximum (FWHM) of 150 fs. In all measurements, the samples were cleaved and kept at the base pressure of 8×10^{-11} mbar. Our samples have been oriented by low energy electron diffraction in figure 8.3 and measured in the temperature range from 135 K to 300 K (± 2 K).

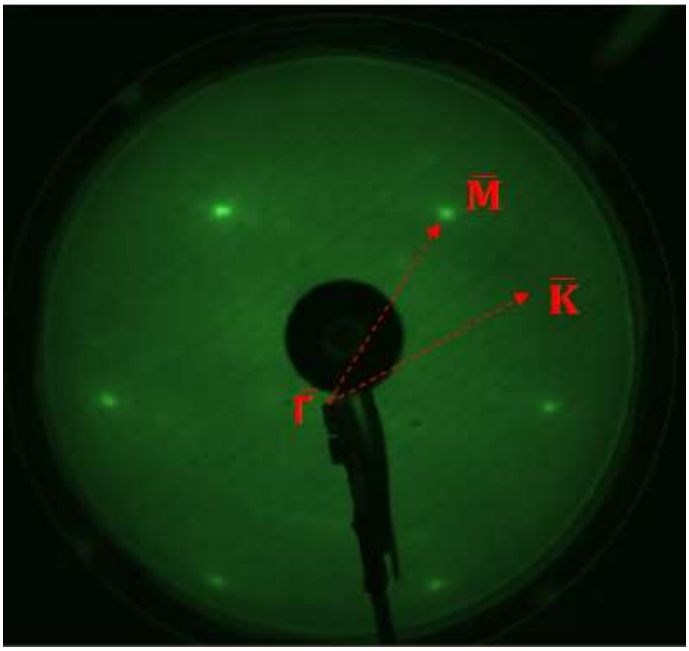

Figure 8.3: LEED pattern of 1T-TaS_2 at 300 K.

8.3 Results and discussion

Layered 1T-TaS_2 crystal structure consisting of S-Ta-S sandwiches, stacked through van der Waals interactions as shown in Figure 8.4. The electronic structure is very sensitive to the specific charge ordering of the CDWs phases. Figures 8.5a and 8.5b display the photoelectron intensity maps along the $\bar{\Gamma}$-$\bar{M}$ direction, acquired with 6.3 eV photons at different sample temperatures, either upon cooling or heating the sample. Figure 8.5c and 8.5d show the map integrated in the wave-vector interval [-0.10, 0.10] $Å^{-1}$. Upon cooling, we observe at 182 K the transition from a metallic state with nearly commensurate order (NC-CDW) to an insulating phase with commensurate structural distortion (C-CDW). Upon heating, the C-CDW state displays the transition to an intermediate I-CDW phase at 221 K and a second transition from the I-CDW to the NC-CDW phase at 229 K. As shown in Figures 8.5b and 8.5d the intermediate state I-CDW can be stabilized in a narrow temperature window (221 – 229 K). Our results confirm the recent finding of Y. D. Wang. *et al* [27].

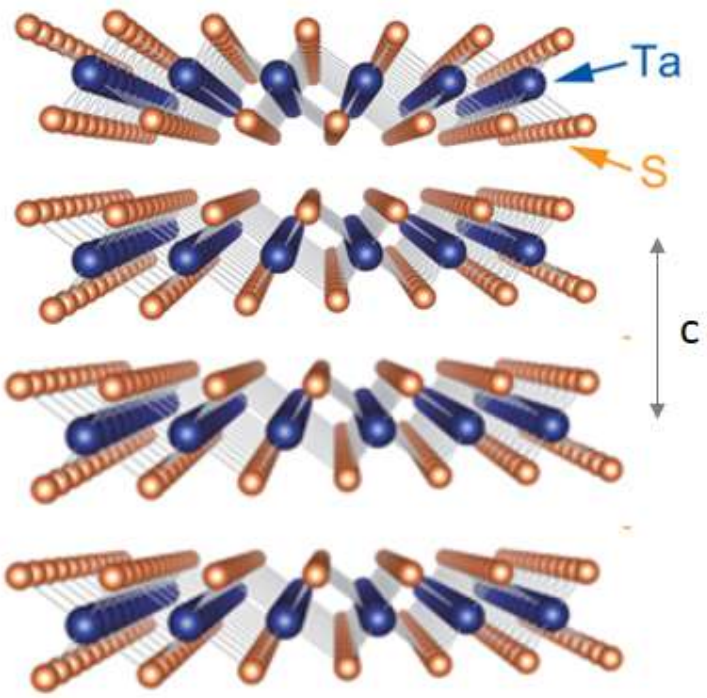

Figure 8.4: Crystal structure of 1T-TaS_2.

Figure 8.6 shows energy distribution curves (EDC) of the NC-CDW, C-CDW and I-CDW, obtained by integrating the photoelectron intensity maps in the wave-vector interval [-0.10, 0.10] $Å^{-1}$. Note that the EDC of the C-CDW phase is broader in energy than the one of the I-CDW phase. An important contribution to the broadening of the EDC in the C-CDW phase is due to interlayer coupling. This term leads to a sizable dispersion of the electronic states along the c axis direction and results in a projected density of the states with large energy width. Since the ARPES signal measures a weighted density of the electronic states perpendicular to the surface, we also expect that states with larger out of plane dispersion result in a broader EDC. When entering the I-CDW phase, the EDC becomes thinner and the peak moves farther from the chemical potential. This observation suggests that the I-CDW phase is actually a surface reconstruction in which the topmost layer decouples from the underlying ones and enters in a Mott insulating regime. Figure 8.6 shows that, near to the Fermi level, the spectral intensity of the I-CDW spectrum nearly follow the spectral intensity of the T-CDW rescaled by a factor 0.6. As a consequence, we assume that 60% of the spectrum acquired in the I-CDW is a bulk contribution corresponding to the T-CDW and 40% due to photoelectrons emitted by the outermost layer in the Mott phase. Note also that a similar surface Mott transition has been already reported in the parent compound 1T-TaS_2 [33]. Moreover, recent spectroscopic measurements of 1T-$TaSe_2$ as a function of layer number support the conjecture that such

decoupled layer should have a larger gap size, due to the localization of the conducting electrons in a half filled orbital [34].

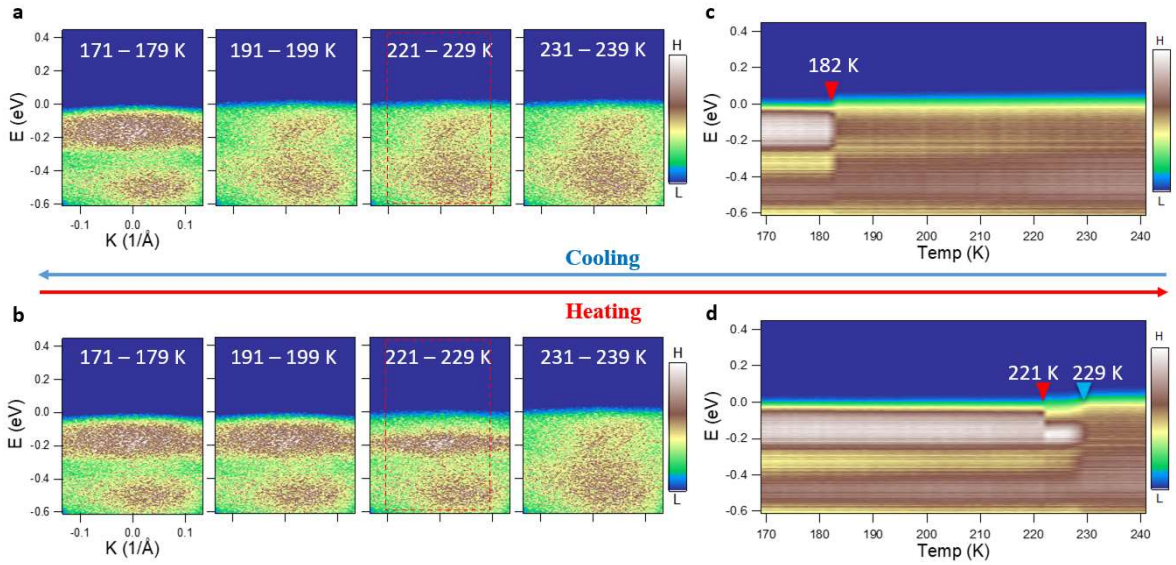

Figure 8.5: Temperature dependent ARPES study of 1T-TaS_2 upon cooling and heating. a) and b), photoelectron intensity maps along the $\bar{\Gamma}$-$\bar{M}$ direction with 6.3 eV photons at different temperatures upon cooling and heating, respectively. (The red rectangles in a) and b) highlight the occupied bands, which determine if the material is a metal or an insulator). c) and d), photoelectron intensity maps integrated in the wave-vector interval [-0.10, 0.10] $Å^{-1}$ and zoomed in the energy region corresponding to the red rectangles in a) and b). The red arrow in c) marks the transition temperature from the NC-CDW state to the C-CDW state. The red arrow in d) marks the transition temperature from the C-CDW to the I-CDW state and the blue arrow in d) marks that the transition temperature from the I-CDW to the T-CDW state.

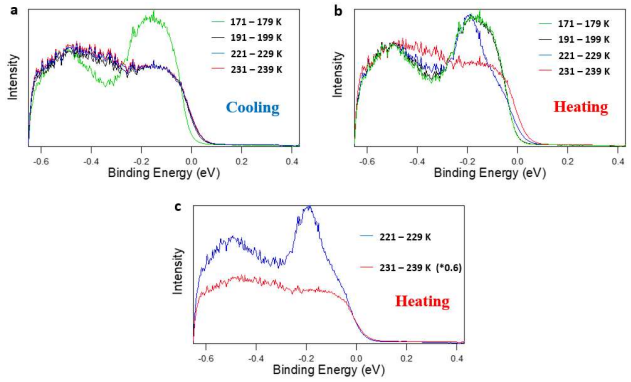

Figure 8.6: Energy distribution curves of the NC-CDW, T-CDW, C-CDW and I-CDW (different temperature ranges), obtained by integrating the photoelectron intensity maps in the wave-vector interval [-0.10, 0.10] $Å^{-1}$. a) the green spectrum corresponds to the C-CDW, while the others correspond to the NC-CDW. b) the green and dark spectrum correspond to the C-CDW, the blue spectrum corresponds to the I-CDW phase and the red spectrum corresponds to the T-CDW. c) the blue spectrum corresponds to the I-CDW phase and the red spectrum corresponds to the T-CDW whose intensity is rescaled by a factor 0.6.

The fact that bulk sensitive techniques could not spot any hint of I-CDW phase is a strong indication that such state is indeed a surface phase transition. In order to gain more insights, we have performed LEED measurements. As for the case of ARPES, also LEED is a surface sensitive technique that is especially suited to observe structural reconstructions in the uppermost layers. We call A(T) the intensity of the diffraction pattern observed at temperature T. Figures 8.7 a, b) shows the intensity ratio R(T)=A(T)/A (190 K) for two representative temperatures: T=175 K and T=200 K. From R (175 K) we evince that the Bragg spots and superlattice peaks become brighter in the C-CDW phase than in the NC-CDW. As expected we find that R (190 K) is identical to unity in the cooling cycle (since both images refer to the NC-CDW phase). In order to follow the temperature evolution of surface structure we plot in Fig. 8.7c) the intensity variation S(T) that takes place around a Bragg spot when the temperature is changed from T to T-dT. In the cooling cycle the data reveal a significant increase of S(t) at the transition from the NC-CDW to the C-CDW. Figure 8.7d) show that during the heating cycle, S(t) shows weak variations both at the C-CDW to I-CDW phase transition and as well as the I-CDW to T-CDW phase transition. These preliminary data suggest that a slight structural distortion takes place when entering in the I-CDW eventually due to the decoupling of the topmost layer from the underlying ones. Also the surface structural distortion from the I-CDW to the T-CDW, which is observed in the heating cycle at 229 K, seems much smaller (smaller variation of S(T)) than the NC-CDW to the C-CDW that takes place at 182 K in the cooling cycle.

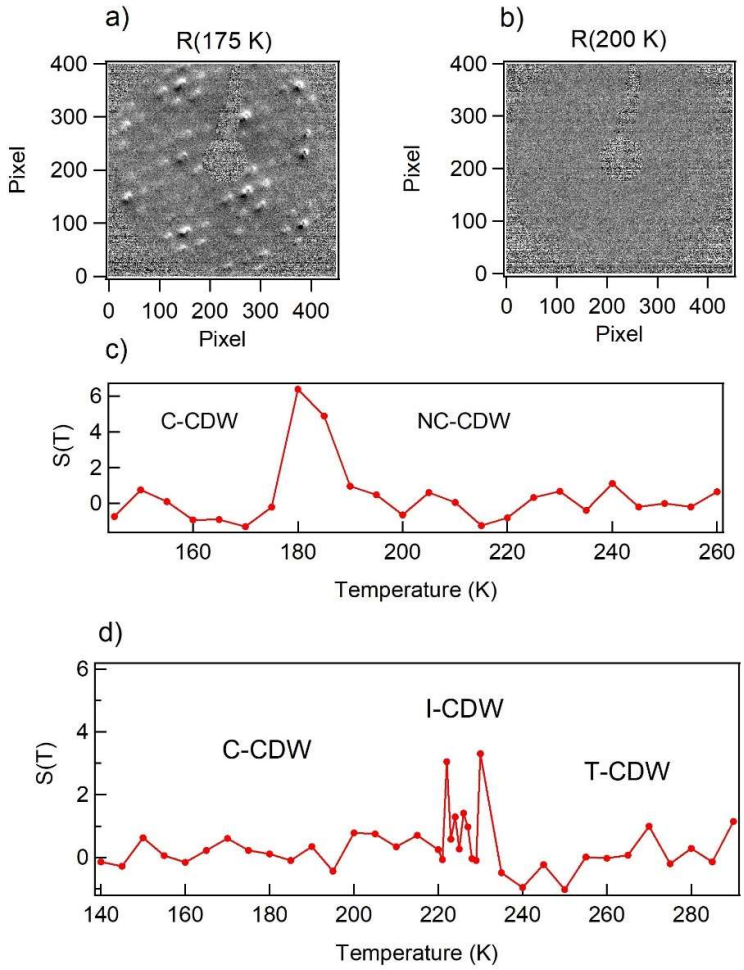

Figure 8.7: a) Ratio R(T)=A(T)/A(190 K) for T=175 K during the cooling cycle. The signal arises from the transition from the NC-CDW to the C-CDW. b) confirmation that the ratio R(T)=A(T)/A(190 K) is one if T=200 K, namely when on phase transition takes place. c) Intensity variation of the Bragg spots during the cooling cycle. d) Intensity variation of the Bragg spots during the heating cycle.

In order to follow the electron dynamics in the C-CDW and I-CDW state we also tried to perform TrARPES at temperatures close to the phase transition. The sample is first cooled down to 130 K from room temperature using liquid nitrogen cooling system, and then heated to 211 K from 130 K. The temperature stabilization has been obtained by reducing the liquid nitrogen cooling and heating the sample via a temperature controller. We perform the time resolved measurements along the $\bar{\Gamma}$-$\bar{M}$ direction with a pump beam and probe beam centered at 1.57 eV and 6.3 eV, respectively. Figure 8.8 shows the photoelectron intensity as a function of pump probe delay, for the different fluences between 70 μJ/cm^2 to 510 μJ/cm^2. We also mark on the top axis the acquisition time from the beginning of the scan. The temporal evolution is consistent with previous

measurements. A photoinduced gap collapse at early delays comes together with periodic modulation of the spectral density due to the coherent excitation of the CDW amplitude mode. The C-CDW looks stable for the entire duration of the measurement (35 minutes) even at the highest pumping fluence of 510 μJ/cm^2. We conclude that the local temperature of the sample stays below 221 K at all pumping fluences that have been employed. We are currently trying to stabilize the system in the I-CDW phase in order to perform time resolved measurements in this phase and compare the results to the dynamics of electrons in the C-CDW phase.

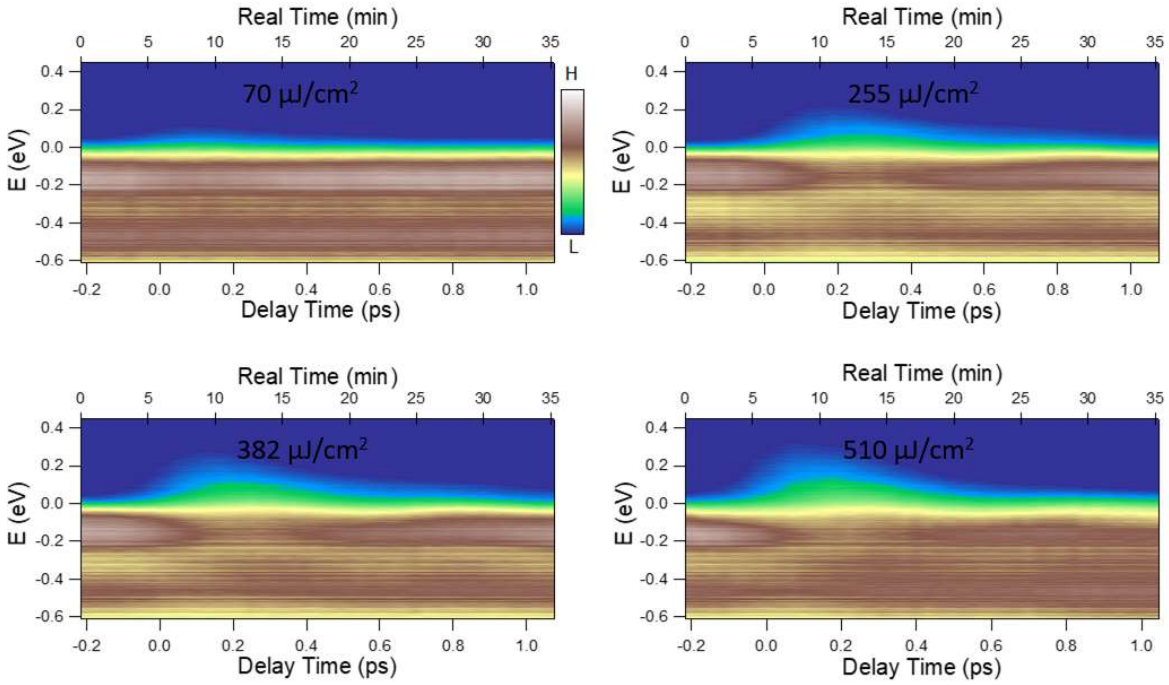

Figure 8.8: The photoelectron intensity maps integrated in the wave-vector interval [-0.10, 0.10] Å^{-1} versus the different pump fluences at 211 K.

8.4 Conclusions

Our ARPES data confirmed the presence of I-CDW phase within a narrow temperature window during the heating cycle of 1T-TaS_2. The larger gap of the I-CDW is compatible with the occurrence of a Mott instability driven by the structural decoupling of the topmost layer. The temperature dependent LEED analysis show a weak but detectable structural change at the transition from the C-CDW to the I-CDW. Moreover, it has been possible to perform high fluence Tr-ARPES measurements at a temperature near to the I-CDW

phase. Next step will be to stabilize the I-CDW phase enough to perform tr-ARPES at high fluence in this putative Mott surface.

References

[1] Chen, T.; Dumas, R. K.; Eklund, A.; Muduli, P. K.; Houshang, A.; Awad, A. A.; Dürrenfeld, P.; Malm, B. G.; Rusu, A.; Akerman, J. Spin-Torque and Spin-Hall Nano-Oscillators. *Proc. IEEE* **104** (10), 1919−1945 (2016).

[2] Sajid Husain, Xin Chen, Rahul Gupta, Nilamani Behera, Prabhat Kumar, Tomas Edvinsson, F. García-Sánchez, Rimantas Brucas, Sujeet Chaudhary, Biplab Sanyal, Peter Svedlindh, and Ankit Kumar. Large Damping-Like Spin–Orbit Torque in a 2D Conductive 1T-TaS2 Monolayer. *Nano Letters* **20** (9), 6372-6380 (2020).

[3] Geim, A. K. & Grigorieva, I. V. Van der Waals heterostructures. *Nature* **499**, 419–425 (2013).

[4] Svetin, D., Vaskivskyi, I., Brazovskii, S. & Mihailovic, D. Three-dimensional resistivity and switching between correlated electronic states in 1T-TaS_2. *Sci. Rep*. **7**, 46048 (2017).

[5] Yoshida, M., Suzuki, R., Zhang, Y., Nakano, M. & Iwasa, Y. Memristive phase switching in two-dimensional 1T-TaS_2 crystals. *Sci. Adv*. **1**, e1500606 (2015).

[6] Stojchevska, L. et al. Ultrafast switching to a stable hidden quantum state in an electronic crystal. *Science* **344**, 177–180 (2014).

[7] L. Perfetti, P. A. Loukakos, M. Lisowski, U. Bovensiepen, H. Berger, S. Biermann, P. S. Cornaglia, A. Georges, and M. Wolf. Time Evolution of the Electronic Structure of 1T−TaS_2 through the Insulator-Metal Transition. *Phys. Rev. Lett*. **97**, 067402 (2006)

[8] Yu, Y., Yang, F., Lu, X. et al. Gate-tunable phase transitions in thin flakes of 1T-TaS_2. *Nature Nanotech* **10**, 270–276 (2015).

[9] Eichberger, M., Schäfer, H., Krumova, M. et al. Snapshots of cooperative atomic motions in the optical suppression of charge density waves. *Nature* **468**, 799–802 (2010).

[10] Kim, K.S., Ji, Y.J., Kim, K.H. et al. Ultrasensitive MoS_2 photodetector by serial nano-bridge multi-heterojunction. *Nat Commun* **10**, 4701 (2019).

[11] Butler, C.J., Yoshida, M., Hanaguri, T. et al. Mottness versus unit-cell doubling as the driver of the insulating state in 1T-TaS_2. *Nat Commun* **11**, 2477 (2020).

[12] Sylvain Ravy; Claire Laulhé; Jean-Paul Itié; Pierre Fertey; Benoit Corraze; Sabrina Salmon; Laurent Cario. High-pressure X-ray diffraction study of 1T-TaS_2. *Physica B* **407**, 1704-1706 (2012).

[13] Wang, X., Liu, Y., Chen, X., Zhang, P., Liu, X. Prediction of a novel robust superconducting state in TaS_2 under high pressure. *Phys. Chem. Chem. Phys.* **22**, 8827-8833 (2020).

[14] Hu, K., Chen, Q.-J., Xie, S.-Y. Pressure induced superconductive 10-fold coordinated TaS_2: A first-principles study. *Journal of Physics Condensed Matter* **32** 085402 (2020).

[15] Kim, J-J., Yamaguchi, W., Hasegawa, T. & Kitazawa, K. Observation of Mott localization gap using low temperature scanning tunneling spectroscopy in commensurate 1T-TaS_2. *Phys. Rev. Lett*. **73**, 2103–2106 (1994).

[16] Sipos, B., Kusmartseva, A. F., Akrap, A., Berger, H., Forró, L. & Tutiš, E. From Mott state to superconductivity in 1T-TaS_2. *Nat. Mater*. **7**, 960–965 (2008).

[17] Rossnagel, K. On the origin of charge-density waves in select layered transition-metal dichalcogenides. *J. Phys. Condens. Matter* **23**, 213001 (2011).

[18] Vaskivskyi, I. et al. Controlling the metal-to-insulator relaxation of the metastable hidden quantum state in 1T-TaS_2. *Sci. Adv*. **1**, e1500168 (2015).

[19] Hollander, M. J. et al. Electrically driven reversible insulator-metal phase transition in 1T-TaS_2. *Nano Lett*. **15**, 1861–1866 (2015).

[20] Perfetti, L. et al. Femtosecond dynamics of electronic states in the Mott insulator 1T-TaS_2 by time resolved photoelectron spectroscopy. *New J. Phys*. **10**, 053019 (2008).

[21] Stahl, Q., Kusch, M., Heinsch, F. et al. Collapse of layer dimerization in the photo-induced hidden state of 1T-TaS_2. *Nat Commun* **11**, 1247 (2020).

[22] Wang, W., Dietzel, D. & Schirmeisen, A. Lattice Discontinuities of 1T-TaS_2 across First Order Charge Density Wave Phase Transitions. *Sci Rep* **9**, 7066 (2019).

[23] Sakabe, D., Liu, Z., Suenaga, K. et al. Direct observation of mono-layer, bi-layer, and tri-layer charge density waves in 1T-TaS_2 by transmission electron microscopy without a substrate. *npj Quant Mater* **2**, 22 (2017).

[24] Wang, Y.D., Yao, W.L., Xin, Z.M. et al. Band insulator to Mott insulator transition in 1T-TaS2. *Nat Commun* **11**, 4215 (2020).

[25] Parendo, K. A. et al. Electrostatic tuning of the superconductor–insulator transition in two dimensions. *Phys. Rev. Lett*. **94**, 197004 (2005).

[26] Perfetti, L., Gloor, T. A., Mila, F., Berger, H. & Grioni, M. Unexpected periodicity in the quasi-two-dimensional Mott insulator 1T−TaS_2 revealed by angle-resolved photoemission. *Phys. Rev. B* **71**, 153101 (2005).

[27] Chen, Z.; Dong, J.; Papalazarou, E.; Marsi, M.; Giorgetti, C.; Zhang, Z.; Tian, B.; Rueff, J.-P.; Taleb-Ibrahimi, A.; Perfetti, L. Band Gap Renormalization, Carrier Multiplication, and Stark Broadening in Photoexcited Black Phosphorus. *Nano Lett* **19**, 488– 493 (2019).

[28] Ribak, A., Silber, I., Baines, C., Chashka, K., Salman, Z., Dagan, Y. & Kanigel, A. Gapless excitations in the ground state of 1T-TaS_2. *Phys. Rev. B* **96**, 195131 (2017).

[29] Tosatti, E. & Fazekas, P. On the nature of the low-temperature phase of 1T-TaS_2. *J. Phys. Colloques* **37**, C4-165- C4-168 (1976).

[30] Chen, Z.; Giorgetti, C.; Sjakste, J.; Cabouat, R.; Veniard, V.; Zhang, Z.; TalebIbrahimi, A.; Papalazarou, E.; Marsi, M.; Shukla, A.; J., P.; Perfetti, L. Ultrafast electrons dynamics reveal the high potential of InSe for hot carrier optoelectronics. *Physical Review B* **97**, 241201 (2018).

[31] Shibuta, M., Yamamoto, K., Ohta, T. et al. Direct observation of photocarrier electron dynamics in C_{60} films on graphite by time-resolved two-photon photoemission. *Sci Rep* **6**, 35853 (2016).

[32] Faure, J.; Mauchain, J.; Papalazarou, E.; Yan, W.; Pinon, J.; Marsi, M.; Perfetti, L. Full characterization and optimization of a femtosecond ultraviolet laser source for time and angle-resolved photoemission on solid surfaces. *Rev. Sci. Instrum* **83**, 043109 (2012).

[33] Butler, C.J., Yoshida, M., Hanaguri, T. et al. Mottness versus unit-cell doubling as the driver of the insulating state in 1T-TaS_2. *Nat Commun* **11**, 2477 (2020).

[34] L. Perfetti, A. Georges, S. Florens, S. Biermann, S. Mitrovic, Y. Tomm, H. Höchst, M. Grioni Spectroscopic signatures of a bandwidth-controlled Mott transition at the surface of 1T-$TaSe_2$. *Phys. Rev. Lett.* **90**, 166401 (2003).

Conclusions and Future work

This thesis investigates three different layered materials by means of TrARPES and surface doping. The unique ability of our experimental method to detect transient electronic states and cooling process of hot carriers can be of high relevance to determine the optoelectronic properties of layered materials and heterostructures. Moreover, ARPES with our laser-based photon source can also probe buried electronic states that would go undetected when doing ARPES with synchrotron light source. The beams generated from our laser system have a duration of roughly 100 fs. This timescale is short enough to study the electronic thermalization, cooling by phonon emission and carrier's recombination in layered semiconductors.

In our work on black phosphorus, we reveal that photoexcited electrons do not induce a sizable renormalization of the bandgap and that they thermalize near to the conduction band minimum without leading to carrier's multiplication. At early pump-probe delay the ionization of charged defects is also responsible for a Stark broadening of the electronic states. We could generate an accumulation layer of varying carrier's concentration by in-situ Cesium evaporation. The time laser-based TrARPES allows us to follow the collapse of electronic gap with unmatched accuracy. Moreover, the buried states of valence band cannot be detected via Synchrotron ARPES but are accessible by the longer escape depth of low energy photoelectrons. Our ARPES maps revealed an intriguing increase of the valence band dispersion at high doping level. We obtained interesting results on the layered ε-InSe, which is one of most promising layered semiconductors for optoelectronics. The in-situ alkali metals evaporation generates a two dimensional electrons gas of variable carrier's density. The TrARPES method has been employed to quantify the cooling rate of hot electrons as a function of electronic concentration. Our results show that the quantum screening of Longitudinal Optical (LO) phonons due to the accumulation layer is not as efficient as it would be in a strictly 2D dimensional system but rather follows the behavior of a bulk compound with equivalent filling. We ascribe this finding to the remote Fröhlich coupling of confined electronic states with bulk polar mode. Finally, we carefully reconstructed the phase diagram of the transition metal dichalcongenide 1T-TaS_2. Our data confirm recent reports claiming the presence of a new I-CDW phase taking place during the heating cycle and in a narrow temperature range. Most likely, this phase is related to a decoupling of the topmost layer from the underlying bulk, leading to a Mott insulating phase with larger gap than the C-CDW phase.

Future perspectives of this work are the complete analysis of the hot electrons dynamics in Black phosphorous with different surface doping. In particular, the thermalization and recombination time that we have extracted should be compared to the ab-initio calculations. In the case of 1T-TaS_2, it would be interesting to perform tr-ARPES of the I-CDW phase and to investigate the dynamics of electrons and CDW mode after an evaporation of alkaline atoms at the surface.

List of Publications

1.* Chen, Z.; **Dong, J**.; Papalazarou, E.; Marsi, M.; Giorgetti, C.; Zhang, Z.; Tian, B.; Rueff, J.-P.; Taleb-Ibrahimi, A.; Perfetti, L. "*Band Gap Renormalization, Carrier Multiplication, and Stark Broadening in Photoexcited Black Phosphorus"*. Nano Lett, 19, 488 (2019).

2.* Zhesheng Chen, **Jingwei Dong**, Christine Giorgetti, Evangelos Papalazarou, Marino Marsi, Zailan Zhang, Bingbing Tian, Qingwei Ma, Yingchun Cheng, Jean-Pascal Rueff, Armina Taleb-Ibrahimi and Luca Perfetti. "*Spectroscopy of buried states in black phosphorous with surface doping".* 2D Materials. doi.org/10.1088/2053-1583/ab8ec1. (2020).

3.* Zhesheng Chen, **Jingwei Dong**, Christine Giorgetti, Evangelos Papalazarou, Marino Marsi, Zailan Zhang, Bingbing Tian, Qingwei Ma, Yingchun Cheng, Jean-Pascal Rueff, Amina Taleb-Ibrahimi, and Luca Perfetti. "*Significant tunability of hot-carrier dynamics in black phosphorus".* (In preparation).

4.* Zhesheng Chen, Jelena Sjakste, **Jingwei Dong**, Amina Taleb-Ibrahimi, Jean-Pascal Rueff, Abhay Shukla, Jacques Peretti, Evangelos Papalazarou, Marino Marsi, and Luca Perfetti. "*Ultrafast dynamics of hot carriers in a quasi-two-dimensional electron gas on InSe"*. PNAS 117 (36), 21962-21967; doi:10.1073/pnas.2008282117 (2020).

5.* **Jingwei Dong**. et al. Transition from Band Insulator to Mott Insulator in 1T-TaS_2 based on photoinjection. (In preparation)

6. Eunhwan Jung, Kestutis Budzinauskas, Senol Öz, Feray Ünlü, Henning Kuhn, Julian Wagner, David Grabowski, Benjamin Klingebiel, Marie Cherasse, **Jingwei Dong**, Pierfrancesco Aversa, Paola Vivo, Thomas Kirchartz, Tsutomu Miyasaka, Paul H. M. van Loosdrecht, Luca Perfetti, and Sanjay Mathur. "*Femto- to Microsecond Dynamics of Excited Electrons in a Quadruple Cation Perovskite"*. ACS Energy Letters 5 (3), 785-792 (2020).

7. Jacques Hawecker, T. H. Dang, James Boust, Sophie Collin, Jean-Marie-Georges, Henri-Jean Drohuin, Yannis Laplace, Romain Grasset, **Jingwei Dong**, Juliette Mangeney et Jerome Tignon Henri Jaffrès, Luca Perfetti and Sukhdeep Dhillon. "*Correlation between spin-mixing-conductance, THz emission and spin-memory-loss at magnetic/heavy metal interfaces".* (Submitted to Science Advances).

8. Zhesheng Chen, J. Caillaux, J. Zhang, E. Papalazarou, **Jingwei Dong**, J.-P. Rueff, A. Taleb-Ibrahimi, L. Perfetti and M. Marsi. "*Ultrafast dynamics with time-resolved ARPES: photoexcited electronic bands in monochalcogenide semiconductors".* (Submitted to the French Academy of Science (CRAS)).

* **Papers included in this thesis**

ECOLE DOCTORALE

Titre : Dynamique des électrons dans les matériaux superposés

Mots clés : Dynamique ultrafast, semi-conducteurs superposés, structure électronique

Résumé : Actuellement, les matériaux superposés suscitent un grand intérêt en raison de leurs propriétés électriques et optiques. Ces cristaux peuvent être éclaircis jusqu'à la couche unique et afficher une structure de bande électronique qui dépend fortement de l'épaisseur de l'échantillon. La grande tunabilité du criblage électronique et la taille de l'écart peuvent être très attrayantes pour la création d'hétérostructures dont les propriétés peuvent être conçues sur demande. Ces objectifs motivent le regain d'attention aux composés connus depuis de nombreuses années. Nous pouvons dire que le champ de recherche des matériaux de faible dimension a été stimulé par la découverte du graphène et a rapidement été agrandi à d'autres matériaux comme les dichalcogénides métalliques de transition, le phosphore noir et le sélénide d'Indium. Nos travaux se concentreront sur la dynamique de l'état excité dans ces composés, ainsi que sur l'évolution de la structure de la bande sur le dopage de surface.

Title : Electron dynamics in layered materials

Keywords : Ultrafast dynamics, layered semiconductor, electronic structure

Abstract : Currently, layered materials attract great interest due to their electrical and optical properties. Such crystals can be thinned down to the single layer and display an electronic band structure that strongly depends on the sample thickness. The large tunability of the electronic screening and gap size can be very attractive for the creation of heterostructures whose properties can be designed on demand. These goals motivate the renewed attention to compounds that were known for many years. We can say that the research field of low dimensional materials has been boosted by the discovery of graphene and quickly has been enlarged to other materials like transition metal dichalcogenides, black phosphorous and Indium selenide. Our work will focus on the excited state dynamics in these compounds, as well as on the evolution of the band structure upon surface doping.